STUDY QUARK GLUON PLASMA BY PARTICLE CORRELATIONS IN HEAVY ION COLLISIONS

A Dissertation
Submitted to the Faculty
of
Purdue University
by
Li Yi

In Partial Fulfillment of the
Requirements for the Degree
of
Doctor of Philosophy

December 2014
Purdue University
West Lafayette, Indiana

To my parents.

ACKNOWLEDGMENTS

On the journey to my doctoral degree, I have been blessed by many individuals, totaling more than can be listed here.

First and foremost, I would like to thank my advisor Prof. Fuqiang Wang for his guidance and support over years with my research and my career. Prof. Wang guided me through the adventure of research with his inspiring ideas, patience in mentoring, prudent attitude towards data analysis, and critical feedback on the results. I would like to thank Prof. Wei Xie, Prof. Andrew Hirsch, Prof. Rolf Scharenberg and Prof. Brijish Srivastava for their helpful advices and discussions during the regular group meetings. I also would like to thank Prof. Denes Molnar for his valuable and fun discussions through his heavy-ion course and in regards to my thesis. I also would like to thank Prof. Matthew L. Lister to serving on my thesis committee.

I would like to express my thanks to my fellow graduate students in heavy-ion group for their daily discussions: Tyler Browning, Liang He, Xin Li, Kun Jiang, Kurt Jung, Michael Skoby, Deke Sun, Jian Sun, Quan Wang. I received much encouragement and help from Joshua Konzer from the beginning of my studies through when he graduated. I feel grateful to David Garand for providing feedback on my presentations and paper works. I would like to thank Mustafa Mustafa for teaching me the STAR software and sharing his interesting stories. I also would like to give my thanks to our group member Lingshan Xu and non-group member Yanzhu Ji for their friendship and joyful memories together.

I am thankful to the STAR collaborators who helped me with my thesis work and who taught me a great deal in heavy-ion physics: the jetlike correlation PWG convenor Saskia Mioduszewski, the bulk correlation group convenor and nonflow paper GPC chair Hiroshi Masui, the d+Au ridge paper GPC chair Nu Xu and members

Helen Caines and Daniel McDonald. I also would like to thank Zhangbu Xu for introducing me to the heavy-ion field when I was in college.

Finally I would like to thank my parents for their understanding and love.

TABLE OF CONTENTS

Page

LIST OF TABLES

Table Page

LIST OF FIGURES

ABBREVIATIONS

ADC	Analog-to-Digital Converter
BBC	Beam-Beam Counter
BNL	Brookhaven National Laboratory.
CTB	Central Trigger Barrel
dca	distances of closest approach
FTPC	Forward Time Projection Chamber
QCD	Quantum Chromodynamics
QGP	Quark Gluon Plasma
LHC	Large Hadron Collider
RP	Reaction Plane
RHIC	Relativistic Heavy Ion Collider
STAR	Solinoid Tracker At RHIC
TPC	Time Projection Chamber
MB	Minimum Bias Trigger Data
ZDC	Zero Degree Calorimeter

ABSTRACT

Yi, Li Ph.D., Purdue University, December 2014. Study Quark Gluon Plasma by Particle Correlations in Heavy Ion Collisions. Major Professor: Fuqiang Wang.

A strongly interacting Quark Gluon Plasma (QGP) is created in relativistic heavy ion collisions at the Relativistic Heavy Ion Collider (RHIC). Two-particle (dihadron) angular correlations have been used to study the properties of the QGP. The two major contributions to the dihadron correlations are jet correlations and correlations due to anisotropic collective flow of the QGP. While jet correlations probe jet-medium interactions in the QGP medium, anisotropic flow provides information about the thermodynamic properties of the QGP. The third harmonic flow (v_3) is sensitive to the ratio of the shear viscosity to entropy density of the QGP medium and the initial energy density fluctuations. This thesis provides the first v_3 measurement in Au+Au collisions at $\sqrt{s_{\rm NN}} = 200$ GeV from the STAR experiment. The $\Delta\eta$-gap, multiplicity and p_T dependence of the v_3 are reported along with comparisons with hydrodynamic predictions.

In heavy ion collisions, the two-particle cumulant flow measurement is contaminated by nonflow correlations, such as jet correlations. An accurate flow measurement is crucial for the determination of the QGP shear viscosity to entropy density ratio. This thesis provides a data-driven isolation of $\Delta\eta$-dependent and $\Delta\eta$-independent components in the two-particle cumulant measurement. The $\Delta\eta$-dependent term is associated with nonflow, while the $\Delta\eta$-independent term is associated with flow and flow fluctuations. It is found that in 20-30% centrality Au+Au collisions, the flow fluctuation is 34% relative to flow, and the nonflow relative to flow square is 5% with $\Delta\eta$-gap > 0.7 for $0.15 < p_T < 2$ GeV/c at $|\eta| < 1$.

The recent observations of a long-range $\Delta\eta$ correlation (the ridge) in $p+p$ and p+Pb collisions at the Large Hadron Collider (LHC) raised the question of collective flow in these small systems, which had been considered control experiments for heavy-ion collision studies. This thesis provides a careful analysis of short- and long-range two-particle correlations in d+Au collisions at 200 GeV from the STAR experiment. The event activity selection affects the jetlike correlated yield in the d+Au collisions. Therefore, a simple difference between high- and low-activity collisions cannot be readily interpreted as nonjet, anisotropic flow correlations. This thesis reports the near-side ridge yield as a function of multiplicity and $\Delta\eta$, and its ratio to the away-side jet dominated correlated yield, as well as the ratio to the underlying event multiplicity. This thesis also analyzes the dihadron azimuthal correlations in terms of Fourier coefficients V_n. The V_2 is found to be independent of event multiplicity and similar between Au-going and d-going forward/backward rapidities. These dihadron correlation measurements in d+Au collisions should provide insights into the theoretical understanding of the physics mechanism for the near-side ridge in the d+Au system and the possible collective flow and QGP formation in these systems.

1. Introduction

The fundamental constituents of nuclear matter are quarks and gluons, together called partons. Gluons mediate the strong force between quarks. Since the strong force between quarks increases with the distance of separation, quarks and gluons are confined within hadrons as color neutral objects [1–3]. Free quarks or gluons have never been observed. However, Quantum Chromodynamics (QCD) [4–7], the fundamental theory governing the strong interaction, predicts that quarks and gluons can exist in deconfined state, called the Quark Gluon Plasma (QGP) [8–11]. The QGP is a plasma in which quarks and gluons can move in an extended volume without being restricted to the hadron size. Relativistic heavy ion collisions are used to create and study such a QGP state in the laboratory.

1.1 Quark Gluon Plasma

The attractive force between a quark-antiquark pair is roughly constant at large distances. The gluon binding potential between quark and antiquark is therefore proportional to their distance. The linear potential confines the quarks within the hadron size at zero temperature, since more energy is needed when the distance increases [12, 13]. As a long distance feature of QCD, the confinement prevents the isolation of a single quark. When one tries to isolate a single quark from a hadron, for example, the gluon field between the quark and the rest of the hadron becomes energetic enough that a quark-antiquark pair is created that separates the gluon field into two regions. A new hadron is created in this process which confines the quark preventing the creation of an isolated, free quark.

Deconfinement can occur at high nuclear densities. When the nuclear matter density is high enough, the hadrons are compressed into one another. The quarks cannot identify their original partners in the hadron anymore, as they find a considerably large number of neighboring quarks in their former hadron radius (see Fig. 1.1). The attractive potential between quarks is a function of their distance. At high nuclear matter densities, when the distance between quarks and their new neighbors is short enough, the attractive potential becomes small. The quarks can therefore move over the extended volume. This change in quark motion can also occur at high temperatures. At high temperature many extra particle-antiparticle pairs can be produced, which effectively makes the boundaries between hadrons disappear.

Another way to look at the transition from confinement to deconfinement is through its similarity to the Debye screening effect in electric plasmas. In dense plasma, each ion is surrounded by other ions and electrons. The effective Coulomb potential between the ion and an electron some distance away is screened by the surrounding ion and electron cloud with vanishing net charge. The effective potential decreases as the charge density increases. In this case, the bound state of ion and electron becomes dissolved. The color screening in QGP is similar to the Debye screening in the electric plasma by substituting the electric charge with QCD color charge. The difference between them is the interaction properties of the force carrier. While photons in electromagnetism do not interact between themselves, gluons interact with each other in QCD. The consequence of this self-interaction property of the gluons is that the QCD binding energy is $\propto r$, while the Coulomb potential is $\propto \frac{1}{r}$ at large distances.

1.2 Heavy Ion Collisions

Ultra-relativistic heavy ion collisions were proposed as a means to create the QGP [15]. The QGP exists at high temperatures (> 170 MeV $\approx 2 \times 10^{12}$ Kelvin [16,17]) or large baryon number densities (a few times the nuclear matter density). (Quarks and antiquarks have baryon numbers of $\frac{1}{3}$ and $-\frac{1}{3}$, respectively. The baryon number of a system is the sum of the baryon numbers of all its constituents.) As a result, there

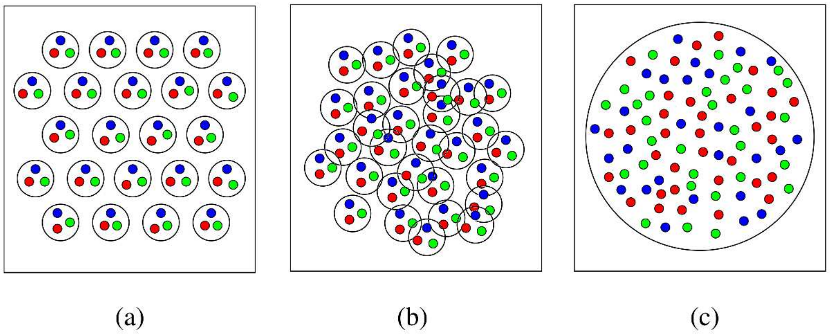

(a) (b) (c)

Figure 1.1. With increasing nuclear matter density, matter changes from nuclear to quark matter. Figure motivated by [14].

are generally two ways to achieve the high energy density for the QGP to form. One is to increase the temperature for particle-antiparticle production without increasing the net baryon number. The other is to compress the system of many nucleons with an increase of the baryon number density.

Since normal nuclear matter is at a comparatively low temperature (for comparison, the center of the Sun is at 11×10^6Kelvin $\approx 10^{-3}$ MeV) and low baryon number density (~ 0.17 per cubic fermi $= 0.17 \times 10^{-45} m^{-3}$), the QGP is not present in normal environments. Ultra-relativistic heavy ion collisions create the QGP primarily through the increase of temperature. In ultra-relativistic heavy ion collisions, two nuclei are accelerated close to the speed of light (99.995% c) and are thus Lorentz contracted. When they collide with each other, the nuclei slow down through, naively speaking, multiple inelastic nucleon-nucleon collisions, depositing energy into the collision zone. If the energy density reaches the critical value ($\sim$ 1 GeV/fm^3 predicted from QCD [15]) of the phase transition, the QGP is predicted to form. After a collision, high energy nucleons (the baryonic matter) still have substantial forward/backward momentum and thus end up substantially far away from the collision zone. Therefore, the net baryon number in the collision zone is small, while the matter created is at an extremely high temperature. The collision process is illustrated as the curve in Fig. 1.2, starting from the hadronic matter (nuclei), rising in temperature with low net baryon density into the QGP phase, and then returning to the hadronic phase in the end. In contrast, proton-proton ($p + p$) collisions at similar energies deposit less energy since there is only one nucleon-nucleon interaction.

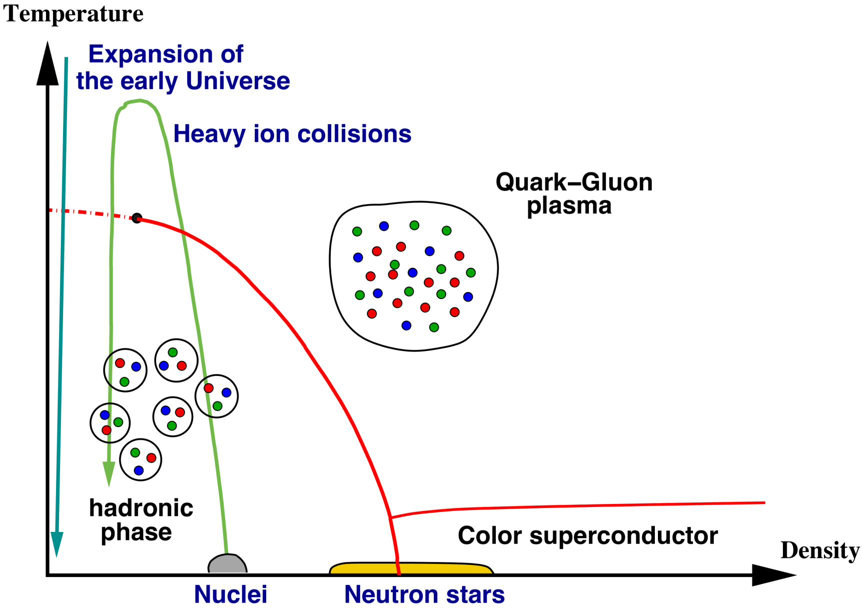

Figure 1.2. A schematic view of the nuclear matter phase diagram in QCD. Figure taken from [18].

In a relativistic heavy ion collision where the QGP is formed, the system evolves through several space-time stages as depicted in Fig.1.3. The inelastic nucleon-nucleon collision happens through parton-parton (quark or gluon) scattering. The QGP is formed within $\sim 1\text{fm}/c$ after the collision. The system begins to thermalize by further partonic scattering. As the scattering continues, the system expands in both longitudinal and transverse directions. The temperature decreases as the system expands. The photons and leptons radiated from the color QGP medium leave the system without further (strong) interactions in the QGP. When the temperature drops below the phase-transition critical value, the system starts to convert back into a hadronic state, in the form of baryons and mesons. The hadronization happens at ~ 10 fm/c. After hadronization, the system enters the hadron gas state. In the hadron gas state, hadronic inelastic scatterings change the particle species at the level of hadrons instead of partons. When further hadronic inelastic scattering ceases, particle species is frozen. As the system further expands, the average distance between particles increases. Particle elastic scatterings continue until their distance is too large. Finally, the elastic scattering ceases and particles stream freely into the detector and are recorded. The experimental observables are the charge, momentum and energy of each final state particle reconstructed with the detectors. The final state particles carry the information about the QGP as well as the various stages of evolution.

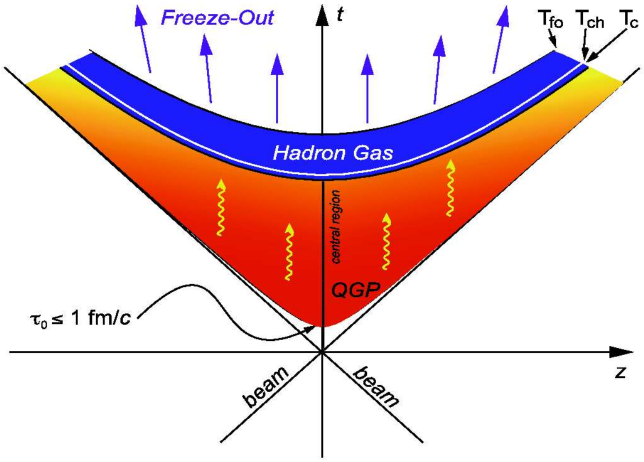

Figure 1.3. Schematic view of the QGP space-time evolution. T_c is the critical temperature for the QGP to turn into hadrons. T_{ch} is the temperature when hadrons stop inelastic collisions and their hadron species become fixed. T_{fo} is the temperature when hadrons stop having elastic collisions and free-stream to the detectors. Figure taken from [19].

The primary goal of the high energy heavy ion collision program is to create the deconfined QGP and to investigate the QGP's properties, such as the temperature and order of the phase transition, the equation of state, and the transport properties.

1.3 Collective Flow

During the QGP expansion, the partons are found to move collectively (flow phenomenon), and hydrodynamics have been used to describe such collectivity behavior [20]. There are several forms of flow: the longitudinal flow, the axially symmetric radial flow, and the azimuthal anisotropic flow. The first harmonic anisotropic flow is called the dipole/directed flow. The second harmonic anisotropic flow is called the elliptic flow. The third anisotropic flow is called the triangular flow. The longitudinal flow will not be discussed in this thesis, but some studies of it can be found in [21,22]. The radial flow and the anisotropic flow are in the transverse plane. Radial flow is caused by the QGP expansion in the radial direction. The amount of radial flow is generally governed by the particle interaction cross sections with others (or in hydrodynamic language, viscosity). For particles of similar cross sections, a common radial flow velocity is customarily assumed. The heavier particles receive a larger boost from the common radial flow velocity. The radial flow has been used to study kinetic freeze-out information and the QGP equation of state [23,24]. The directed flow (or dipole flow) is the collective sidewards deflection of particles, as illustrated in Fig. 1.4. It was first observed in Ca + Ca and Nb + Nb collisions at 400 MeV/nucleon in the early 1980's [25]. The directed flow probes the pre-equilibrium and the thermalization stage as well as the initial-state fluctuation. The directed flow is small in the mid-rapidity region in high energy heavy ion collisions. The directed flow measurements can be found in [26–30]. This thesis focuses on the azimuthal anisotropic flow, particularly the elliptic and triangular harmonic flows. In the following context, the word 'flow' refers to anisotropy flow.

In a semicentral collision, the pressure gradient is not uniform in azimuthal angle. Figure 1.5 shows the geometry of the overlap collision zone of two nuclei in the beam view. In spatial coordinates, the collision zone is almond shaped. The standard eccentricity of the overlap zone is defined by [32]

$$\epsilon_2 = \frac{\langle y^2 - x^2 \rangle}{\langle y^2 + x^2 \rangle}, \tag{1.1}$$

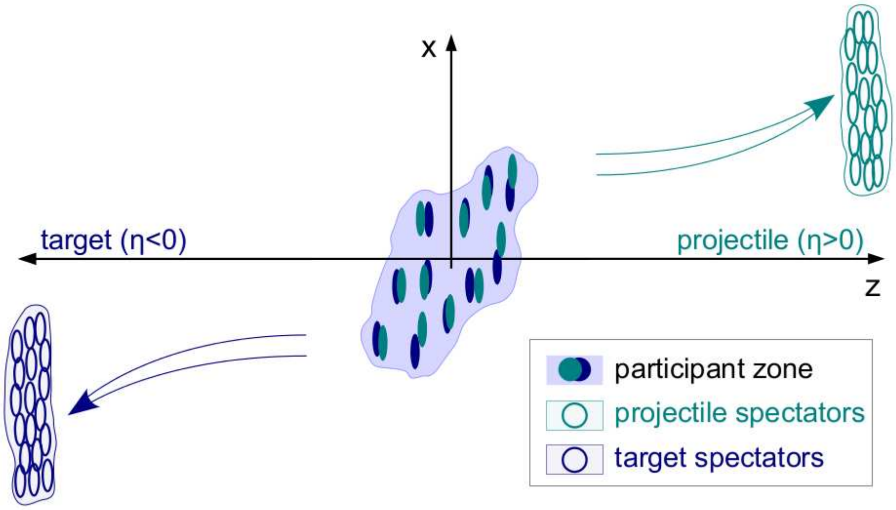

Figure 1.4. Distribution of nucleons on the reaction plane. The collision axis is the z direction. The spectators are the particles which do not interact. The nuclear matter distribution in the participant collision zone has a sidewards deflection. Figure taken from [31].

where (x, y) is the spatial position of a participant nucleon. The angle brackets are the average over all participant nucleons with unity weight. Other average definitions can be found in reference [33–35]. The pressure gradient along the x axis is larger than that along the y axis. Because the pressure gradient drives the direction of the expansion, as the system evolves, the particles gain a larger momentum along the x axis than the y axis. The spatial anisotropy is thus transferred into a momentum anisotropy. The response of the final momentum anisotropy to the initial spatial anisotropy depends on the interaction strength among the constituents, or the particle mean free path relative to the size of the collision system. When the mean free path is much larger than the size of the system, particles do not interact, and therefore are unaware of the spatial geometry of the system. Hence, the particle momentum directions would be uniform, and would be the same as they are initially produced. When the mean free path is small relative to the system size, the information of the system's spatial distribution will be propagated to the particle momenta via interactions. The relative value of the mean free path to the system size is related to the shear viscosity. The smaller mean free path, the smaller shear viscosity. The comparison of the final anisotropy to the initial one, therefore, provides information about shear viscosity of the system. In addition to the overall geometry, there are event-by-event fluctuations in the geometry of the collision zone (e.g. hot spots). There exist higher order harmonics in the energy density distribution. The different order of coefficients respond differently to the system shear viscosity. Therefore, the flow information can be used to constrain the QGP viscosity.

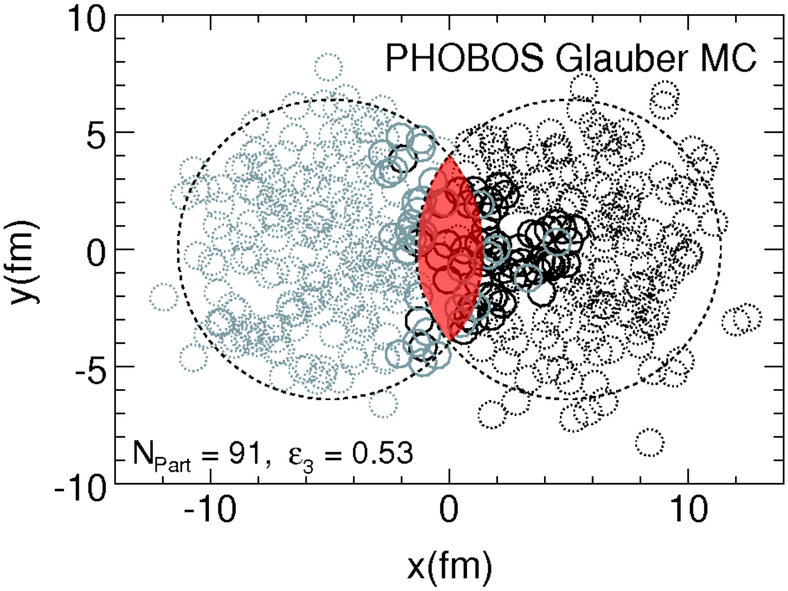

Figure 1.5. Distribution of nucleons in the transverse plane. The red shaded area indicates smooth geometry overlap, while the dark circles indicate interacting nucleons (thereby defining the collision zone). Figure taken from [36].

The particle momentum angular distribution can be written as a Fourier series:

$$\frac{dN}{d\phi} = \frac{N}{2\pi}[1 + 2v_1 \cos(\phi - \Psi_1) + 2v_2 \cos 2(\phi - \Psi_2) + 2v_3 \cos 3(\phi - \Psi_3) + \cdots] \quad (1.2)$$

$$= \frac{N}{2\pi}[1 + \sum_{n=1}^{\infty} 2v_n \cos n(\phi - \Psi_n)], \quad (1.3)$$

where ϕ is the particle azimuthal angle. The v_1 is the directed flow; the v_2 is the elliptic flow; the v_3 is the triangular flow. They describe the magnitudes of particle momentum anisotropy. Ψ_n are the corresponding harmonic azimuthal angles. Of particular interest is the Ψ_2, called the second harmonic plane or second order of participant plane, which is determined by the initial participant nucleon (or parton) configuration [37]. In Fig.1.5, the short x axis is the reaction plane, and the z axis is the beam axis. Due to fluctuations, Ψ_2 may not be the same as the reaction plane (the plane determined by the beam direction and geometry centers of the two nucleons, which is the x axis in Fig. 1.5). The v_2 is the dominant term when the collision geometry is almond shaped. The v_3 is the third harmonic flow, which is zero due to symmetry if the overlap region is smooth. Each v_n would have their own harmonic plane Ψ_n. The measurements of v_2 and v_3 are the main focus in this thesis.

Because the harmonic planes Ψ_n are not known a priori, v_2 and v_3 cannot be calculated directly from the single particle distribution as in Eq. (1.2). However, they can be obtained from two-particle correlations as follows. When single particle distribution follows Eq. (1.2), the two-particle distribution is given by

$$\frac{dN_{pair}}{d\Delta\eta} = \frac{N_{pair}}{2\pi}[1 + \sum_{n=1}^{\infty} 2V_n\{2\} \cos n\Delta\phi] \tag{1.4}$$

$V_n\{2\} = v_n^a \cdot v_n^b$ if there is only flow correlation (see discussion in Chapter 4). Here a, b stand for the two sets of particles used in the correlation measure (where $\Delta\phi$ is the azimuthal opening angle between the two particles). When choosing a and b from the same kinematic region, v_n can be calculated by [38]:

$$v_n\{2\} = \sqrt{\left\langle \frac{\sum_{i,j=1,i\neq j}^{M} \cos n(\phi_i - \phi_j)}{M(M-1)} \right\rangle}, \tag{1.5}$$

where ϕ_i, ϕ_j are the azimuthal angles of particle pairs used for the correlation measurement; M is number of particles used. First the average over M particles in each event is taken, then the average over all events is taken (The weight used to average over all event can be the number of pairs or unity, If the number of pairs, $M(M-1)$, is used as the weight in the event average, then the calculation is equivalent to taking a single average over all pairs from all events). The v_2 and v_3 calculated from two particle correlations are called the two-particle cumulant flow. In a similar manner, one can also calculate v_n from four-particle correlations (see Chapter 4).

1.4 Jet-medium Interactions

One way to probe the QGP is to measure how the jets are modified as they interact with the QGP medium while traversing the medium. A parton in a projectile nucleon interacts with a parton in a target nucleon. Occasionally large momentum transfers occur. A large momentum-transfer scattering is called hard scattering. In contrast, if the momentum transfer is small, the process is called a soft scattering. In a hard scattering, the large longitudinal energy is transferred into the transverse plane. The final partons thus gain large transverse momenta. Each final parton later fragments into a shower of partons. In the QGP medium, these partons exchange both momentum and color with the QGP. The color medium modifies the parton shower if it propagates through the QGP. These partons eventually hadronize into a cluster of hadrons, often called jets.

Jets as a probe for the QGP have two primary advantages. First, jets are produced from partonic scatterings involving large momentum transfers. Jet production can therefore be calculated by using perturbative QCD, while the soft process can not. Second, jets are generated in hard scatterings on a very short time scale $\sim 1/Q_T \sim 0.1\ fm/c$ or less [39] for momentum transfer $Q_T = 2$ GeV/c. The jets have enough time to interact with the QGP, while they can also interact with the system before the system is thermalized. By exploring how jets are modified, information can be gained about the QGP medium.

On the other hand, the jet as a probe is also complicated. First, the partons in a jet suffer from a complex time evolution, even in a vacuum without QGP. They subsequently radiate gluons and can also split into quark and anti-quark pairs. As a result, the nature of partons in a jet evolves as a function of time by branching into more partons. Second, the QGP medium has a collective motion. The measured jet correlations have a flow background. Third, the QGP medium is not static. The medium expands rapidly and its temperature decreases. The interaction of jets with the dynamic medium is a challenging theoretical undertaking.

The first challenge above can be addressed by the following comparisons. Since the final measurement is the output of jet-medium interactions, it is necessary to understand the jet's behavior in the absence of the medium as a baseline. $p+p$ collisions can be used as the vacuum baseline because QGP is generally not expected to form in p+p collisions. Moreover, the parton distributions (except for low-x gluons) in the nucleon, the partonic hard process cross sections and the fragmentation of partons into hadrons are well understood [40]. Nonetheless, there is a defect in using $p+p$ collisions as the baseline. The initial multiple soft scattering effect in heavy ion collisions, usually called the Cronin effect [41], is not included in $p+p$ collisions. One way to include the Cronin effect in the baseline is to study proton-nucleus (pA) or deuteron-nucleus (dA) collisions. In pA or dA collisions, the Cronin effect is present, while the QGP is generally not expected to form in such a small system. (However, there is a report of the possible formation of small droplets of QGP in p+Pb at the LHC energy. The search for the QGP in $d+Au$ collisions at RHIC will be discussed in Chapter 5.)

The resolution to the second challenge can be considered from two perspectives. From the experimental side, one can analyze the medium's collective motion, namely flow. By subtracting the flow, one will expect to obtain a clearer jet signal. From the theoretical point of view, a dynamic description of the jet-medium interactions should be incorporated. The third aforementioned challenge can also be addressed by realistic theoretical investigations. By comparing experimental measurements of jets and jet correlations to realistic and rigorous theoretical model studies, one hopes to learn valuable information about the QGP.

1.5 Two-particle $\Delta\eta$-$\Delta\phi$ Correlation and the Ridge

This section describes two-particle $\Delta\eta$-$\Delta\phi$ correlations and discusses the ridge structure and the away-side shoulder in heavy ion collisions.

1.5.1 Why to Measure Two-particle $\Delta\eta$-$\Delta\phi$ Correlation

Two-particle correlations have been used to study jets and jet-medium interactions. Ideally fully reconstructed jets tell a more complete story on how a jet interacts with the QGP medium than two-particle correlation studies. Figure 1.6 left panel shows a reconstructed back-to-back jet event with one leading jet and one less energetic, subleading jet at the Large Hadron Collider (LHC). However, it is practically difficult to reconstruct a pure jet in heavy ion collisions, due to the large number of final particles. The jet is known to be a spray of particles which are the end products of one high energy parent parton. Instead of a parton spray, the experimental observation is the final hadrons reconstructed from the electrical signals. It is difficult to reconstruct jets for several reasons. First, the detector has finite coverage and particle detection capabilities. Not all particles can be recorded in the detectors. Second, the large number of final produced particles ($\sim$ thousands) in heavy ion collisions makes it harder to distinguish which ones are from a jet, which are from the medium, and which are from the interaction between the jet and the medium. Third, the different jet reconstruction algorithms generally lead to different jet results, because different jet algorithms may identify a jet with different particle constituents.

Because of these difficulties, high p_T particles are often used as a substitute for jets since they are usually the leading fragment of the jet. (At RHIC energy, a particle with p_T larger than 3 GeV/c is considered to be a high p_T particle.) The ratio of the high p_T particle yield in heavy ion collisions relative to the yield in $p+p$ or d+Au baselines normalized by the number of binary collisions, called the nuclear modification factor, is found to be less than unity [42,43]. The suppression of the single particle spectra at high p_T in heavy ion collisions indicates jet energy loss in the QGP. The suppression is often referred to as the jet-quenching phenomenon. However, the high p_T single particle spectra method has two kinds of bias by design. First, in order to have one high p_T daughter particle, the selected high p_T parent parton tends to give most of its energy to the daughter particle in hard fragmentation. Such a bias exists in heavy ion collisions as well as in $p+p$ collisions [44]. Second, for jets in heavy ion collisions, there is an additional bias: the surface bias. The surface bias is illustrated in the right panel of Fig. 1.6. The jet interacts with the medium and loses energy. The amount of energy loss depends on the path length the jet traverses through the medium. When triggered on high p_T, the jets with the shortest path length are more likely to be selected because they lose less energy. These jets are mostly generated near the surface of the medium. As a result, they provide minimal information about the medium, since they have interacted little with the medium. This surface bias limits the usefulness of these leading jets, but high p_T particles can be used for the nuclear modification study as mentioned previously. On the other hand, due to momentum conservation, there is a recoil jet associated with the triggered high p_T jet. While the triggered high p_T particle has less interaction, the particle in the recoil jet likely has maximal interaction with the QGP medium because they have the longest path length to traverse in the QGP. By studying the particles in the recoil jet, one can gain more information about jet-medium interactions. Two-particle correlations are used to study the recoil jet associated with the trigger jet. The combination of high p_T single particle spectra and two-particle correlations prove to be a powerful tool to shed light on how jets lose energy in QGP.

1.5.2 Two-particle $\Delta\eta$-$\Delta\phi$ Correlation Method

Two-particle $\Delta\eta$-$\Delta\phi$ correlations measure the momentum angular distributions of the associated particles relative to the trigger particle. A trigger particle is usually defined as a particle with high p_T, which is likely from a jet. An associated particle is correlated with the trigger particle identified in a collision and it is usually a lower

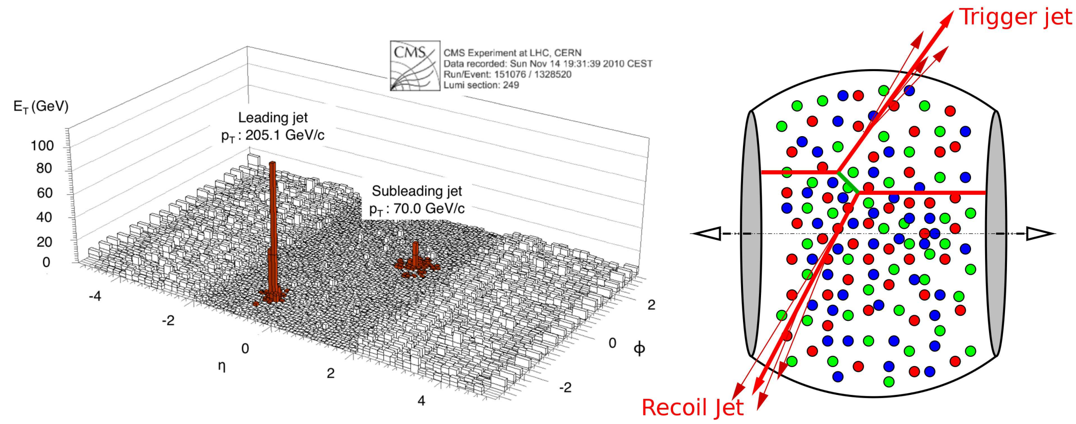

Figure 1.6. Left panel: a reconstructed dijet event in Pb+Pb collisions by CMS experiment [45]. The hard scattering producing the jets occurs near the edge of the fireball. One of the jets (the trigger jet) leaves the medium soon after its formation and thus escapes without much further interaction with QGP, while the other one (the recoil jet) traverses the medium and is strongly modified by the medium. Figure taken from [18].

p_T particle which may be from the same jet or the recoil jet, the medium or the jet-medium interaction. There are also cases when both the trigger and associated particles are low p_T particles. The low p_T two particle correlation is sometimes referred as the untriggered two-particle correlation, which is often used to study medium properties. Two dimensions will be discussed: $\Delta\phi = \phi_{\text{assoc}} - \phi_{\text{trig}}$ is the azimuthal opening angle between the trigger and associated particles; $\Delta\eta = \eta_{\text{assoc}} - \eta_{\text{trig}}$ is the pseudo-rapidity separation between the particles. The region $\Delta\phi \approx 0$ is called the near side, where the associated particle azimuthal angle is similar to the trigger particle angle. The particles in the same jet as the trigger particle usually end up in the near side. The region $\Delta\phi \approx \pi$ is called the away side. The particles from the recoil jet are on the away side. The $\Delta\eta$-$\Delta\phi$ two-particle (dihadron) correlation is given by

$$C(\Delta\eta, \Delta\phi) = \frac{1}{N_{trig}} \frac{d^2N}{d\Delta\eta d\Delta\phi} = \frac{1}{N_{trig}} \frac{S(\Delta\eta, \Delta\phi)/\epsilon_{\text{assoc}}}{B(\Delta\eta, \Delta\phi)/\langle B(\Delta\eta|_{100\%}, \Delta\phi)\rangle}. \tag{1.6}$$

Here $S = \frac{d^2N^{\text{same}}}{d\Delta\eta d\Delta\phi}$ is the raw dihadron correlation for pairs in the same event; and $B = \frac{d^2N^{\text{mix}}}{d\Delta\eta d\Delta\phi}$ is for trigger and associated particles from different events, which is called mixed event correction. $\langle B\rangle$ is the B average over $\Delta\phi$ at fixed $\Delta\eta|_{100\%}$. $\Delta\eta|_{100\%}$ is where the two-particle acceptance is 100%. The mixed event background serves as the correction for the detector's two-particle acceptance. For a 4π coverage with detection efficiency $\epsilon_{\text{assoc}} = 100\%$, $C(\Delta\eta, \Delta\phi) = \frac{S(\Delta\eta,\Delta\phi)}{N_{trig}}$. While the mixed event background does not contain the particle correlation existing in the same collision, it includes the detector acceptance information. Taking STAR experiment's Time Projection Chamber (TPC) as an example, there are 12 sectors in ϕ. The sector boundaries are the dead zones for particle detection. Particle tracks across the sector boundaries have a lower probability to be reconstructed. Single particle deficiencies at sector boundaries affect two-particle correlations, especially when both particles cross the sector boundaries. Similarly, for the η direction and other detectors with non-uniform detector efficiencies, the single particle efficiency affects the two-particle correlations. Since the mixed event is also affected by the single particle detecting efficiency, the raw dihadron correlation in the same event divided by the mixed event correlation can correct for the non-uniform detector efficiency. Meanwhile, detector has limited η acceptance. The STAR TPC has a good detection capacity in $-1 < \eta < 1$. The single particle η acceptance gives a triangular shape for the dihadron correlations. The mixed event background also corrects the triangular shape in $\Delta\eta$. The mixed event dihadron correlation normalization is 100% at $|\Delta\eta|_{100\%} = 0$ when both the triggered and associated particles are in the TPC. The mixed events are required to have primary vertices close to each other in the beam direction to resemble similar detector acceptance, and to have similar event characteristics, such as a similar number of particles. After dividing by the mixed event background, the dihadron correlation in Eq. (1.6) is normalized by the total number of trigger particles used in the correlation study. The per trigger particle normalized dihadron correlation describes, on average, how many associated particles distributed in $\Delta\eta$-$\Delta\phi$ space for each trigger particle.

The underlying event contribution, which is a flow modulated background, is subtracted from the per trigger dihadron correlations in Eq. (1.7) in order to obtain the jet correlation. The dihadron correlation is the sum of jetlike and flow correlations:

$$C(\Delta\eta, \Delta\phi) = C_{background}(\Delta\eta, \Delta\phi) + J(\Delta\eta, \Delta\phi); \tag{1.7}$$

$$C_{background}(\Delta\eta, \Delta\phi) = B_{ZYAM}(\Delta\eta)(1 + 2\langle v_2^{trigger} v_2^{assocated}\rangle \cos(2\Delta\phi)). \tag{1.8}$$

Here $C(\Delta\eta, \Delta\phi)$ is the measured dihadron correlation after the mixed event correction. $C_{background}(\Delta\eta, \Delta\phi)$ is the medium contribution to the dihadron correlation. $J(\Delta\eta, \Delta\phi)$ is the dihadron correlation from the jetlike particles. The medium contribution $C_{background}(\Delta\eta, \Delta\phi)$ is a uniform background with flow modulation in $\Delta\phi$ for each $\Delta\eta$. Eq. (1.8) gives the expression which includes only elliptic flow modulation where $v_2^{trigger}$ and $v_2^{associated}$ are the elliptic flow for the trigger and associated particles, respectively. The elliptic flow $v_2^{trigger}$ and $v_2^{associated}$ can be measured using several methods, such as the event-plane, the generating function, or the Q-cumulant method [38]. The difference between flow measurements is usually treated as systematic uncertainties. Normalization B_{ZYAM} is the uniform background value at each $\Delta\eta$, usually estimated by the Zero Yield At Minimum (ZYAM) method [46]. ZYAM background B_{ZYAM} is estimated based on the assumption that the jet correlated yield is zero at its minimum:

$$J(\Delta\eta, \Delta\phi = \Delta\phi_{min}) = 0. \tag{1.9}$$

For various $\Delta\eta$, the jet yield minima $J(\Delta\eta, \Delta\phi = \Delta\phi_{min})$ can have different values, at different $\Delta\phi_{min}$.

The high p_T dihadron $\Delta\eta$-$\Delta\phi$ correlation measurement shows a strongly suppressed away-side jet peak with a minimally modified near-side jet peak in central Au+Au collisions at $\sqrt{s_{NN}}$ =200 GeV, as reported in [47, 48]. The near-side peaks, inspected in $p + p$, d+Au and in all centrality (Section 2.2.5) classes of Au+Au collisions, characterize the hard scattering processes. Clear away-side peaks for the high p_T particles exist in p+p, d+Au and peripheral Au+Au collisions. In contrast, the away-side peak for high p_T particles in central Au+Au collisions is remarkably diminished. The observation of the disappearance of high p_T away-side peak in central Au+Au collisions indicates that the recoil jet loses significant energy when traversing the QGP.

1.5.3 Near-Side Ridge

The ridge was first discovered in central Au+Au collisions at $\sqrt{s_{NN}} = 200$ GeV at the RHIC by the STAR experiment [49]. The dihadron $\Delta\eta$-$\Delta\phi$ correlation was initially studied with high p_T trigger particles. After the subtraction of the elliptic flow background, the ridge was observed as a near-side peak at small $|\Delta\phi|$, but at large $\Delta\eta$, where jet contribution is minimal. As the top panels in Fig. 1.7 show [50], beside the near-side jet peak at small $|\Delta\eta| < 1$, there is a ridge on the near-side which is uniform in $\Delta\eta$ at large $|\Delta\eta| > 1$ in the STAR TPC acceptance $-2 < \Delta\eta < 2$ for both $3 < p_T^{trigger} < 4$ GeV/c and $4 < p_T^{trigger} < 6$ GeV/c in Au+Au central collisions. The ridge structure in the $\Delta\eta$ region of the near-side jet peak is unknown. The naive expectation is that the ridge is also approximately uniform at $|\Delta\eta| < 1$. The PHOBOS experiment measured the dihadron correlations in their detector coverage $-4 < \Delta\eta < 2$ with $p_T^{trigger} > 2.5$ GeV/c and inclusive associated particle p_T, and found that the near-side ridge reaches up to at least $|\Delta\eta| \approx 4$ in central Au+Au collisions. The ridge yield is found to be largely independent of $\Delta\eta$ within their detectors $\Delta\eta$ acceptance. The multiplicity dependence of the ridge shows that the ridge yield decreases towards peripheral collisions, and that the yield is zero when the collision has fewer than 100 participating nucleons for $p_T^{trigger} > 2.5$ GeV/c [51]. In contrast, there is no ridge in minimum bias d+Au collisions, as shown in the bottom panels of Fig. 1.7. There is also no ridge observed in minimum bias $p+p$ collisions at $\sqrt{s_{NN}} = 200$ GeV [49]. The near-side ridge discovered in central Au+Au collisions has three major features: long rapidity range, relatively small azimuthal angle $\Delta\phi$, and existence in events with a large number of particles.

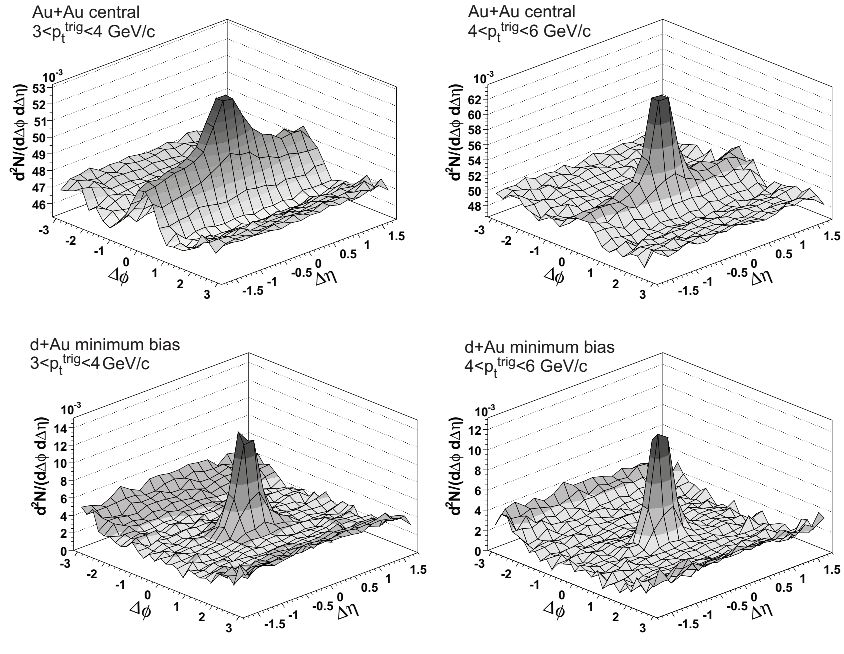

Figure 1.7. Dihadron $(\Delta\eta, \Delta\phi)$ correlations in d+Au (lower panels) and Au+Au (higher panels) $\sqrt{s_{\mathrm{NN}}} = 200$ GeV per nucleon. Figure taken from [50].

Further studies, which is discussed below, suggest the soft origin of ridge physics (soft standing for small momentum transfer). The two major contributions in dihadron correlations are jet and flow correlations. Flow correlations are the soft physics phenomenon. In contrast, jets are the hard process. While the first ridge measurement was done with high p_T trigger particles, further dihadron correlation measurements with low p_T particles showed that the ridge also exists for soft particles [52]. The ridge with soft particles suggests that the jet may not be essential for the near-side ridge. One should note, however, that soft near-side ridge measurements do not preclude a jet origin, since jets also fragment into low p_T particles. Several measurements have been conducted to investigate whether the near-side ridge is originated from jet physics or not by comparing the behaviors of jet and ridge. Jet correlations from hard scattering have charge dependence. Dihadron correlations from jets are stronger for pairs with opposite charges (unlike-sign) than pairs with the same charge (like-sign) due to charge conservation. The near-side ridge, however, is found to be the same for both unlike-sign and like-sign pairs so ridge behaves differently from dihadron correlations in jets [52]. On the other hand, there is a strong correlation between the jet yield and the trigger particle p_T. The higher $p_T^{trigger}$ particles come from more energetic jets. However, the near-side ridge has a weaker dependence on the $p_T^{trigger}$. Additionally, the $p_T^{associated}$ spectra (particle yield distribution) of the near-side ridge is softer than the spectra from jets, but similar to inclusive particle production which is dominated by medium particles [53]. These measurements together suggest that the near-side ridge may not be due to jets, but rather, due to medium particles.

Any possible explanation for the near-side ridge needs to address both its relationship with medium particles and its angular distribution features. The medium collectivity effect in dihadron correlations is also more prominent in central collisions because of the larger multiplicity. The near-side ridge is stronger in the central collisions. Meanwhile, the ridge is similar to the medium effect as discussed above. These facts suggest the possible connection between the ridge and collective anisotropic flow (beyond elliptic flow, which has been subtracted out already). On the other hand, the larger $\Delta\eta$ rapidity requires an early stage interaction for the near-side ridge. The long range $\Delta\eta$ correlation implies that the two particles with large initial $\Delta\eta$ separation still have a connection between them in the final state. According to causality, their interaction has to happen at early times: at or instantaneously after the encounter of the colliding nuclei [54]. Moreover, the $\Delta\eta$ shape is not only long range, but also flat in $\Delta\eta$. The flatness in $\Delta\eta$ suggests that these particle correlations are produced independently in η. Flow also develops at early times [55]. Thus flow is a viable explanation for the ridge.

Another explanation for the near-side ridge in heavy ion collisions is the consequence of the early stage Glasma flux tube in concert with the later stage radial flow [54, 55]. The Color Glass Condensate (CGC) theory [56, 57] predicts that the transverse fields in the two nuclei are transformed into the so called longitudinal Glasma flux tubes right after the collision, as Fig. 1.8 illustrates. Since the particles in a Glasma flux tube are from the same transverse position in the early times of the collision, the particles fragmented from the same tube share the correlation regardless of their rapidity. Thus, the particles produced from a Glasma flux tube decay resemble the long-range flatness in $\Delta\eta$ for the near-side ridge. The small $|\Delta\phi|$ feature arises from the effect of the radial flow on the flux tube. The radial flow is the collective expansion of the QGP medium in the transverse direction. The particles from the same flux tube experience the same radial flow velocity. The common radial flow collimates the outgoing particles into a small $\Delta\phi$. The particles from the same Glasma flux tube are focused by the radial flow to form the near-side ridge at small $\Delta\phi$ independent of $\Delta\eta$.

It is worthwhile to note that, even without radial flow, CGC predicts an enhanced two-gluon density at small $\Delta\phi$. However, such an effect is too small to explain the observed heavy-ion ridge. Such effect, on the other hand, may be related to the observed ridge in small system collisions at the LHC and perhaps at RHIC as well (see Chapter 5).

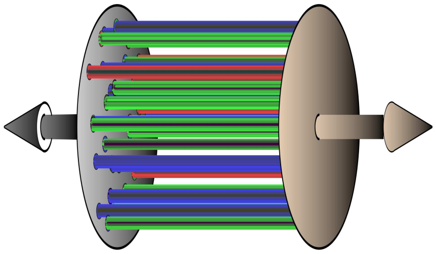

Figure 1.8. Glasma flux tubes for the collision of two nuclei. Figure taken from [54].

1.5.4 Away-Side Shoulder

The away-side shoulder is the double-peak on the away side in central heavy ion collisions [49]. Figure 1.9 shows the dihadron $\Delta\phi$ correlations in 0-20% Au+Au collisions at $\sqrt{s_{NN}} = 200$ GeV from the PHENIX experiment [58]. Since the near-side ridge and the away-side shoulder both exist in central heavy ion collisions, they could originate from the same mechanism.

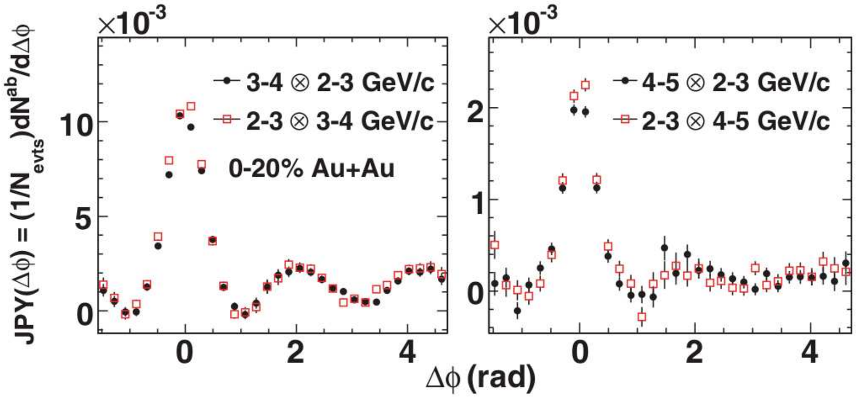

Figure 1.9. The dihadron correlated per-trigger yield $\Delta\phi$ distributions in 0-20% Au+Au collisions at $\sqrt{s_{NN}} = 200$ GeV by the PHENIX experiment. Figure taken from [58].

The away-side shoulder behavior and its components have been analyzed as below. The away-side dihadron yield per trigger is found to increase towards central collisions, similar to the near-side ridge. Meanwhile, the average p_T of the particles on the away side associated with high p_T trigger particles drops rapidly as the multiplicity increases, which means the particles in the ridge become softer in central collisions [49]. As the above two measurements show, there are more and softer particles correlated with high p_T trigger particles on the away side in central collisions than that in peripheral collisions. Moreover, the dihadron away-side yield is observed to be dependent on particle species. The baryon to meson ratio on the away side is enhanced in central collisions, and is quantitatively similar to that for inclusive particles [58].

The initial explanation for the away-side shoulder is that it is a jet-medium effect in central heavy ion collisions. One possibility is that the away-side jet is modified by the QGP and results in the double-peak structure. Another possibility is that the recombination of the correlated soft particles induced via strong jet-medium interactions causes the shoulder effect.

However, the observation of the away-side shoulder is only obtained from dihadron correlations after elliptic flow subtraction. The initial state energy density fluctuation can transform into higher order final state particle azimuthal correlations, such as the third harmonic v_3. Because the initial energy density distribution in the collision zone was previously considered as smooth and the overlap region is almond shaped, higher order odd harmonics were not expected. The v_3 contribution was thus not subtracted in the previous dihadron correlation measurements. Glauber Monte Carlo simulations reveal the lumpiness in the initial state density and the non-zero higher order harmonics in the final state, specially v_3 [36]. The hydrodynamic flow v_3 is a soft physics feature, and it gives a ridge shape on the near side and a double-peak shape on the away side. The shape of v_3 makes it the most natural explanation for both the near-side ridge and away-side shoulder.

The important question is then whether the v_3 calculated from hydrodynamics with a fluctuating initial state can quantitatively describe the experimental measurements in heavy ion collisions. Chapter 3 describes the v_3 measurement as performed in this thesis work and its comparison with hydrodynamics.

2. STAR Experiment

This thesis work is conducted with Au+Au and d+Au data taken by the STAR detector at the RHIC accelerator.

2.1 Relativistic Heavy Ion Collider

The Relativistic Heavy Ion Collider (RHIC) is located at Brookhaven National Lab in Upton, New York on Long Island. RHIC is a versatile collider. It can accelerate many species of ions to a wide range in energy. The two major physics programs at RHIC are spin physics, using polarized protons, and heavy ion physics. Reviews on the spin physics program can be found in references [59,60].

For heavy ion physics, RHIC accelerates heavy nuclei of various species to various energies. From its commissioning in 2000 to the present day (2014), RHIC has performed proton and proton ($p+p$), deuteron and gold (d+Au), copper and copper (Cu+Cu), gold and gold (Au+Au), copper and gold (Cu+Au), uranium and uranium (U+U), helium 3 and gold (He^3+Au) collisions. RHIC has conducted a beam energy scan program for Au+Au collisions at center of mass energy $\sqrt{s_{\mathrm{NN}}}$ from 7.7 GeV to the top energy of 200 GeV per nucleon pair. The various energies facilitate the search for the possible critical point of QCD phase diagram [61–64].

As Fig. 2.1 shows, there are six interaction points on RHIC's 3.8 km long storage ring, among which are four experiments. They are STAR at 6 o'clock, PHENIX at 8 o'clock, PHOBOS at 10 o'clock, and BRAHMS at 1 o'clock. While PHOBOS and BRAHMS finished their missions in 2005 and 2006, respectively, the STAR and PHENIX experiments are still operating as of 2014.

After serving as a heavy-ion collider, RHIC has been proposed as a possible facility for a future electron-ion collider to study the partonic structure of nuclei [65,66].

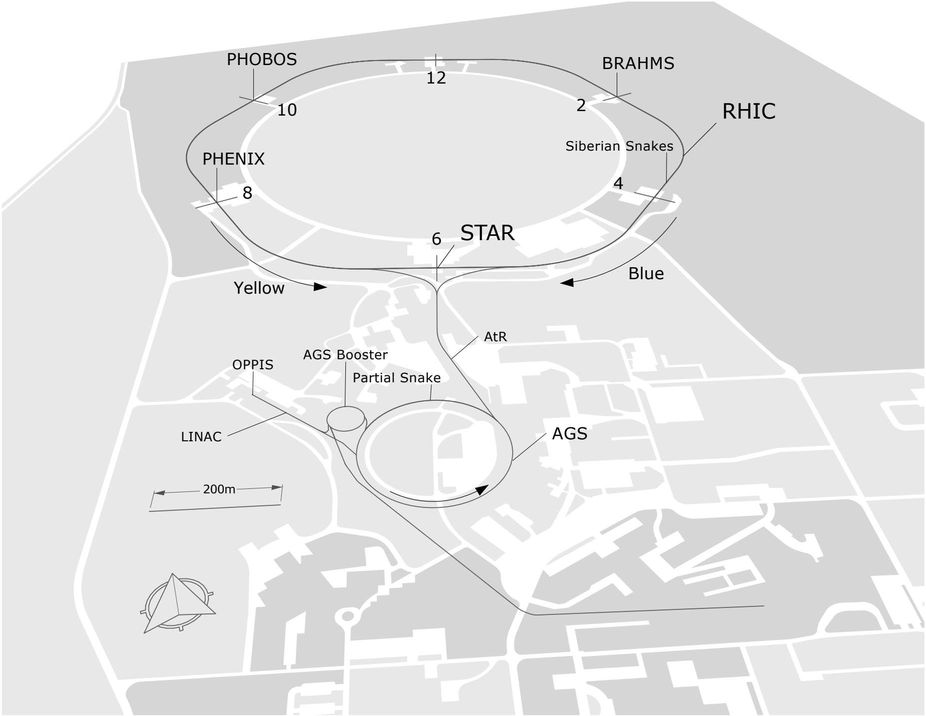

Figure 2.1. The RHIC accelerator complex. (Credit: Tai Sakuma)

2.2 STAR Detector

The Solenoidal Tracker at RHIC (STAR) detector is a general purpose detector. STAR has various detector subsystems. The main detector component is the TPC. It has full azimuthal and approximately 2.5 units of rapidity coverage. Three major detector subsystems used in this analysis are the TPC, the Forward Time Projection Chamber (FTPC) and the Zero Degree Calorimeter (ZDC), as shown in Fig. 2.2.

The conventional coordinate system at STAR uses the center of the Time Projection Chamber as the origin point. The beam pipe direction is the z direction with the west direction as being positive. The x direction is pointing to the south and the y direction is pointing up. For the d+Au collisions conducted in 2003 and 2008, the deuteron beam was going to the west, the positive z direction, and the gold beam was going to the east, the negative z direction. The azimuthal direction is in the x-y plane.

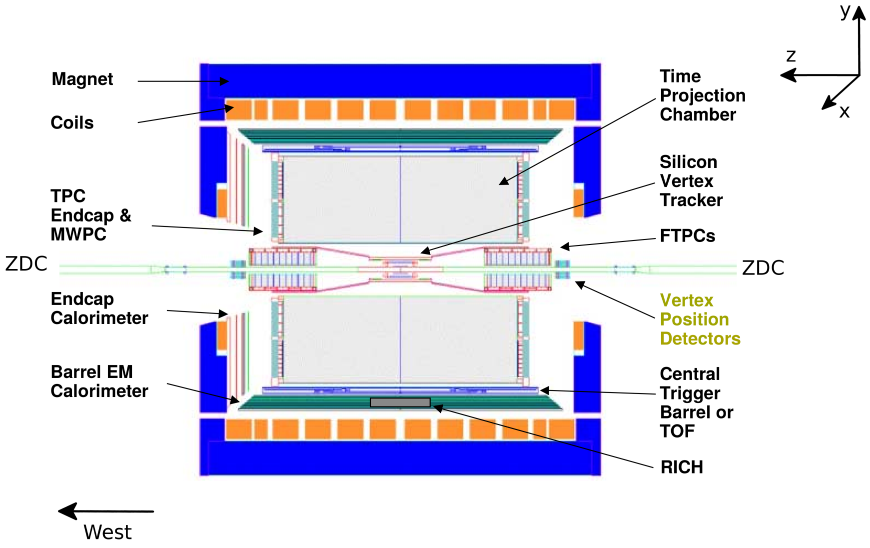

Figure 2.2. An illustration of a cutaway side view of the STAR detector. Figure modified from [67].

2.2.1 Time Projection Chamber

The TPC is the primary tracking detector at STAR [68]. The TPC records charged particle tracks, measures particle momentum and charge, and identifies particle species. It is 4 meters in diameter and 4.2 meters long, providing coverage of $-1.2 < \eta < 1.2$ in pseudo-rapidity with high-quality tracking. With the STAR magnetic field of 0.5 Tesla in the z direction, the TPC can measure particles with momentum larger than 150 MeV/c.

The TPC tracks particles via ionization they cause in the TPC gas volume. As Fig. 2.3 illustrates, the thin conductive Central Membrane, the concentric field cage cylinders and two end caps provide a nearly uniform electric field along the beam pipe z direction in the TPC. As a charged particle traverses in the TPC gas, it ionizes the gas atoms and electrons are released. The ionization electrons drift in the electric field. The drifting electrons avalanche in the high field around the anode in the Multi-Wire Proportional Chambers at the end cap readout. The current collected by wire gives the hit location in the x-y plane and the current amplitude is proportional to the ionization energy loss. Each end cap has 12 sectors with 45 pad rows which gives a maximum of 45 hits per track. At the sector boundaries, the particle reconstruction efficiency is low. Hence, the TPC has detecting deficiency at the sector boundaries. The z position of the charged particle is measured by the product of electron drifting time and drift velocity. The TPC is filled with P10 gas (Ar 90% + CH_4 10%) which provides a stable electron drift velocity that is insensitive to small variations of temperature and pressure. With the hit points x, y and z known, the helix of the particle motion is reconstructed. The particle helix and the STAR magnetic field magnitude together are used to determined the particle momentum and the particle charge sign using the Lorentz force equation of motion. The ionization energy loss dE/dx measured from the readout current is used to identify the particle species.

The particle tracks reconstructed by the TPC hit points are called global tracks. After finishing all track reconstructions in a collision event, the primary vertex of the collision, which is the estimate of the interaction point, is reconstructed from the global tracks. The Distance of Closest Approach (*dca*) is the closest distance from the primary vertex to the track helix. The tracks with *dca* less than 3 cm are refitted with the primary vertex, which are then called primary tracks. The primary track has better momentum resolution than the global track because the primary vertex position from all tracks is more precise than the single track when the track is from the primary vertex. However, when the track is from a secondary vertex, for example from a resonance decay, the primary track becomes less accurate than the global tracks. Hence, the *dca* is used to distinguish whether a track is from the primary vertex or a secondary vertex in the analysis.

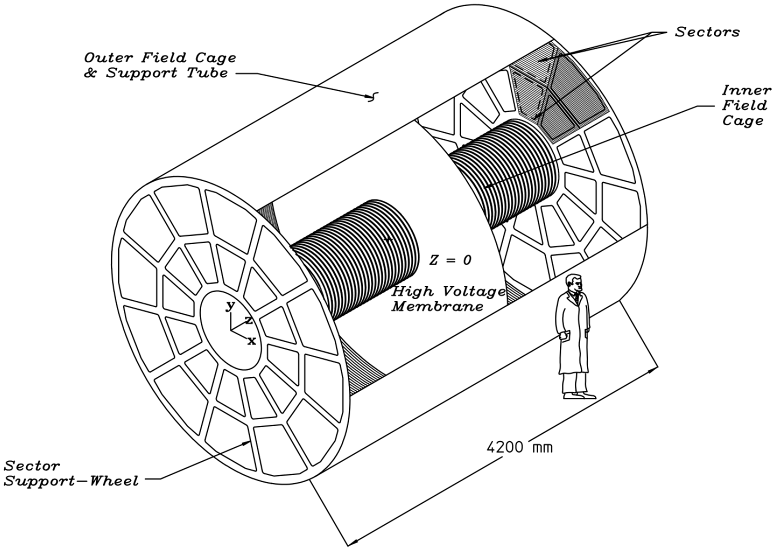

Figure 2.3. The illustration of the Time Projection Chamber at STAR. Figure taken from [68].

2.2.2 Forward Time Projection Chamber

Two cylindrical FTPCs measure charged particles in the range $2.5 < |\eta| < 4$ [69]. The FTPCs extend the STAR rapidity coverage. The major design difference of the FTPC from the TPC is that the electric drift field is in the radial direction instead of parallel to the beam axis. The radial field is used so that the FTPCs have high resolution in regions close to the beam pipe where the density particle tracks is high.

The schematic diagram of an FTPC is shown in Fig. 2.4. In order to fit in the available space inside the TPC (see Fig. 2.2), each FTPC is 75 cm in diameter by 120 cm long. The FTPCs share with the TPC major component the common STAR magnetic field, in the z direction. The radial electric field of the FTPC is provided by the high voltage inner electrode and the grounded outer cylinder wall. The FTPC readout system is located outside the cylinder chamber surface due to its radial drift field. The readout system has 6 sections in the azimuthal ϕ direction and 10 rows in z to afford a maximum of 10 hit points.

Similar to the TPC tracks, the FTPC tracks are reconstructed in two steps (global and then primary tracks) with one additional calibration procedure (misalignment correction). The FTPC global tracks are reconstructed from the FTPC hits. A collision vertex reconstructed from the FTPC global tracks are called FTPC "pre-vertex". The primary vertex reconstructed from the TPC tracks has a better position resolution than the FTPC pre-vertex because TPC has higher resolution than the FTPC. The TPC and FTPC may potentially have a misalignment due to a possible shift (or rotation) of the FTPC mounting points. Therefore, a misalignment correction procedure is conducted based on the discrepancy between the FTPC pre-vertex and the TPC primary vertex. The FTPC primary tracks are reconstructed with the necessary corrections to align the FTPC with the TPC.

To summarize, the FTPC track reconstruction procedure is: reconstruction of FTPC global tracks, determination of FTPC pre-vertex, determination of the correction for misalignment between FTPC and TPC, and finally fitting the corrected FTPC global tracks with TPC vertex to obtain the primary tracks.

2.2.3 Zero Degree Calorimeter

The ZDCs are two hadron calorimeters measuring the neutron energy along the beam pipe after the charged particles are bent out of acceptance of the ZDC by the dipole magnets, as Fig. 2.5 shows [70]. Two ZDCs are located symmetrically at 18 meters away from the collision intersection point on each side, with a horizontal acceptance of ± 5 cm. In relativistic heavy ion collisions, the evaporation neutrons are emitted from spectators, which do not participate in the collision. The ZDC measures the energy of those neutrons. Meanwhile, the east and west ZDC signal timing difference provides a measure of the collision location.

The two main purposes of the ZDCs are event characterization and luminosity monitoring. Together with the Central Trigger Barrel (CTB), the ZDCs characterize the collision centrality. The CTB measures the charged particle multiplicity in $-1 <$

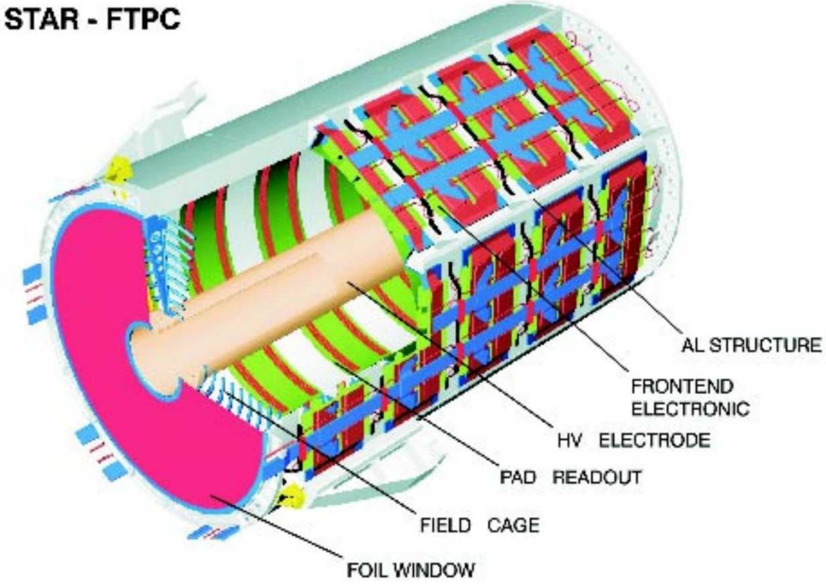

Figure 2.4. The schematic diagram of the FTPC. Figure taken from [69].

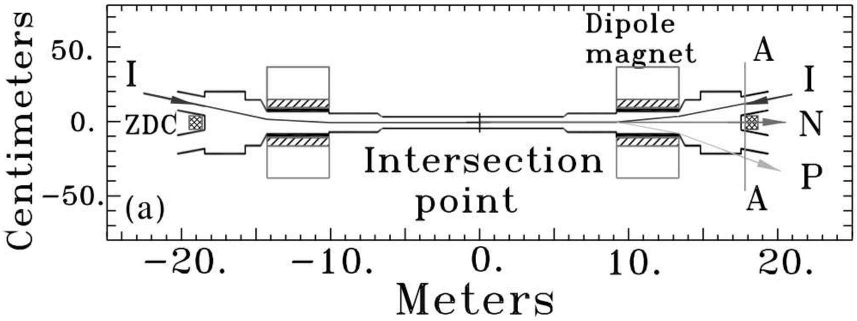

Figure 2.5. The schematic diagram of the ZDC in the context of collisions. Figure taken from [70].

$\eta < 1$ with full ϕ coverage. The CTB is arranged around the TPC and covers similar phase space as the TPC. The CTB records data faster than the TPC detector. The arch shaped color band in Fig. 2.6 (same for left and right panels) is the ZDC measured neutral energy versus the CTB measured charged particle multiplicity distribution for Au+Au collisions. In peripheral Au+Au collisions, the gold ions are largely untouched and bent away by the dipole magnet. There are only a few neutron spectators. Hence, the ZDC signal is small. Meanwhile, the number of the produced charged particles from the collision is also small so that the CTB has a small signal. In semicentral Au+Au collisions, since the gold ion spectators are mostly shattered into nucleons, the maximum number of neutron spectators is reached. The ZDC thus receives its maximum signal. The particle multiplicity at mid-rapidity for the CTB coverage is intermediate between peripheral and central events. A central event has the maximum multiplicity at mid-rapidity compared to more peripheral event, because only a fraction of the nucleons are involved in the collision. The central event gives the maximum CTB signal. However, when all the nucleons participate in the interaction, the number of neutron spectators again becomes small ,resulting in a small ZDC signal. The ZDC and CTB signals together give the collision centrality information in Au+Au collisions.

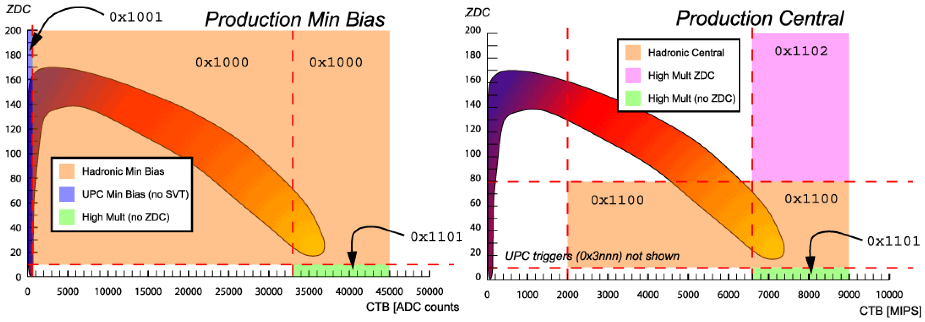

Figure 2.6. An illustration of event characterization by the ZDC-measured neutral energy versus the CTB-measured charged particle multiplicity for minimum bias (left) and central triggered (right) Au+Au collisions. (Plot from STAR trigger website `http://www.star.bnl.gov/public/trg/trouble/operating-trigger/introduction/CtbZdc.gif`)

2.2.4 Minimum Bias Event

The high RHIC crossing rate ($\sim$ 10 MHz) and the low TPC response rate ($\sim$ 100 Hz) call for the need for the trigger system to effectively select interesting events to record. The event characteristics are examined using the fast detectors. When an event passed a given trigger requirement, the trigger system sends a request to start the recording cycle for the slower but more precise detectors,. Both the TPC and the FTPCs are slow detectors because the electrons need time to drift to the readout devices. Both the ZDCs and the CTB are fast detectors, and are used in the trigger system.

Various triggers determine the recording of interesting events and the discarding of the rest. The left and right panels in Fig 2.6, as alreay seen in Section 2.2.3, show an example of two kinds of triggers for Au+Au collisions: minimum bias (left panel) and central (right panel) trigger. The minimum bias (MB) triggered events are in the yellow rectangle area with legend 'Hadronic Min Bias.' While zero bias events are for all possible collisions, MB events are the best event sample estimation for the zero bias events. The typical trigger requirements for a MB event in heavy ion collisions are:

- there are ion bunches in both beam pipes for the possible collisions,
- at least one neutron is detected in each ZDC detector so that there is at least one ion in each beam direction that has interacted,
- the timing difference between two ZDC signals satisfies the correct window to assure the interaction point is inside the TPC, and
- at least 15 particles hit the CTB so that the interaction is an inelastic collision.

The central triggered events are those having a large number of particles hit the CTB after already satisfying the MB trigger requirement. The central triggered events are interesting because they are the most likely to have QGP formed. Other triggers are implemented for various physics purposes as well as new detector monitoring: high

p_T jet events, beam polarization for spin studies, cosmic rays for calibrations, heavy flavor for quarkonium production and so on. For d+Au collisions, the MB event is triggered by the ZDC in the gold-beam going direction only. The STAR trigger system makes sure that, in generally, the detector samples the maximum number of collisions provided by RHIC within the detector response time.

2.2.5 Centrality Definition in Heavy-Ion Collisions

The impact parameter of a collision, which is the distance between the centers of two colliding nuclei, varies from one event to the next. A central collision with a zero impact parameter has a full overlap area, and tends to have the maximum energy density. A peripheral collision of two nuclei with large impact parameter has a small overlap zone, and tends to be similar to a $p+p$ collision. The systems resulted from the various initial heavy-ion collisions geometries are thus different. Experimentally, the collision geometry setup cannot be controlled. On the other hand, in order to compare physical quantities in A+A collisions (nucleus+nucleus) to those in $p+p$ collisions (nucleon+nucleon), one needs to know how many binary nucleon+nucleon collisions (N_{coll}) there are in an A+A collision, as what is done for the nuclear modification factor (in Section 1.5). It is also natural to ask whether an observable is related to N_{coll} or the number of participating nucleons N_{part}. Collisions with different geometries correspond to different N_{coll} and N_{part}.

The Glauber model has been used to describe the collision geometry and to link experimental observables with a theoretical b, N_{coll} and N_{part} [71]. In high energy heavy ion collisions, the de Broglie wavelengths of the nucleons are smaller than their transverse size. Their total geometry cross section is approximately the sum of the individual nucleon+nucleon collision cross sections. The inputs to the Glauber model are the Wood-Saxon nuclear matter density and the inelastic nucleon-nucleon cross section. For a given b, the Glauber Monte Carlo generates the nucleon distribution in the nuclei according to the Wood-Saxon density profile. Further assumptions are made that the nucleons move in straight lines, and each nucleon+nucleon collision happens independently. One nucleon in a nucleus interacts with the nucleons in the other nucleus on their straight line path. The condition for a nucleon+nucleon collision to occur is that their distance apart is within the range of the nucleon+nucleon inelastic cross section. The values of N_{coll} and N_{part} are the output of the Glauber model for a given b. An observable needs to be chosen to map the Glauber model simulation to experimental data for the centrality definition. A basic assumption is that the observable should be a monotonic function of the impact parameter b. As Fig. 2.7 illustrates, the inclusive charged particle multiplicity can be used as a centrality definition observable: the larger the multiplicity, the smaller the b. The dashed lines are an illustration of the typical centrality binning. The illustrations of various collision geometries in the beam view are also depicted for different centrality classes.

While the centrality binning procedure seems straightforward, there are several factors one needs to keep in mind: the centrality observable selection bias, the fluctuations in the experimental observable and in the Glauber model calculated parameters, and the detector acceptance effect. The centrality observable selection bias especially challenges the centrality definition in small systems where the particle multiplicity is low, such as in d+Au collisions (see Chapter 5). For example, events with an energetic jet tends to have a larger multiplicity than the average MB events. Selecting on high multiplicity would therefore bias events towards jet productions and bias jets towards larger energies. However, in heavy ion collisions, the multiplicity is high and the particle production from the hard process is relatively unimportant compared to the total multiplicity. Hence, the multiplicity selection bias is small in heavy ion collisions.

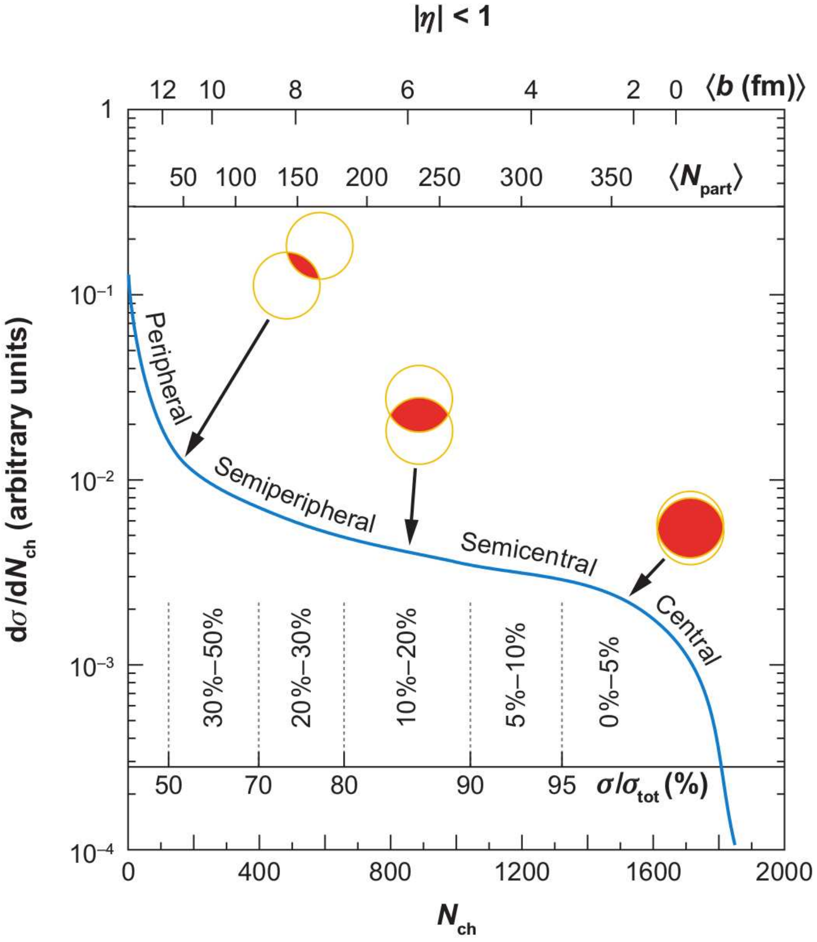

Figure 2.7. An illustration of the correlation of the inclusive charged particle multiplicity and b and N_{part} from Glauber model for centrality definition in Au+Au collisions. Figure taken from [71].

3. Higher Harmonics v_3

This chapter of thesis work has been summarized in [72].

The Fourier coefficients of the particle momentum anisotropy distribution have been considered an important tool to study the QGP bulk properties. In heavy ion physics, the first harmonic v_1, directed flow, and the second harmonic v_2, elliptic flow, have been extensively studied both, experimentally and theoretically. The higher harmonic v_4 has also been studied and is primarily from the non-linear response to the eccentricity ϵ_2 (Eq. (1.1)) of the initial elliptic shape. The odd higher harmonics have traditionally been considered to be zero if the collision energy density distribution is smooth and symmetric. However, a Monte Carlo simulation study [36] reported that event-by-event initial state geometry fluctuations can lead to non-zero higher order odd harmonics. By studying the higher harmonics, one could gain information about the lumpiness in the initial state energy density distribution. The different order of the anisotropy harmonics each responds differently to the hydrodynamic viscosity. The combination of the various harmonic measurements provides better constraints on the hydrodynamic viscosity than the traditional elliptic flow alone. However, the harmonics v_n for $n > 3$ have non-linear responses to the lower harmonics. Hence v_3 is an optimal observable to compare to hydrodynamic calculations.

3.1 Two-Particle Q-Cumulant Method

As discussed in Section 1.3, due to the unknown participant plane, the two-particle correlation method has been used in experiment to measure anisotropic flow. If using Eq. (1.5) directly, the nested loops over the particle pairs will become a CPU consuming process. The mathematical technique of cumulants is thus adopted to simplify the analysis calculation [38].

The cumulant is expressed in terms of moments of the corresponding flow vector Q. For one event with M particles, the nth order harmonic flow vector is

$$Q_n \equiv \sum_{j=1}^{M} \exp(in\phi_j) \text{ with } i = \sqrt{-1}, \tag{3.1}$$

where, ϕ_j is the azimuthal angle of the jth particle. Take the absolute square of the Q_n,

$$Q_n Q_n^* = \sum_{j,k=1}^{M} \exp in(\phi_j - \phi_k) = M + \sum_{j,k=1,j\neq k}^{M} \exp in(\phi_j - \phi_k). \tag{3.2}$$

The second term on the right hand side of Eq. (3.2) is exactly the square of Eq. (1.5), that is, v_n^2. Actually $\sum\limits_{j,k=1,j\neq k} \exp in(\phi_j - \phi_k)$ divided by the number of pairs is called the second order moment,

$$\langle 2_n \rangle = \frac{Q_n Q_n^* - M}{M(M-1)}. \tag{3.3}$$

The single bracket represents the average over particles in one event. The second cumulant is equal to the average of the second moment over events.

$$V_n\{2\} = \langle\langle 2_n \rangle\rangle. \tag{3.4}$$

The double brackets represent the average over particles and events. The cumulant gives the estimation of flow v_n by,

$$v_n\{2\} = \sqrt{V_n\{2\}}. \tag{3.5}$$

For higher order cumulants:

$$v_n\{4\} = \sqrt[4]{V_n\{4\}}; \tag{3.6}$$

$$v_n\{4\} = \sqrt[6]{\frac{1}{4} V_n\{6\}}, \tag{3.7}$$

where

$$V_n\{4\} = 2\langle\langle 2_n\rangle\rangle^2 - \langle\langle 4_n\rangle\rangle; \tag{3.8}$$

$$V_n\{6\} = \langle\langle 6_n\rangle\rangle - 9\langle\langle 2_n\rangle\rangle\langle\langle 4_n\rangle\rangle + 12\langle\langle 2_n\rangle\rangle^3. \tag{3.9}$$

$$\begin{aligned}\langle 4\rangle_n =& \frac{|Q_n|^4 + |Q_{2n}|^2 - 2\cdot Re[Q_{2n}Q_n^*Q_n^*]}{M(M-1)(M-2)(M-3)} \\ &- 2\frac{2(M-2)\cdot|Q_n|^2 - M(M-3)}{M(M-1)(M-2)(M-3)};\end{aligned} \tag{3.10}$$

$$\begin{aligned}\langle 6\rangle_n =& \frac{|Q_n|^6 + 9\cdot|Q_{2n}|^2|Q_n|^2 - 6\cdot Re[Q_{2n}Q_nQ_n^*Q_n^*Q_n^*]}{M(M-1)(M-2)(M-3)(M-4)(M-5)} \\ &+ 4\frac{Re[Q_{3n}Q_n^*Q_n^*Q_n^* - 3\cdot Re[Q_{3n}Q_{2n}^*Q_n^*]}{M(M-1)(M-2)(M-3)(M-4)(M-5)} \\ &+ 2\frac{9(M-4)\cdot Re[Q_{2n}Q_n^*Q_n^*] + 2\cdot|Q_{3n}|^2}{M(M-1)(M-2)(M-3)(M-4)(M-5)} \\ &- 9\frac{|Q_n|^4 + |Q_{2n}|^2}{M(M-1)(M-2)(M-3)(M-5)} \\ &+ 18\frac{|Q_n|^2}{M(M-1)(M-3)(M-4)} \\ &- \frac{6}{(M-1)(M-2)(M-3)}.\end{aligned} \tag{3.11}$$

As the above equations show, the nested loops are now replaced by means of single particle quantities, which need only a single loop over particles to measure. The complex calculation is largely simplified and the computing time is reduced.

Flow is a global property of particle anisotropic distributions in the whole event, respective to a common harmonic plane (the participant plane). Nonflow is intrinsic particle correlations unrelated to the common plane, such as jet correlations, resonance particle decays, and quantum statistics [73–75]. These nonflow correlations contaminate flow measurements.

Nonflow is mostly a short range correlation in $\Delta\phi$ and $\Delta\eta$. In order to eliminate the contribution from nonflow, a $\Delta\eta$-gap method is usually used for the two-particle cumulant measurement. A large $\Delta\eta$ separation eliminates short range correlations, hence, minimizes the nonflow contribution [76]. The $\Delta\eta$-gap two-particle cumulant flow measurement can be illustrated in an example with the STAR TPC which has an acceptance $-1 < \eta < 1$ as the following. The $\Delta\eta$-gap can be chosen as $|\Delta\eta| > 1$. Two

η windows symmetric about mid-rapidity are chosen for the two-particle cumulant measurement such that one particle lies in $-1 < \eta < -0.5$, named group A, and the other particle in $0.5 < \eta < 1$, named group B. The $\Delta\eta$-gap size is determined by two factors. One is the typical angular size of the nonflow contributions, such as the size of the near-side jet cone [77]. The other factor is good statistics for the cumulant results. In symmetric Au+Au collisions, the physics quantities in the two groups A and B should be the identical, since the group A and B are chosen to be symmetric about mid-rapidity. The second order harmonic moment for one particle in A and the other particle in B for integrated p_T (particles in all p_T) is

$$\langle\langle 2_n \rangle\rangle(A;B) = \frac{Q_n(A)Q_n^*(B)}{M(A)M(B)}. \tag{3.12}$$

The two-particle flow estimate in window η_A and/or η_B is

$$v_n(\eta_{A,B}) = \sqrt{\langle\langle 2_n \rangle\rangle(A;B)}. \tag{3.13}$$

Now suppose that group C is the particle of interest (e.g. within a particular p_T bin to study the p_T-dependence of v_n) and group A is the reference particle. A $\Delta\eta$-gap is often also applied between group C and group A. The v_n of the particle of interest (group C) can be calculated with the following equation:

$$v_n(C) = \frac{\langle\langle 2_n \rangle\rangle(C;A)}{\sqrt{\langle\langle 2_n \rangle\rangle(A;B)}}, \tag{3.14}$$

3.2 Data Sample and Analysis Cuts

A total of 19 million minimum bias Au+Au events at $\sqrt{s_{\mathrm{NN}}} = 200$ GeV has been collected by STAR and are used in this thesis. The main detector, the TPC, covers the pseudo-rapidity $-1 < \eta < 1$. The minimum bias collisions are triggered by the ZDC and the Beam-Beam Counter (BBC) detectors [67]. The centrality is measured by the charged particle multiplicity in $-0.5 < \eta < 0.5$ in the TPC. The number of participant nucleons N_{part} and the number of binary nucleon-nucleon collisions N_{coll} for the corresponding Au+Au collisions at $\sqrt{s_{NN}} = 200$ GeV are listed in reference [78].

The collision point is required to be within 30 cm of the TPC center along the beam pipe to assure a uniform acceptance. The charged particle tracks are reconstructed by fitting the hit points in the TPC. The number of hit points is required to be larger than 51% of the number of possible hit points, and also more than 20 hits out of the maximum 45 detecting points. The 51% requirement is to avoid split tracks (single track is fitted as two tracks close together), and the 20 points requirement is to assure there are enough points for a good fit. The *dca* to the primary collision vertex is less than 2 cm.

3.3 v_3 Measurement Result

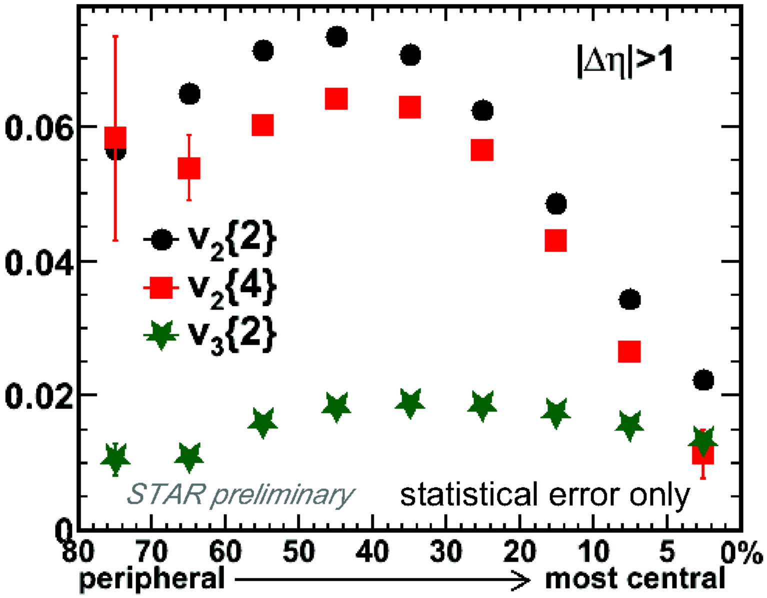

Figure 3.1. Two-particle Q-cumulant flow for the second harmonic $v_2\{2\}$ (black dots) and the triangular $v_3\{2\}$ (green stars), and four-particle Q-cumulant flow for the second harmonic $v_2\{4\}$ (red squares) as a function of centrality in Au+Au at 200 GeV.

Figure 3.1 shows the elliptic flow and third harmonic flow from two- and four-particle Q-cumulant [38] measurements as a function of centrality for Au+Au collisions at 200 GeV. A $\Delta\eta$-gap $|\Delta\eta| > 1$ is applied. The elliptic flow, v_2, reaches its minimum in the most central collisions. In these collisions, the two Au nuclei overlap on top of each other such that the collision region is approximately a round shape. The initial eccentricity ϵ_2 of the collision system is small, which leads to a small elliptic flow for the final particles. As the centrality decreases, the eccentricity and the v_2 increase. The v_2 reaches its maximum in collision of 40-50% centrality class. As for more peripheral collisions, the overlap area decreases, and the energy density becomes small, so less flow is developed.

The four-particle flow is smaller than the two-particle flow, because in the four-particle flow the nonflow contribution, which is a few-body correlation, is suppressed. In addition, the flow fluctuation contribution is negative in the four-particle flow measurement, while it is positive in two-particle flow (see Chapter 4).

The magnitude of the third harmonic flow is less than the elliptic flow v_2. The v_3 dependence on centrality is weak. Since v_3 is due to event-by-event fluctuations, it is not expected to be primarily correlated with the reaction plane, making it unlikely that v_3 will follow the strong centrality dependence as v_2. Discussion on the physics and measurements of event plane (which is the Ψ_n estimate experimentally) correlations can be found in references [79].

Figure. 3.2 compares the two-particle v_3 centrality dependence measurements with three $\Delta\eta$-gaps: $|\Delta\eta| > 1$ for one particle in $-1 < \eta < -0.5$ and the other in $0.5 < \eta < 1$; $|\Delta\eta| > 0.7$ for one in $-1 < \eta < -0.35$ and the other in $0.35 < \eta < 1$; $|\Delta\eta| > 0$ for one in $-1 < \eta < 0$ and the other in $0 < \eta < 1$. $\Delta\eta$-gap size of 1 and 0.7 give similar v_3 for all centralities. In peripheral collisions, $|\Delta\eta| > 0$ is larger than those two with larger $\Delta\eta$-gap. Their difference decreases as the centrality decreases.

Figure. 3.3 shows the measured v_3 as a function of transverse momentum p_T for two centrality classes, 0-5% and 30-40%. For both centrality classes, v_3 increases with p_T and saturates above $2 - 3$ GeV/c. The event-by-event hydrodynamic calculation [80] are superimposed as the dashed curves. The theory calculation is done with the viscosity to entropy density ratio of $\eta/s = 0.08$ and the Glauber initial state condition.

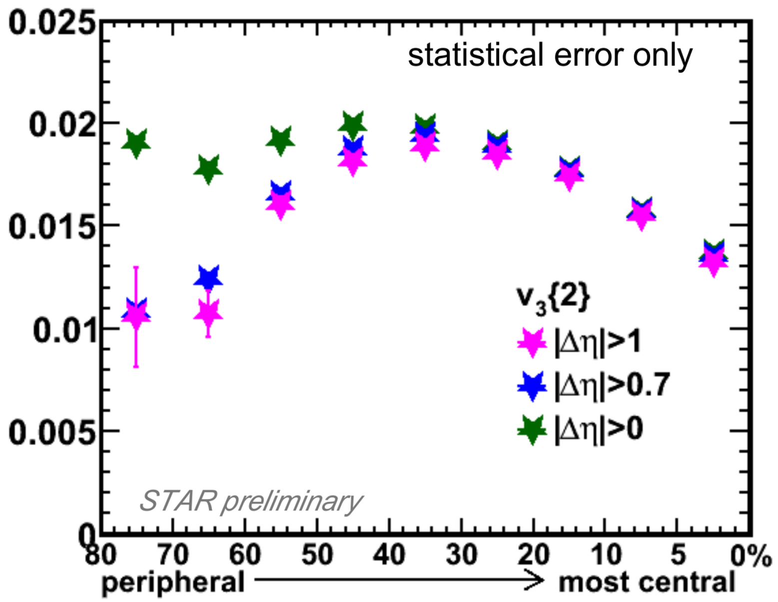

Figure 3.2. Two-particle Q-cumulant flow for the third harmonic $v_3\{2\}$ with $|\Delta\eta|$-gap $|\Delta\eta| > 1$ (pink stars), $|\Delta\eta| > 0.7$ (blue stars) and $|\Delta\eta| > 0$ (green stars) as a function of centrality in Au+Au at 200 GeV.

The hydrodynamic calculation gives a good description for the v_3 trend below 2 GeV/c. Above 2 GeV/c, hydrodynamics may no longer be considered applicable. However, the flow measurement may have nonflow contamination, which needs to be addressed for an precise comparison (see Chapter 4).

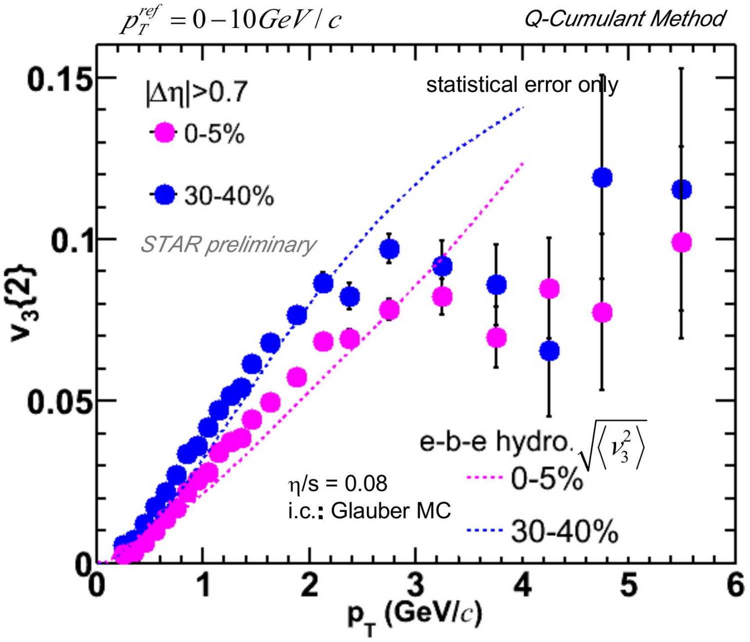

Figure 3.3. Two-particle Q-cumulant flow for the third harmonic $v_3\{2\}$ with $\Delta\eta$-gap $|\Delta\eta| > 0.7$ in 0-5% (pink dots) and 30-40% (blue dots) as a function of transverse momentum p_T in Au+Au at 200 GeV. The dashed curves are the event-by-event hydrodynamic calculation [80].

4. Isolation of Flow and Nonflow Correlations

This chapter of thesis work has been summarized in [81].

Through the comparison of anisotropic flow measurements and hydrodynamic calculations, properties of the early stage of the collision system may be extracted. One of the important variables, the ratio of the shear viscosity to entropy density of the QGP, was found to be not much larger than the conjectured quantum limit of $1/4\pi$ [82].

The momentum-space anisotropic flow can be characterized by the Fourier coefficients v_n as shown in Eq. (1.3). The participant plane Ψ_n is unknown experimentally. The anisotropic flow is thus measured by particle correlations, such as two-particle or multiple-particle correlations [73–75, 83]. (In event plane flow measurement method, the event plane is first determined from all particles. Hence, it is effectively also a two-particle correlation method.) Therefore, the flow measurement is contaminated by intrinsic particle correlations unrelated to the participant plane. Those correlations are generally called nonflow and are due to jet fragmentation, final state Coulomb and strong interactions, resonance decays, etc. [73–75].

The two-particle correlation is given by Eq. (1.4). When nonflow is non-zero, $V_n\{2\} = v_{n,\alpha} \cdot v_{n,\beta} + \delta_n$, where $v_{n,\alpha}, v_{n,\beta}$ stand for the flow of two particles at α and β, and δ_n is the nonflow contribution. Since the shear viscosity extracted from the flow measurement is sensitive to even a small uncertainty [84], it is important to eliminate nonflow contributions in flow measurements.

This chapter describes a method to separate flow and nonflow in a data-driven way, with minimal reliance on models. Two- and four-particle cumulants with different pseudo-rapidity (η) combinations are measured. By exploiting the symmetry of the average flow $\langle v \rangle$ in η about mid-rapidity in symmetric Au+Au collisions, $\Delta\eta$-independent and $\Delta\eta$-dependent contributions are separated. Flow, as an event-wise many-particle azimuthal correlation, reflecting properties on the single-particle level, is dependent on η. However, nonflow is a few-particle azimuthal correlation that depends on the $\Delta\eta$ distance between the particles. Hence, the $\Delta\eta$-independent part is associated with flow, while the $\Delta\eta$-dependent part is associated with nonflow.

4.1 Analysis Method

In this analysis, the anisotropy was calculated with the two- and four-particle Q-cumulant method using unit weight for event average [38]. The non-uniform acceptance is corrected (see Section 4.2.2). By using the moment of the flow vector, this method calculates multi-particle cumulant from the mean moment values without going over pair or high multiplet loops.

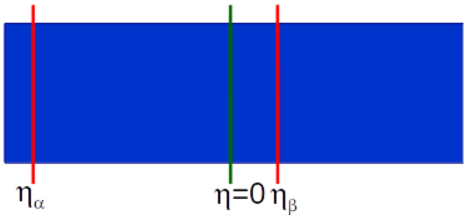

Figure 4.1. Illustration of one pair of two-particle cumulant $V(\eta_\alpha, \eta_\beta)$ with one particle at η_α and the other particle at η_β.

The two-particle cumulant, with one particle at pseudo-rapidity η_α and another at η_β, illustrated in Figure 4.1, is [85, 86]

$$\begin{aligned} V\{2\} &\equiv \langle\langle e^{i(\phi_\alpha-\phi_\beta)}\rangle\rangle = \langle v(\eta_\alpha)v(\eta_\beta)\rangle + \delta(\Delta\eta) \\ &\equiv \langle v(\eta_\alpha)\rangle\langle v(\eta_\beta)\rangle + \sigma(\eta_\alpha)\sigma(\eta_\beta) + \sigma'(\Delta\eta) + \delta(\Delta\eta), \end{aligned} \tag{4.1}$$

where $\Delta\eta = |\eta_\beta - \eta_\alpha|$. The single brackets represent the average over events only, while the double brackets are for the average over particle pairs and the average over events. For example, the harmonic number n is suppressed to lighten the notation. The average flow $\langle v \rangle$ is the anisotropy parameter with respect to the participant plane. σ is the flow fluctuation of $\langle v \rangle$. Because average flow reflects the property on the single-particle level, $\langle v \rangle$ and σ are only functions of η, and are $\Delta\eta$-independent. However, a $\Delta\eta$-dependent flow fluctuation component could exist. The harmonic planes Ψ_n could depend on η due to the initial energy density longitudinal fluctuation [87–89]. The σ' is used to denote such $\Delta\eta$-dependent part of the flow fluctuation. The δ is nonflow, which is generally a function of $\Delta\eta$, but may also depend on η.

For the four-particle cumulant, two particles are at η_α and another two are at η_β. For easier discussion, the square root of the four-particle cumulant is used, which has the same order in $\langle v \rangle$ as the two-particle cumulant. The square root of the four-particle cumulant is given by

$$\begin{aligned} V^{\frac{1}{2}}\{4\} &\equiv \sqrt{\langle\langle e^{i(\phi_\alpha+\phi_\alpha-\phi_\beta-\phi_\beta)}\rangle\rangle} \\ &\approx \langle v(\eta_\alpha)\rangle\langle v(\eta_\beta)\rangle - \sigma(\eta_\alpha)\sigma(\eta_\beta) - \sigma'(\Delta\eta), \end{aligned} \tag{4.2}$$

where the approximation assumes that the flow fluctuation is relatively small compared with the average flow [90]. In $V^{1/2}\{4\}$, the contribution from the two-particle correlations due to nonflow effects is suppressed, while the contribution from the four-particle correlations due to nonflow effects $\propto 1/M^3$ (M is multiplicity) and is, therefore, negligible [91, 92]. The flow fluctuation has negative contribution in $V^{1/2}\{4\}$, while it is positive in $V\{2\}$.

The analysis method described in Ref. [86] is used to extract the values of the average flow, $\langle v \rangle$, the $\Delta\eta$-dependent and $\Delta\eta$-independent flow fluctuations, σ' and σ, and the nonflow contribution, δ. Consider two pairs of two-particle cumulants as Fig. 4.2 left panel illustrates. The difference between cumulants $V\{2\}$ at $(\eta_\alpha, \eta_\beta)$ and $(\eta_\alpha, -\eta_\beta)$ is

$$\begin{aligned} \Delta V\{2\} &\equiv V\{2\}(\eta_\alpha, \eta_\beta) - V\{2\}(\eta_\alpha, -\eta_\beta) \\ &\equiv V\{2\}(\Delta\eta_1) - V\{2\}(\Delta\eta_2) \\ &= \Delta\sigma' + \Delta\delta, \end{aligned} \tag{4.3}$$

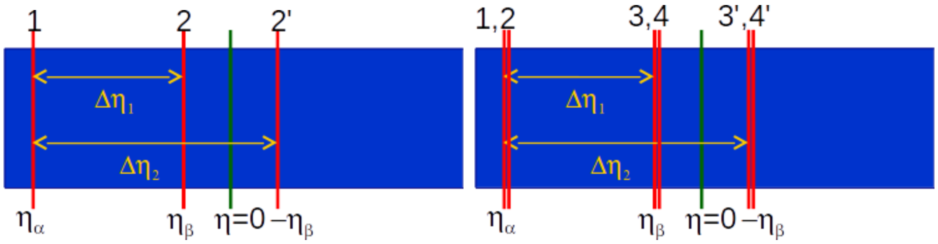

Figure 4.2. Left: Two pair of two-particle cumulants, $V\{2\}(\eta_\alpha, \eta_\beta)$ with one particle at η_α and the other particle at η_β, and $V\{2\}(\eta_\alpha, -\eta_\beta)$ with one particle at η_α and the other particle at $-\eta_\beta$. One pair is denoted as particle 1 and 2. The other pair is particle 1 and 2'. Right: Two pair of four-particle cumulants, $V\{4\}(\eta_\alpha, \eta_\beta)$ with two particles at η_α and the other two particles at η_β, and $V\{4\}(\eta_\alpha, \eta_\beta)$ with two particles at η_α and the other two particles at $-\eta_\beta$. One quadruplet is denoted as particles 1, 2, 3 and 4. The other quadruplet is 1, 2, 3' and 4'.

where $\eta_\alpha < \eta_\beta < 0$ or $0 < \eta_\beta < \eta_\alpha$ is required. Similarly, for two pairs of four-particle cumulants as illustrated in Fig. 4.2 right panel, the difference for $V^{1/2}\{4\}$ yields,

$$\begin{aligned}\Delta V^{\frac{1}{2}}\{4\} &\equiv V^{\frac{1}{2}}\{4\}(\eta_\alpha,\eta_\beta) - V^{\frac{1}{2}}\{4\}(\eta_\alpha,-\eta_\beta)\\ &\equiv V^{\frac{1}{2}}\{4\}(\Delta\eta_1) - V^{\frac{1}{2}}\{4\}(\Delta\eta_2)\\ &\approx -\Delta\sigma'. \end{aligned} \tag{4.4}$$

Here $\Delta\eta_1 \equiv \eta_\beta - \eta_\alpha,\ \Delta\eta_2 \equiv -\eta_\beta - \eta_\alpha,\ \Delta\sigma' = \sigma'(\Delta\eta_1) - \sigma'(\Delta\eta_2)$, and $\Delta\delta = \delta(\Delta\eta_1) - \delta(\Delta\eta_2)$. In symmetric Au+Au collisions, the two $\Delta\eta$-independent terms in Eqs. (4.1) and (4.2) have $\langle v(\eta_\alpha)\rangle\langle v(\eta_\beta)\rangle = \langle v(\eta_\alpha)\rangle\langle v(-\eta_\beta)\rangle$ and $\sigma(\eta_\alpha)\sigma(\eta_\beta) = \sigma(\eta_\alpha)\sigma(-\eta_\beta)$. The differences from these $\Delta\eta$-independent terms have zero contribution in Eqs. (4.3) and (4.4). Therefore the differences in Eqs. (4.3) and (4.4) depend only on the $\Delta\eta$-dependent terms: flow fluctuation $\Delta\sigma'$ and nonflow $\Delta\delta$.

The goal is to parameterize the flow fluctuation $\Delta\sigma'$ and nonflow $\Delta\delta$. The plan is as follows: extract the empirical functional form for

$$D(\Delta\eta) = \sigma'(\Delta\eta) + \delta(\Delta\eta), \tag{4.5}$$

from $\Delta V_2\{2\}$ data; obtain the σ' result from $\Delta V_2^{1/2}\{4\}$; use D and σ' to determine δ; finally $\langle v\rangle$ and σ.

4.2 Data Analysis

4.2.1 Data Samples and Analysis Cuts

This thesis work principally relies on measurements by the STAR TPC [93]. A total of 25 million Au+Au collisions at $\sqrt{s_{\rm NN}} = 200$ GeV, collected with a minimum bias trigger in 2004, were used. The events selected were required to have a primary event vertex within $|z_{vtx}| < 30$ cm along the beam axis to ensure nearly uniform detector acceptance. The centrality definition was based on the raw charged particle multiplicity within $|\eta| < 0.5$ in TPC. The charged particle tracks used in the analysis were required to satisfy the following conditions: the transverse momentum $0.15 <$

$p_T < 2$ GeV/c to minimize jet contributions; the distance of closest approach to the event vertex $|dca| < 3$ cm to ensure that the particles are from the primary collision vertex instead of a secondary particle decay vertex; the number of fit points along the track greater than 20, and the ratio of the number of fit points along the track to the maximum number of possible fit points larger than 0.51 for good primary track reconstruction and to avoid split tracks [94]. For the particles used in this thesis work, the pseudo-rapidity region was restricted to $|\eta| < 1$.

4.2.2 Non-Uniform Acceptance Correction

For a detector with uniform acceptance, the terms such as $\langle\langle\cos\phi_\alpha\rangle\rangle$ and $\langle\langle\sin\phi_\alpha\rangle\rangle$ vanish. Although STAR TPC has a nearly uniform acceptance, there could still be some deficiencies. The non-uniform acceptance can be corrected by [38]

$$V\{2\} = \langle\langle 2\rangle\rangle - [\langle\langle\cos\phi_\alpha\rangle\rangle \cdot \langle\langle\cos n\phi_\beta\rangle\rangle + \langle\langle\sin\phi_\alpha\rangle\rangle \cdot \langle\langle\sin\phi_\beta\rangle\rangle]; \tag{4.6}$$

$$
\begin{aligned}
V\{4\} = {} & \langle\langle 4\rangle\rangle - 2\langle\langle 2\rangle\rangle^2 \\
& - 6\langle\langle\cos\phi_\alpha\rangle\rangle^3\langle\langle\cos\phi_\beta\rangle\rangle + 2\langle\langle\cos\phi_\alpha\rangle\rangle^2\langle\langle\cos(\phi_\beta+\phi_\alpha)\rangle\rangle \\
& -2\langle\langle\cos\phi_\alpha\rangle\rangle\langle\langle\cos(\phi_\beta+\phi_\alpha-\phi_\alpha)\rangle\rangle+4\langle\langle\cos\phi_\alpha\rangle\rangle^2\langle\langle\cos(\phi_\beta-\phi_\alpha)\rangle\rangle-\langle\langle\cos\phi_\alpha\rangle\rangle\langle\langle\cos(\phi_\beta-\phi_\alpha-\phi_\alpha)\rangle\rangle \\
& + 4\langle\langle\cos\phi_\alpha\rangle\rangle\langle\langle\cos\phi_\beta\rangle\rangle\langle\langle\cos(\phi_\alpha-\phi_\alpha)\rangle\rangle - \langle\langle\cos\phi_\beta\rangle\rangle\langle\langle\cos(\phi_\alpha-\phi_\alpha-\phi_\alpha)\rangle\rangle \\
& + 2\langle\langle\cos\phi_\alpha\rangle\rangle\langle\langle\cos\phi_\beta\rangle\rangle\langle\langle\cos n(-\phi_\alpha-\phi_\alpha)\rangle\rangle - \langle\langle\cos(\phi_\beta+\phi_\alpha)\rangle\rangle\langle\langle\cos(-\phi_\alpha-\phi_\alpha)\rangle\rangle \\
& - 6\langle\langle\cos\phi_\alpha\rangle\rangle\langle\langle\cos\phi_\beta\rangle\rangle\langle\langle\sin\phi_\alpha\rangle\rangle^2 - 2\langle\langle\cos(\phi_\beta+\phi_\alpha)\rangle\rangle\langle\langle\sin\phi_\alpha\rangle\rangle^2 \\
& + 4\langle\langle\cos(\phi_\beta-\phi_\alpha)\rangle\rangle\langle\langle\sin\phi_\alpha\rangle\rangle^2 - 6\langle\langle\cos\phi_\alpha\rangle\rangle^2\langle\langle\sin\phi_\alpha\rangle\rangle\langle\langle\sin\phi_\beta\rangle\rangle \\
& + 4\langle\langle\cos(\phi_\alpha-\phi_\alpha)\rangle\rangle\langle\langle\sin\phi_\alpha\rangle\rangle\langle\langle\sin\phi_\beta\rangle\rangle - 2\langle\langle\cos n(-\phi_\alpha-\phi_\alpha)\rangle\rangle\langle\langle\sin\phi_\alpha\rangle\rangle\langle\langle\sin\phi_\beta\rangle\rangle \\
& - 6\langle\langle\sin\phi_\alpha\rangle\rangle^3\langle\langle\sin\phi_\beta\rangle\rangle + 4\langle\langle\cos\phi_\alpha\rangle\rangle\langle\langle\sin\phi_\alpha\rangle\rangle\langle\langle\sin(\phi_\beta+\phi_\alpha)\rangle\rangle \\
& - 2\langle\langle\sin\phi_\alpha\rangle\rangle\langle\langle\sin(\phi_\beta+\phi_\alpha-\phi_\alpha)\rangle\rangle + \langle\langle\sin\phi_\alpha\rangle\rangle\langle\langle\cos(\phi_\beta-\phi_\alpha-\phi_\alpha)\rangle\rangle \\
& + \langle\langle\sin\phi_\beta\rangle\rangle\langle\langle\sin(\phi_\alpha-\phi_\alpha-\phi_\alpha)\rangle\rangle - 2\langle\langle\cos\phi_\beta\rangle\rangle\langle\langle\sin\phi_\alpha\rangle\rangle\langle\langle\sin(-\phi_\alpha-\phi_\alpha)\rangle\rangle \\
& - 2\langle\langle\cos\phi_\alpha\rangle\rangle\langle\langle\sin\phi_\beta\rangle\rangle\langle\langle\sin(-\phi_\alpha-\phi_\alpha)\rangle\rangle + \langle\langle\sin(\phi_\beta+\phi_\alpha)\rangle\rangle\langle\langle\sin(-\phi_\alpha-\phi_\alpha)\rangle\rangle.
\end{aligned}
\tag{4.7}
$$

The non-uniform acceptance correction for 20-30% centrality was 0.7% for the second harmonic two-particle cumulant $V_2\{2\}$, and 0.5% for the square root of the second harmonic four-particle cumulant $V_2^{1/2}\{4\}$. The largest acceptance correction was 1.8% for $V_2\{2\}$ in the most central collisions, and 1% for $V_2^{1/2}\{4\}$ in the most peripheral collisions.

4.2.3 Track Merging Effect

When two track trajectories in the TPC are too close to each other, the reconstruction algorithm has difficulty to identify them as two tracks but instead only one track. The deficiency of reconstruction of two close tracks is called the track merging effect. While track merging effect on two particles' azimuthal angle $\Delta\phi$ depends on the combination of two particles' charges and the magnetic field polarity, the effect on pseudo-rapidity $\Delta\eta$ is independent of charges and magnet field. As Fig. 4.3 shows, for particles with $0.15 < p_T < 2$ GeV/c in Au+Au collisions at $\sqrt{s_{\rm NN}} = 200$

GeV, the track merging effect is limited to two particles with $|\Delta\eta| < 0.05$. Since the track merging affects only the region $|\Delta\eta| < 0.05$, the $V_n\{2\}$ and $V_n\{4\}$ points in the affected region were excluded from further analysis.

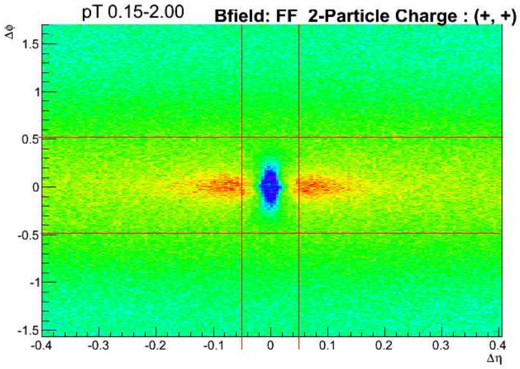

Figure 4.3. The $\Delta\eta - \Delta\phi$ two-particle correlation demonstrating deficit due to track merging effect in Au+Au collisions at $\sqrt{s_{\mathrm{NN}}} = 200$ GeV for particles in $0.15 < p_T < 2$ GeV/c. The x axis is the pseudo-rapidity separation between two particles $\Delta\eta$ and the y axis is their azimuthal angle difference $\Delta\phi$. The shown case is for two positive particles and positive full magnetic field polarity (positive z direction). The red color represents large number of pairs. The blue color represents small number of pairs.

4.2.4 Two- and Four-particle Cumulant Measurements

The two- and four-particle cumulants were measured for various $(\eta_\alpha, \eta_\beta)$ pairs and quadruplets. Figure 4.4 shows the results for 20-30% central Au+Au collisions. Panels (a) and (b) are the two-particle second and third harmonic cumulants, $V_2\{2\}(\eta_\alpha, \eta_\beta)$ and $V_3\{2\}(\eta_\alpha, \eta_\beta)$, respectively. Panel (c) is the square root of the four-particle second harmonic cumulant, $V_2^{1/2}\{4\}(\eta_\alpha, \eta_\alpha, \eta_\beta, \eta_\beta)$. From the points on the diagonal to the points off the diagonal, the gap between the η_α and η_β, which is $|\Delta\eta| = |\eta_\alpha - \eta_\beta|$, increases. Figure 4.4 shows $V_2\{2\}$ decreases as $|\Delta\eta|$ increases. The points on the diagonal are affected by track merging effect (see Section 4.2.3) and thus they are excluded from further analysis. $V_3\{2\}$ suggests the same trend. However, $V_3\{2\}$ magnitude is smaller, and decreases more rapidly with $\Delta\eta$ than $V_2\{2\}$ does. $V_2^{1/2}\{4\}$ is roughly constant and the magnitude is smaller than that of $V_2\{2\}$ which is consistent with the expectation that $V_2^{1/2}\{4\}$ is less affected by the nonflow and the flow fluctuation is negative in $V_2^{1/2}\{4\}$.

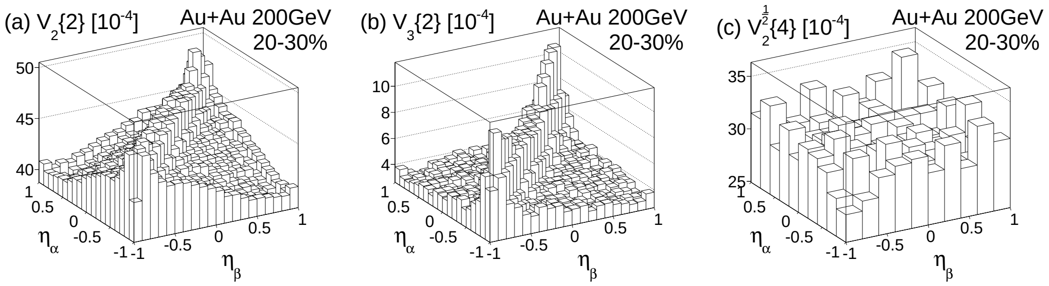

Figure 4.4. The second (a) and third (b) harmonic two-particle cumulants for $(\eta_\alpha, \eta_\beta)$ pairs and the second harmonic four-particle cumulant for $(\eta_\alpha, \eta_\alpha, \eta_\beta, \eta_\beta)$ quadruplets for 20-30% central Au+Au collisions at $\sqrt{s_{\rm NN}} = 200$ GeV.

4.2.5 Nonflow Parameterization

Fig. 4.5(a) shows the measured two-particle second harmonic cumulant difference $\Delta V_2\{2\}$. For each $\Delta\eta_1$ (the points with same color), the data value appear to be linear in $\Delta\eta_2 - \Delta\eta_1$ except near $\Delta\eta_1 = \Delta\eta_2$ as shown by dashed lines in Fig. 4.5 (a) and (b). Moreover, the magnitude of $\Delta V_2\{2\}$ decreases with increasing $\Delta\eta_1$. Linear fits of the dashed lines indicate that the intercept decreases exponentially with increasing $\Delta\eta_1$, and the slopes are all similar. Such behavior can be described mathematically as $a\exp(-\frac{\Delta\eta_1}{b})+k(\Delta\eta_2-\Delta\eta_1)$. In order to express the measured two-particle cumulant difference in the form of $D(\Delta\eta_1) - D(\Delta\eta_2) = (\sigma'(\Delta\eta_1)+\delta(\Delta\eta_1))-(\sigma'(\Delta\eta_2)+\delta(\Delta\eta_2))$ $=(\sigma'(\Delta\eta_1)-\sigma'(\Delta\eta_2))+(\delta(\Delta\eta_1)-\delta(\Delta\eta_2))$, two improvements are made to the initial guess of the exponential+linear form of function $D(\Delta\eta)$. First, a term $a\exp(-\frac{\Delta\eta_2}{b})$ is added which is small for data with $\Delta\eta_2$ significantly larger than $\Delta\eta_1$. Second, because

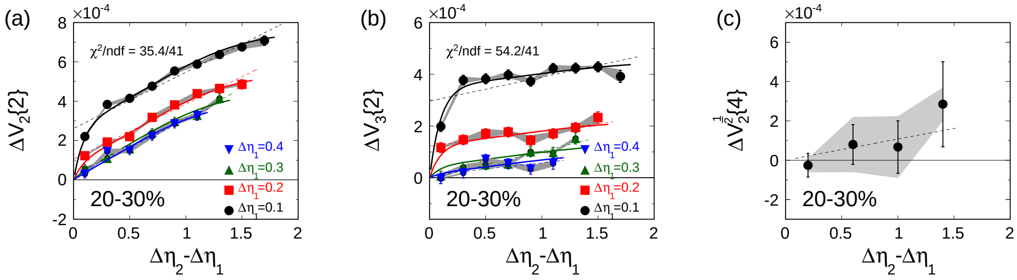

Figure 4.5. The (a) $V_2\{2\}$ and (b) $V_3\{2\}$ difference between the pairs at $(\eta_\alpha, \eta_\beta)$ and $(\eta_\alpha, -\eta_\beta)$. The dashed lines are linear fits for each data set of $\Delta\eta_1$ value separately. The solid curves are a single fit of Eq. (4.8) to all data points with different $\Delta\eta_1$. (c) The $V_2^{1/2}\{4\}$ difference between quadruplets at $(\eta_\alpha, \eta_\alpha, \eta_\beta, \eta_\beta)$ and $(\eta_\alpha, \eta_\alpha, -\eta_\beta, -\eta_\beta)$. The dashed line is a linear fit to the data points. The gray band is the systematic error. The data are from 20-30% central Au+Au collisions at $\sqrt{s_{\rm NN}} = 200$ GeV.

the linear term is unbounded in $\Delta\eta_1$ and $\Delta\eta_2$, it is replaced with the subtraction of two wide Gaussian terms. The Gaussian functions tend to zero as the exponents become large, consistent with the behavior of nonflow. The measured two-particle cumulant difference can then be described by Eq. (4.9):

$$D(\Delta\eta) = a\exp\left(-\frac{\Delta\eta}{b}\right) + A\exp\left(-\frac{\Delta\eta^2}{2\sigma^2}\right), \tag{4.8}$$

such that

$$\begin{aligned}\Delta V\{2\} &= D(\Delta\eta_1) - D(\Delta\eta_2) \\ &= \left[a\exp\left(\frac{-\Delta\eta_1}{b}\right) + A\exp\left(\frac{-\Delta\eta_1^2}{2\sigma^2}\right)\right] \\ &- \left[a\exp\left(\frac{-\Delta\eta_2}{b}\right) + A\exp\left(\frac{-\Delta\eta_2^2}{2\sigma^2}\right)\right],\end{aligned} \tag{4.9}$$

follows from Eq. (4.3). Function $D(\Delta\eta)$ has four parameters a, A, b, and σ. These parameters were determined by fitting Eq. (4.9) simultaneously to all measured two-particle cumulant difference data points with different $\Delta\eta_1$. The fit results are shown in Fig. 4.5(a) as the solid curves with $\chi^2/\mathrm{ndf} \approx 1$. The parameterization is valid within the fitting errors. The same procedure was repeated for the third harmonic $V_3\{2\}$ as shown in Fig. 4.5(b). The fit results give the $\Delta\eta$-dependent part of the two-particle cumulant as Eq. (4.8). Thus, the form of the function D is data-driven.

A similar procedure is followed on the measured difference of the square root of the four-particle cumulant, Eq. (4.2). $\Delta V_2^{1/2}\{4\} = \sigma'(\Delta\eta_1) - \sigma'(\Delta\eta_2)$ is fit by a linear function $k'(\Delta\eta_2 - \Delta\eta_1)$, as the dashed line shows in Fig. 4.5(c). The slope k' from the fit is $(1.1 \pm 0.8) \times 10^{-4}$. In Fig. 4.5(c), each data point is the average of $\Delta V_2^{1/2}\{4\}$ for all $\Delta\eta_1$ at same $\Delta\eta_2 - \Delta\eta_1$ value. With the $\sigma'(\Delta\eta)$ result from the $\Delta V_2^{1/2}\{4\}$ parameterization, the contribution from nonflow, δ, can then be determined through Eq. (4.5).

Subtracting the parameterized D of Eq. (4.8) from the measured two-particle cumulants, $V\{2\}$, yields, from Eq. (4.1), the $\Delta\eta$-independent terms $\langle v^2\rangle \equiv \langle v\rangle^2 + \sigma^2$. Together with $V^{1/2}\{4\}$ from Eq. (4.2), the values of $\langle v\rangle$ and σ may be individually determined.

4.3 Results and Discussion

Figure 4.6 (a) and (b) show the decomposed flow with $\Delta\eta$-independent flow fluctuations $\langle v(\eta_\alpha)v(\eta_\beta)\rangle$ (see Eq. (4.1)) for v_2 and v_3, respectively. The results are found to be constant over η in the measured pseudo-rapidity range $|\eta| < 1$. Therefore, the observed decrease of $V\{2\}$ in Fig. 4.4 with increasing $\Delta\eta$ off diagonal is due to contributions from nonflow and $\Delta\eta$-dependent fluctuations. Note that there is no assumption about the η dependence of flow in the analysis; the flow can be $\Delta\eta$-independent but η-dependent. The observation that the decomposed flow and flow fluctuations are independent of η is, therefore, significant.

Figure 4.6 (c) and (d) show the projections of $\langle v(\eta_\alpha)v(\eta_\beta))\rangle$ in Fig. 4.6 (a) and (b) onto one η variable. The shaded band shows the systematic uncertainty, dominated by the systematic errors in the subtracted $D(\Delta\eta)$ term. For comparison, the projection of the $V_2\{2\}$ is also shown, where the shaded band is the systematic uncertainty. The

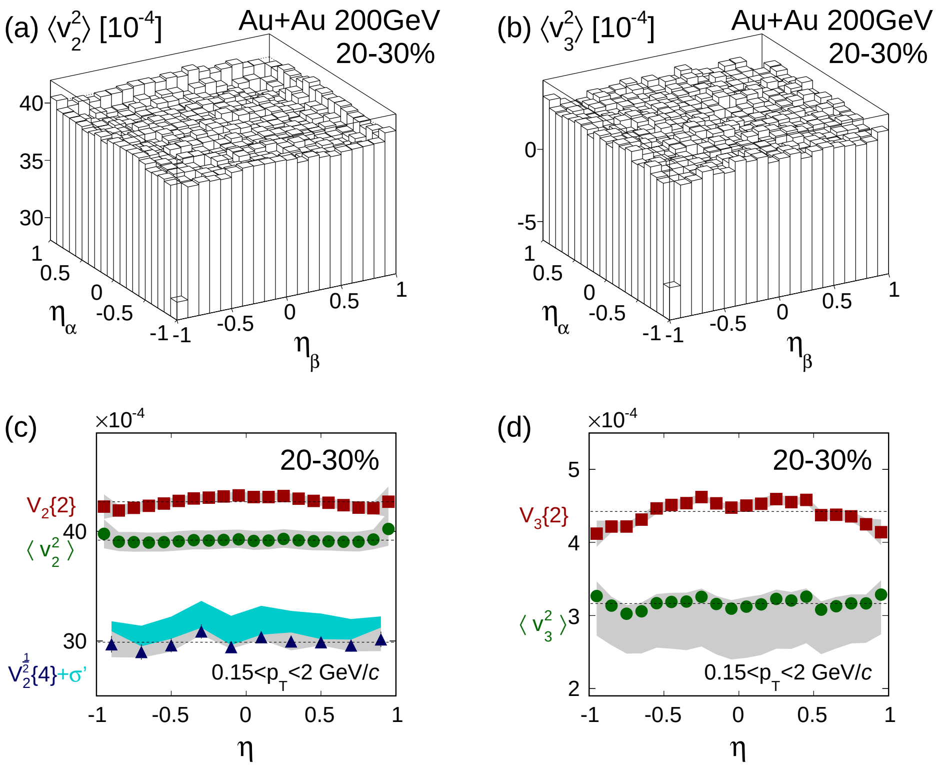

Figure 4.6. The decomposed $\langle v^2\rangle = \langle v\rangle^2 + \sigma^2$ for the second (a) and third (b) harmonics for $(\eta_\alpha, \eta_\beta)$ pairs. (c): The two- and four-particle cumulants, $V_2\{2\}$ (solid red squares) and $V_2^{1/2}\{4\}$ (solid blue triangles), and the decomposed $\langle v_2^2\rangle$ (solid green dots) as a function of η for one particle while averaged over η of the partner particle. The cyan band on top of $V_2^{1/2}\{4\}$ points present $V_2^{1/2}\{4\} + \sigma'$. (d): $V_3\{2\}$ (solid red squares) and $\langle v_3^2\rangle$ (solid green dots) as a function of η. The dashed lines are the mean values averaged over η for 20-30% central Au+Au collisions at $\sqrt{s_{\rm NN}} = 200$ GeV.

projections are the respective quantities as a function of η of one particle averaged over all η of the other particle with unity weight. The flows with $\Delta\eta$-independent fluctuation averaged over η are $\sqrt{\langle v_2^2\rangle} = 6.27\% \pm 0.003\%(stat.)^{+0.08}_{-0.07}\%(sys.)$ and $\sqrt{\langle v_3^2\rangle} = 1.78\% \pm 0.008\%(stat.)^{+0.09}_{-0.16}\%(sys.)$ for the p_T range $0.15 < p_T < 2$ GeV/c in the 20-30% centrality Au+Au collisions. The quoted statistical errors are from the $V\{2\}$ measurements, while the systematic errors are dominated by the parameteriza-

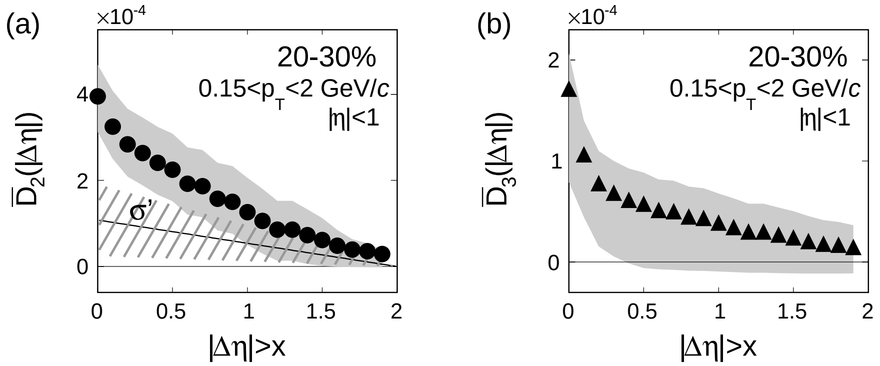

Figure 4.7. The $\Delta\eta$-dependent component of the two-particle cumulant with $\Delta\eta$-gap, $\bar{D}$ in Eq. (4.11), of the second (a) and third (b) harmonics is shown as a function of $\Delta\eta$-gap $|\Delta\eta| > x$. (x is the x-axis value.) The shaded bands are systematic uncertainties. In (a) the estimated σ' is indicated as the straight line, with its uncertainty of ±1 standard deviation as the cross-hatched area for 20-30% central Au+Au collisions at $\sqrt{s_{\mathrm{NN}}} =$ 200 GeV.

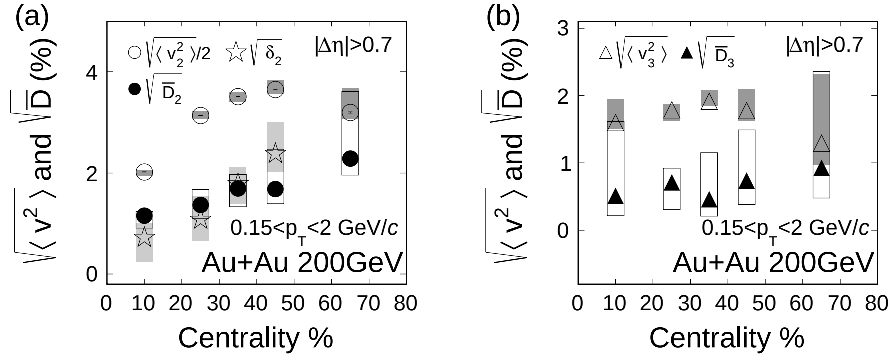

Figure 4.8. The nonflow, $\sqrt{\bar{D}_2}$ (solid dots), $\sqrt{\delta_2}$ (open stars), $\sqrt{\bar{D}_3}$ (solid triangles) and flow, $\sqrt{\langle v_2^2\rangle}/2$ (open circles), $\sqrt{\langle v_3^2\rangle}$ (open triangles) results are shown as a function of centrality percentile for the second (a) and third (b) harmonics, respectively. The statistical errors are smaller than the symbol sizes. The systematic errors are denoted by the vertical rectangles.

tion of D. The difference between $V\{2\}$ and $\langle v^2\rangle$ in Fig. 4.6(c) represents the $D(\eta)$ value versus η of one particle averaged over all η of the other particle.

Figure 4.6(c) also shows the $V_2^{1/2}\{4\}$ projection as a function of η as the solid blue triangles. $V_2^{1/2}\{4\}$ is independent of η. The cyan band is $V_2^{1/2}\{4\} + \sigma' = \langle v\rangle^2 - \sigma^2$, with the systematic uncertainty dominated by the fitting uncertainty in σ'. The difference between the decomposed $\langle v^2\rangle = \langle v\rangle^2 + \sigma^2$ and $V_2^{1/2}\{4\} + \sigma' = \langle v\rangle^2 - \sigma^2$ is two times the $\Delta\eta$-independent flow fluctuation, which is also constant over η within the measured acceptance. The relative $\Delta\eta$-independent elliptic flow fluctuation is calculated as

$$\begin{aligned}\frac{\sigma_2}{\langle v_2\rangle} &= \sqrt{\frac{\langle v_2^2\rangle - (V_2^{\frac{1}{2}}\{4\} + \sigma')}{\langle v_2^2\rangle + (V_2^{\frac{1}{2}}\{4\} + \sigma')}} \\ &= 34\% \pm 2\%(stat.) \pm 3\%(sys.), \qquad (4.10)\end{aligned}$$

where the systematic error is dominated by those in the parameterization of σ'. The relative fluctuation result is consistent with that from the PHOBOS experiment [95] and the previous STAR upper limit measurement [78].

A $\Delta\eta$-gap is usually applied to reduce nonflow contamination in flow measurements (Chapter 3). The nonflow $\bar{D}(|\Delta\eta|)$ contribution in the $\Delta\eta$-gap measurement is calculated as:

$$\bar{D}(|\Delta\eta|) = \frac{\int_{|\Delta\eta|}^{2} \mathrm{d}\Delta\eta' D(\Delta\eta')}{2 - |\Delta\eta|}. \qquad (4.11)$$

$|\Delta\eta| = 2$ is the acceptance limit of the TPC. $\bar{D}$ is the average of D with $|\Delta\eta|$ larger than a certain value. Figure 4.7 (a) and (b) shows $\bar{D}(|\Delta\eta|)$ as a function of $\Delta\eta$-gap $|\Delta\eta| > x$ (x is the x-axis value) for the second and third harmonics, respectively. The bands are the systematic errors estimated from the fitting errors and the different fitting functions as described previously. These errors are correlated because all the errors are from the same fit parameters of the function D.

As noted above, $\bar{D}(|\Delta\eta|)$ is comprised of two parts: the contribution from the $\Delta\eta$-dependent flow fluctuation σ', and the term representing the nonflow δ. In Fig. 4.7(a), these two contributors are estimated separately. The straight line is an estimate of σ'. The cross-hatched area is its uncertainty of ±1 standard deviation. The difference between the black solid points $\bar{D}(|\Delta\eta|)$ and the straight line σ' is the nonflow contribution. For both the second harmonic and the third harmonic shown in Fig. 4.7(a) and Fig. 4.7(b), respectively, $\bar{D}(|\Delta\eta|)$ decreases as the $\Delta\eta$-gap between two particles increases.

Figure 4.8 shows $\sqrt{\langle v^2\rangle}$ and $\sqrt{\bar{D}}$ for all measured centralities for the second harmonic (a) and the third harmonic (b) with $|\Delta\eta| > 0.7$ [76]. The errors on $\sqrt{\langle v^2\rangle}$ and $\sqrt{\bar{D}}$ are anti-correlated. Taking $|\Delta\eta| > 0.7$, the relative magnitude $\bar{D}_2/\langle v_2^2\rangle = 5\% \pm 0.004\%(stat.) \pm 2\%(sys.)$ for 20-30% centrality. It is clear that $\bar{D}_2$ increases as the collisions become more peripheral.

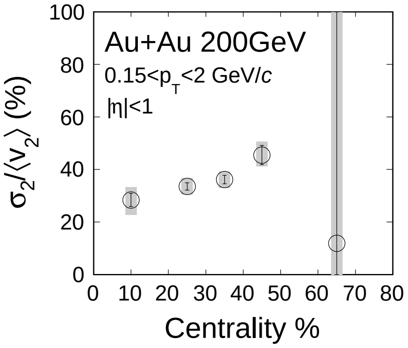

Figure 4.9. The relative elliptic flow fluctuation $\sigma_2/\langle v_2\rangle$ centrality dependence in $\sqrt{s_{\mathrm{NN}}} = 200$ GeV Au+Au collisions. The statistical errors are shown by the error bars. The systematic errors are denoted by the vertical rectangles.

The $\Delta\eta$-dependent nonflow contribution is primarily caused by near-side (small $\Delta\phi$) correlations. These correlations include jet correlations and resonance decays which decrease with increasing $\Delta\eta$. The $\Delta\eta$-independent correlation is dominated by anisotropic flow. However, there should be a $\Delta\eta$-independent contribution from nonflow, such as away-side dijet correlations. The away-side jet contribution should be smaller than the near-side nonflow contribution, because, in part, some of the away-side jets are outside the detector acceptance and, therefore, unrecorded.

Figure 4.9 shows $\sigma_2/\langle v_2 \rangle$ for varies measured centralities. From the central to the peripheral collisions, the relative $\Delta\eta$-independent elliptic flow fluctuation slightly increases. The statistics are limited in the most peripheral centrality bin.

4.3.1 Systematic Uncertainties

The systematic errors for $V\{2\}$ and $V^{1/2}\{4\}$ are estimated by varying event and track quality cuts: the primary event vertex from $|z_{vtx}| < 30$ cm to $|z_{vtx}| < 25$ cm; the number of fit points along the track from greater than 20 to 15; the distance of closest approach to the event vertex from $|dca| < 3$ cm to $|dca| < 2$ cm. The systematic errors for events at 20-30% centrality were found to be 1% for $V_2\{2\}$ and 2% for $V_2^{1/2}\{4\}$, and the same order of magnitude for other centralities.

The fitting error on the parameterized σ' from $\Delta V^{1/2}\{4\}$ is treated as a systematic error, which is 70%, since σ' is consistent with zero in less than 2-σ standard deviation. Similarly, the fitting errors on the parameters used in D are treated as systematic errors that are propagated through to the total uncertainty on D. In addition, there is a systematic error on D that is associated with the choice of fitting function shown as Eq. (4.8), the magnitude of which was estimated using different forms of the fitting function. The forms tried included: an exponential term plus a linear term, a Gaussian function plus a linear term, an exponential function only, a Gaussian function only, and an exponential function plus a term of the form $e^{-\frac{1}{2}(\frac{\Delta\eta}{\sigma})^4}$.

The total estimated uncertainty in the second harmonic of $D(\Delta\eta)$ is an average of 40% based on the different sources evaluated. The systematic error on D also applies to the decomposed flow through $\langle v^2 \rangle = V\{2\} - D$.

4.4 Summary

Two- and four-particle cumulant azimuthal anisotropies are analyzed between pseudo-rapidity bins in Au+Au collisions at $\sqrt{s_{\rm NN}}$ =200 GeV from STAR. Exploiting the collision symmetry about mid-rapidity, The $\Delta\eta$-dependent and the $\Delta\eta$-independent azimuthal correlations in the data are isolated. The $\Delta\eta$-independent correlation $\langle v^2\rangle$, is dominated by flow and flow fluctuations, and is found to be constant over η within the measured range of ± 1 unit of pseudo-rapidity. In the 20-30% centrality Au+Au collisions, the elliptic flow fluctuation is found to be $\sigma_2/\langle v_2\rangle = 34\% \pm 2\%(stat.) \pm 3\%(sys.)$. The $\Delta\eta$-dependent correlation $D(\Delta\eta)$, which may be attributed to non-flow, is found to be $\bar{D}_2/\langle v_2^2\rangle = 5\% \pm 2\%(sys.)$ at $|\Delta\eta| > 0.7$ for $0.15 < p_T < 2$ GeV/c.

5. ‘Ridge’ in d+Au

The deuteron-gold (d+Au) collisions at RHIC were initially proposed as a control experiment to disentangle cold nuclear effect and QGP final state effect for the strong suppression of high p_T particles in central heavy-ion collisions [96–99]. The naive expectation for the small d+Au system is that only the cold nuclear matter effect needs to be considered, where little collective flow can develop. The observation of the long-range $\Delta\eta$ dihadron correlation at small $\Delta\phi$ (called the ridge) in $p + p$ and p+Pb collisions at the Large Hadron Collider (LHC) [100–103] was, therefore, unexpected. As discussed in Section 1.5, the ridge was first discovered in heavy-ion collisions and primarily attributed to triangular anisotropic flow.

To reduce/remove contributions from jetlike correlations, low-multiplicity data were subtracted from dihadron correlations in high-multiplicity data in previous experiments. The application of such a subtraction procedure led to the observation of a back-to-back ridge at $\Delta\phi \sim \pi$, along with the ridge at $\Delta\phi \sim 0$ in p+Pb at $\sqrt{s_{\rm NN}} = 5.02$ TeV. Using the same subtraction technique, the PHENIX experiment also observed a (near- and away-side) double ridge in d+Au collisions at $\sqrt{s_{\rm NN}} = 200$ GeV within their available acceptance of $|\Delta\eta| < 0.7$ [104]. As observed in larger systems, the double ridge is reminiscent of a non-jet, elliptic flow contribution. The ALICE and CMS experiment also reported multi-particle azimuthal v_n for p+Pb [105, 106]. The v_n mass ordering for the π, K and p at low p_T, which is one of the hydrodynamic expectations, is observed in p+Pb by the ALICE experiment [107]. The PHENIX experiment also reported a v_n mass ordering for π and p in d+Au collisions [108]. Other physics mechanisms are also possible, such as the color glass condensate, where the two-gluon density is enhanced at small $\Delta\phi$ over a wide range of $\Delta\eta$ [109–112], the initial state gluon bremsstrahlung effect calculated from the perturbative QCD and sourced by the color antennas [113], or the quantum initial anisotropy from the space momentum uncertainty principle [114].

If jetlike correlations are the same in high- and low-multiplicity events, the dihadron correlation difference between these two event classes would be non-jet physics. However, jet particle production contributes to the overall multiplicity. The selection of high-multiplicity events may demand a relatively large number of jet-correlated particles. In fact, such differences have been observed previously by STAR in the measured two-particle correlations in $p + p$ and various multiplicity d+Au collisions [94, 115]. STAR, with its large acceptance, is well suited to investigate whether and how much event selection affects dihadron jet correlations in d+Au collisions.

5.1 Data Sample and Analysis Cuts

A total of 6.6 million Minimum-Bias (MB) d+Au collisions at $\sqrt{s_{NN}} = 200$ GeV were used in this thesis. These were triggered by the coincidence of signals from the ZDC and the BBC in the year 2003 [67]. The events were selected with the trigger setup names dAuMinBias (2.2 millions) and dAuCombined (4.4 millions) in the dataset. The data chain was reconstructed with the P04if library. The trigger ID was required to be 2001 or 2003. The reconstructed primary tracks in the TPC and the FTPCs were used in the analysis. The event's primary vertex position in z direction was required to be within $|z_{vtx}| < 50$ cm from the TPC center. The detailed track cuts are listed in Table 5.1.

5.2 Centrality Definition in d+Au Collisions

Centrality selections in d+Au collisions are determined by three measures:

- raw charged particle multiplicity (primary tracks) within $|\eta| < 1$ in the TPC,
- raw charged particle multiplicity (primary tracks) within $-3.8 < \eta < -2.8$ in the FTPC Au-going side, and

Table 5.1

d+Au collisions track quality cuts

TPC $\|\eta\| < 1$ or FTPC $2.8 < \|\eta\| < 3.8$
Hit points for TPC tracks ≥ 25 or FTPC tracks ≥ 5
Hit points/possible hit points ≥ 0.51
$dca < 3$ cm
$1 < p_T < 3$ GeV/c

- The neutral charge energy deposit in the Au-going side ZDC quantified by the attenuated ADC signal.

The event cuts for each selection are listed in Table 5.2.

Table 5.2

Centrality Cuts

Centrality	TPC	FTPC-Au	ZDC-Au
0-20%	$N_{ch} \geq 29$	$N_{ch} \geq 17$	$ADC \geq 128$
40-100%	$N_{ch} \leq 19$	$N_{ch} \leq 9$	$ADC \leq 116$

As stated previously in section 5.1 and section 2.2.5, the centrality selection method will be affected by jet contributions, especially in small systems with lower multiplicities. For example, when selecting central d+Au collisions by demanding a high multiplicity in an event, the event in which the jet generated more particles will be preferred. The selected jet may have a large energy so that it can produce more particles, or because of the way the jet fragments there could be more particles in the final state. In short, events with different jet fragmentations are selected into different centrality classes.

5.2.1 Comparison between Centrality Definitions

In order to assess the reliability of the centrality selection methods, the relationships between various centrality selection variables are studied in Figure 5.1 through 5.3. The straight lines are the cuts for the centrality classes of 0-20%, 20-40% and 40-100%. The three left panels are the scatter plots: each dot corresponds to one event. The middle and the right panels are the projections of the two quantities on x- and y-axis, respectively. For example the middle panel in Fig. 5.1 is the average TPC multiplicity as a function of the FTPC-Au multiplicity.

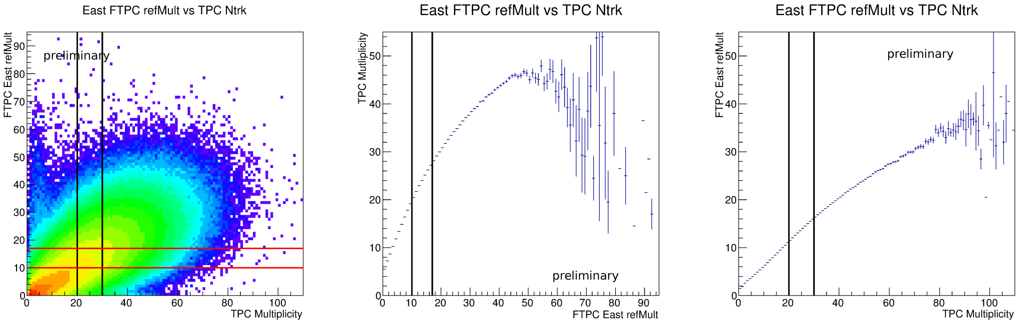

Figure 5.1. Left panel: The FTPC Au-side multiplicity versus TPC multiplicity in d+Au collisions at $\sqrt{s_{\mathrm{NN}}} = 200$ GeV. Middle panel: The mean TPC multiplicity versus FTPC Au multiplicity. Right panel: The mean FTPC multiplicity versus TPC East multiplicity. The color represents the number of events, in increasing order from blue to red.

In Fig. 5.1, the middle and the right panels show that there is a positive correlation between the mid-rapidity multiplicity measured by the TPC and the Au-going side forward multiplicity measured by the FTPC-Au, although the fluctuations are large as seen in the left panel.

In Fig 5.2, the middle panel shows that the FTPC-Au multiplicity slightly increases as the ZDC-Au energy increases when the ZDC-Au Analog-to-Digital Converter (ADC) signal (the signal for the ZDC measured neutral energy) is less than 100. At $100 <$ ZDC-Au < 150, the FTPC-Au multiplicity rapidly increases with

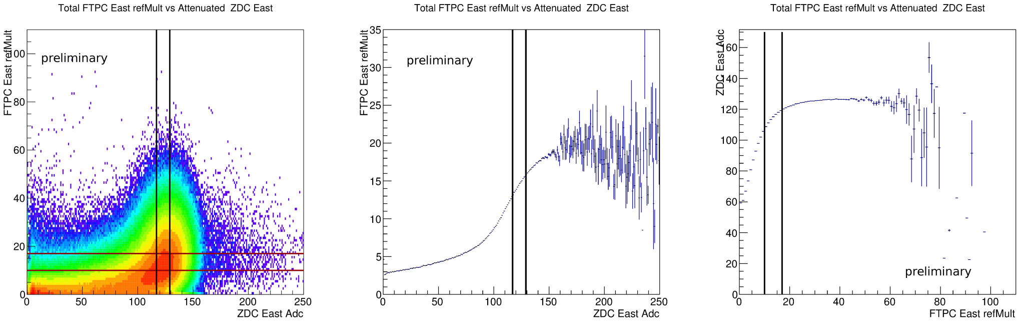

Figure 5.2. The FTPC Au-side multiplicity versus Au-side ZDC ADC in d+Au collisions at $\sqrt{s_{\rm NN}} = 200$ GeV.

the ZDC-Au ADC. At ZDC-Au ADC > 150, the FTPC-Au multiplicity appears to saturate. The right panel shows that the ZDC energy rapidly increases as FTPC-Au multiplicity at FTPC multiplicity < 10 and then it starts to saturate around FTPC multiplicity > 20.

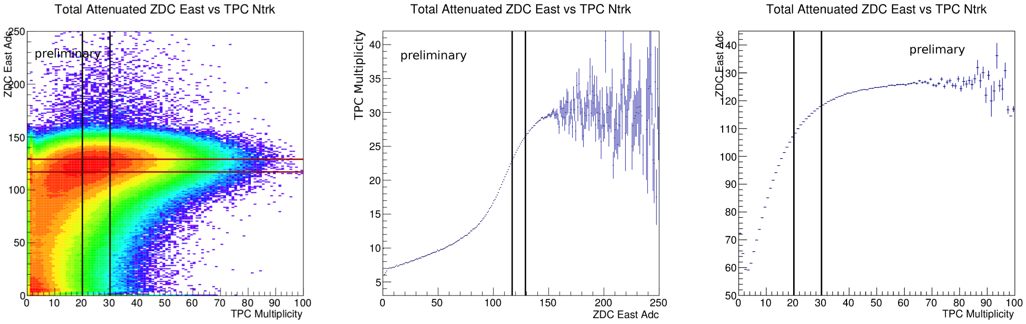

Figure 5.3. The Au-side ZDC ADC versus TPC multiplicity in d+Au collisions at $\sqrt{s_{\rm NN}} = 200$ GeV.

The relationship between the ZDC-Au energy and the TPC multiplicity is similar to the relationship between the ZDC-Au energy and the FTPC-Au multiplicity as shown in Fig. 5.3.

In summary, the TPC, the FTPC-Au multiplicity and the ZDC-Au neutral energy have positive but weak correlations.

5.2.2 Comparison with Au+Au Centrality

For comparison, Figures 5.4 to 5.6 show the relationships between the centrality selections for Au+Au collisions at $\sqrt{s_{\rm NN}} = 200$ GeV. They use the same data sample as in Chapter 3. The TPC multiplicity and FTPC-Au multiplicity show an approximately linear relationship at low multiplicity. At high multiplicity, the FTPC-Au multiplicity starts to saturate as the TPC multiplicity increases. Figure 5.6 is similar to Fig. 2.6. While in Fig. 2.6 the mid-rapidity multiplicity is measured by the CTB, in Fig. 5.6 the mid-rapidity multiplicity is measured by the TPC. Figure 5.5 is similar to Fig. 5.6, but the FTPC-Au saturates at higher multiplicity. From Figures 5.5 and 5.6, the multiplicity (at mid-rapidity and/or forward rapidity) and the ZDC measured neutral energy have a non-monotonic relationship. Their relationship's behavior is discussed in Section 2.2.3. Comparing Figure 5.1 through 5.3 to Figure 5.4 through 5.6, the correlation between various centrality estimating quantities in d+Au collisions are similar to those in peripheral Au+Au collisions (low multiplicity region) as the correlations have similar shapes.

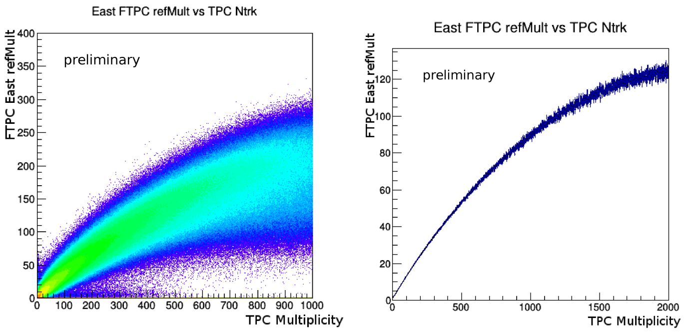

Figure 5.4. The FTPC-Au versus TPC multiplicity in Au+Au collisions at $\sqrt{s_{\rm NN}} = 200$ GeV.

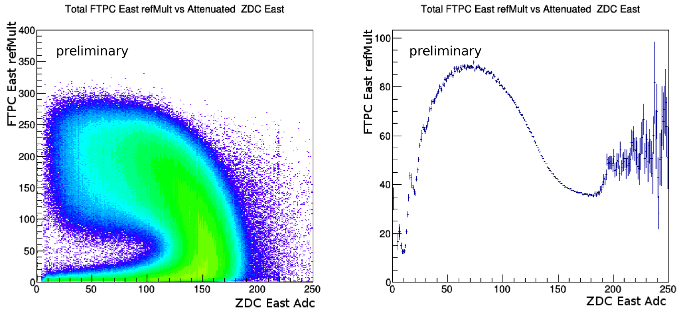

Figure 5.5. The FTPC Au-side multiplicity versus Au-side ZDC ADC in Au+Au collisions at $\sqrt{s_{\rm NN}} = 200$ GeV.

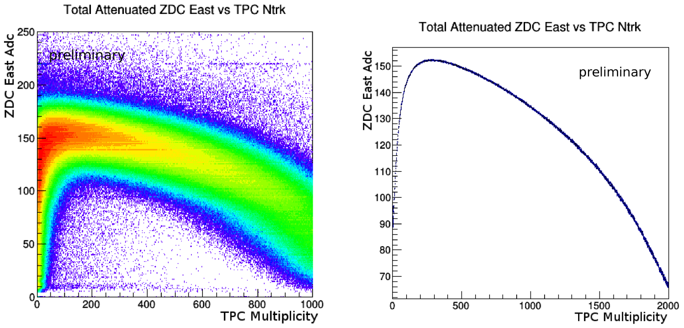

Figure 5.6. The Au-side ZDC ADC and TPC multiplicity in Au+Au collisions at $\sqrt{s_{\rm NN}} = 200$ GeV.

5.3 Correlation Analysis

The TPC-TPC dihadron correlation is measured with the trigger and associated particles both from the TPC detector. The TPC-FTPC correlation is measured with the trigger particle from the TPC and the associated particle from the FTPC. Both the correlations are normalized per trigger particle. The detector acceptance is corrected by the event-mixing technique. The dihadron correlation is given in Eq. (1.6). The details of the correlation analysis are described in Section 1.5.

The left panel of Fig. 5.7 shows $S(\Delta\eta, \Delta\phi)$ for the TPC-TPC correlation, and the left panel fo Fig. 5.8 shows $S(\Delta\eta, \Delta\phi)$ for the TPC-FTPC correlation. Both the trigger and the associated particle are from $1 < p_T < 3$ GeV/c. The correlation data are corrected for the associated particle tracking efficiency of 85% ± 5% (sys.) for TPC tracks, and 75% ± 5% (sys.) for FTPC tracks [94, 115]. The efficiency does not vary from central to peripheral d+Au collisions. The right panel of Fig. 5.7 shows $B(\Delta\eta, \Delta\phi)$ for the TPC-TPC correlation, and the right panel of Fig. 5.8 shows $B(\Delta\eta, \Delta\phi)$ for the TPC-FTPC correlation. The triangle shape of the mixed event is due to the η acceptance cut of $-1 < \eta < 1$ for TPC, and $2.8 < |\eta| < 3.8$ in FTPC. $B(\Delta\eta, \Delta\phi)$ is normalized to be 1 at $\Delta\eta|_{100\%} = 0$ for the TPC-TPC correlation, and at $\Delta\eta_{100\%} = \pm 3$ for the TPC-FTPC correlation (-3 for FTPC east and 3 for west) by dividing by $\langle B(\Delta\eta|_{100\%}, \Delta\phi)\rangle$. This is because the detector pair acceptance is 100% at $\Delta\eta|_{100\%}$. In order to mix the events with similar detector geometry and collision conditions, the mix event matching requirements are imposed. The mixed events are required to be within 1 cm in z_{vtx}, and to have the same multiplicity (for TPC or FTPC centrality) or within the same ADC bin of bin size 10 (for ZDC centrality). To increase statistics, ten mixed events are performed for each trigger particle.

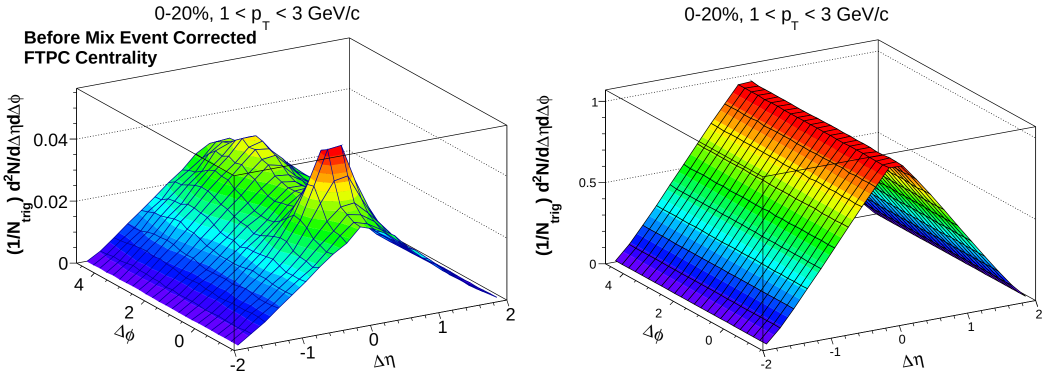

Figure 5.7. Real event (left panel) and mixed event (right panel) TPC-TPC correlations in 0-20% central d+Au collisions.

After the two-particle correlations are measured, two approaches are taken to analyze the data. One is to look at the associated particle correlated yield per trigger particle after ZYAM background subtraction. It is assumed that the underlying event

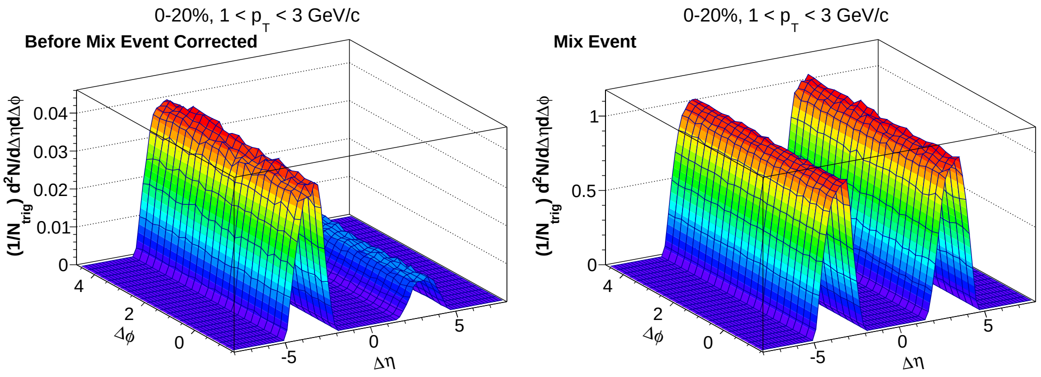

Figure 5.8. Real event (left panel) and mixed event (right panel) TPC-FTPC correlations in 0-20% central d+Au collisions.

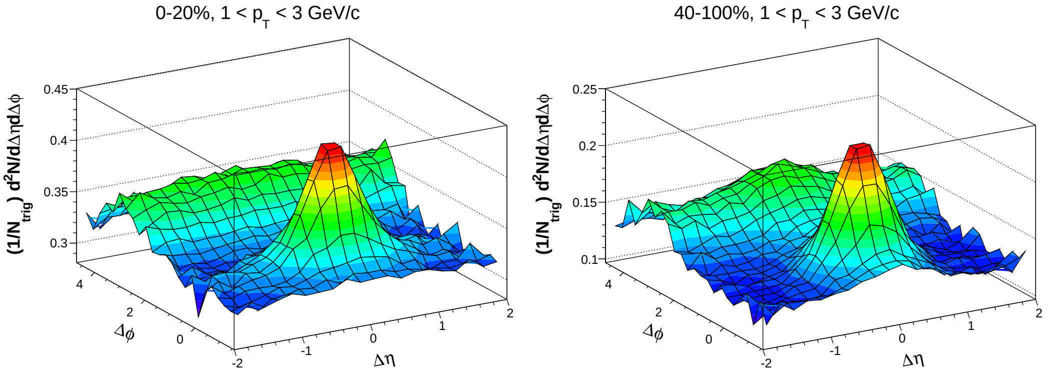

Figure 5.9. The two-particle TPC-TPC correlations in 0-20% (left panel) and 40-100% (right panel) central d+Au collisions. The two-particle correlation is corrected by mixed events.

background in d+Au collisions is a uniform distribution over $\Delta\phi$, with magnitude depending on $\Delta\eta$. The ZYAM background value is determined by the lowest yield of the $\Delta\phi$ distribution in each $\Delta\eta$ bin. To minimize statistical fluctuations from a single $\Delta\phi$ point, the lowest yield is calculated as the lowest average in a $\Delta\phi$ window of a certain width. The default $\Delta\phi$ width is 0.4 radians. The ZYAM systematic error is estimated by varying the $\Delta\phi$ width from 0.2 to 0.6 radians. After subtracting the yield in $C(\Delta\eta, \Delta\phi)$ by the ZYAM background, the correlated yield at its minimum

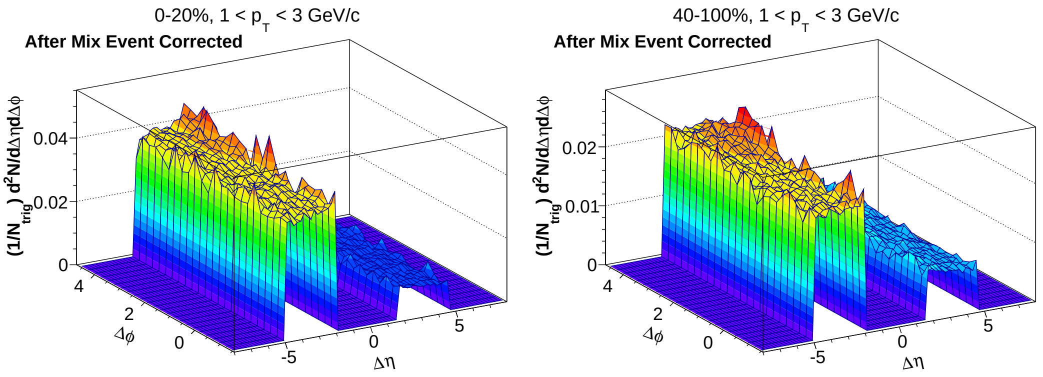

Figure 5.10. The two-particle TPC-FTPC correlations in 0-20% nd 40-100% central d+Au collisions. The two-particle correlation is corrected by mixed events.

will be ‘zero’ (this is for the average over the chosen $\Delta\phi$ window, not for specific $\Delta\phi$ bin). In this approach, after ZYAM subtraction of the underlying event, one can examine how the correlated yield varies over $\Delta\phi$ and $\Delta\eta$.

Another approach to analyze the Fourier coefficients is,

$$\frac{dN}{d\Delta\phi} \propto 1 + \sum_{n} 2V_n \cos(n\Delta\phi), \tag{5.1}$$

where no background subtraction is needed. In Equation (5.1), the $\Delta\phi$-independent combinatorial background goes into the first term “1”. A non-zero Fourier coefficient does not necessarily mean collective anisotropic flow. Any function can be expanded by the Fourier series. In order to infer possible physics from the Fourier coefficients V_n, the V_n needs to be studied as a function of other observables, such as $\Delta\eta$ and multiplicity. Important questions need to be asked, include why and how collective flow, if any, develops in the small system and how low in multiplicity hydrodynamics still apply and QGP can still form.

5.3.1 Systematic Uncertainty

The systematic uncertainties on the correlated yields are dominated by the ZYAM background subtraction and the 5% tracking efficiency uncertainty. They are included in the results presented in the correlated yield distributions.

ZYAM is taken as the lowest correlation magnitude averaged over a $\Delta\phi$ window of full width 0.4. The ZYAM systematic uncertainty is estimated by changing this ZYAM $\Delta\phi$ width to 0.2 and 0.6.

The tracking efficiency is 85% for the TPC, and 75% for the FTPC. The 5% relative uncertainty due to the tracking efficiency correction is taken from previous publications [78, 115] (estimated by variations in the TPC gas mixture, temperature, pressure, and ionization electron drift velocity).

Systematic uncertainty in the raw correlation function is dominated by the 5% tracking efficiency uncertainty.

5.4 Two-Particle Correlation at Mid-Rapidity

The two-particle correlation at mid-rapidity is calculated by the TPC-TPC correlation, while both the trigger and the associated particles are from TPC.

5.4.1 Central and Peripheral $\Delta\phi$ Correlations

The associated particle yields after the ZYAM subtraction are analyzed as a function of $\Delta\phi$ for three different $|\Delta\eta|$ regions: $|\Delta\eta| < 0.3$, $0.5 < |\Delta\eta| < 0.7$, and $1.2 < |\Delta\eta| < 1.8$. Both the trigger and the associated particles are taken from the TPC. The FTPC centrality selection is used instead of the TPC one for the TPC-TPC correlation in order to avoid auto-correlation from the same tracks being used for both the correlation analysis and the centrality selection.

In Fig. 5.11, the central 0-20% collisions are represented by the red solid dots. The peripheral 40-100% collisions data are the blue solid dots. The error bars are the statistical errors of the data points. The boxes are the systematic errors, which is the quadratic sum of the systematic errors due to the efficiency and the ZYAM, as well as the statistical error of the ZYAM, because the ZYAM statistical error is shared by all $\Delta\phi$ bins. The subtracted ZYAM background magnitudes are listed in the figures. The numbers in the parenthesis are the errors. The first number is the statistical error and the second two are the systematic errors. The location of the minimum yield is indicated by the arrows.

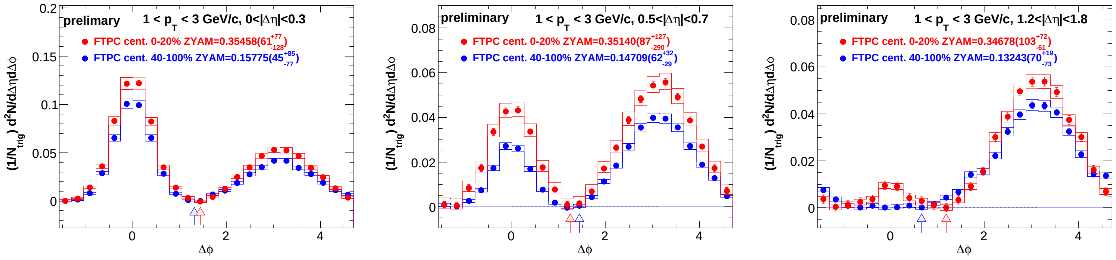

Figure 5.11. The TPC-TPC correlation in $|\Delta\eta| < 0.3$ (left panel), $0.5 < |\Delta\eta| < 0.7$ (middle panel), and $1.2 < |\Delta\eta| < 1.8$ (right panel) in d+Au collisions at $\sqrt{s_{\mathrm{NN}}} = 200$ GeV. The centrality is selected by the FTPC-Au multiplicity.

Figure 5.11 left panel shows that, at $|\Delta\eta| < 0.3$, the near-side jet peak contributes to the near-side yield. The near-side correlated yield is two times larger than the away-side correlated yield for both the central and peripheral collisions. The ZYAM value is 0.3546 ± 0.0006 (stat.) $^{+0.0008}_{-0.0013}$ (sys.) for the central and 0.1578 ± 0.0005 (stat.) $^{+0.0009}_{-0.0008}$ (sys.) for the peripheral collisions. The $\Delta\phi$ locations for the ZYAM are close to each other for central and peripheral collisions, as the arrows indicate.

The $0.5 < |\Delta\eta| < 0.7$ region is the $\Delta\eta$ range used in the PHENIX [104]. The $0.5 < |\Delta\eta| < 0.7$ is still affected by the near-side jet peak, which can be seen from the large near-side peak in peripheral collisions. Figure 5.11 middle panel shows that the near-side correlated yield is slightly smaller than the away-side correlated yield for both the central and peripheral collisions The ZYAM values are similar to but slightly smaller than those for $|\Delta\eta| < 0.3$.

The $1.2 < |\Delta\eta| < 1.8$ region is considered unaffected by the near-side jet peak, which can be seen from the zero near-side peak for peripheral collisions, while the away-side jet is still present. The ZYAM values are smaller than the mid-rapidity cases. The ZYAM decrease in peripheral collisions is larger than the decrease in central collisions.

As $|\Delta\eta|$ increases in Fig. 5.11 from the left panel to the right panel, the near-side ($\Delta\phi \approx 0$) yield (the peak area) decreases, while the away-side yield ($\Delta\phi \approx \pi$) stays almost the same for both central and peripheral collisions. However, the central yield is larger than the peripheral one at both $|\Delta\phi| \approx 0$ and $|\Delta\phi| \approx \pi$ for all three $|\Delta\eta|$ windows. Even for the large $1.2 < |\Delta\eta| < 1.8$ in the right panel of Fig. 5.11, while the peripheral data are consistent with zero, the central data show a peak on the near side. Subtracting the peripheral correlation from the central one, i.e. the "central−peripheral" technique, the associated particle yields will have the double ridge structure (peaks at $\Delta\phi = 0$ and π) for all the $|\Delta\eta|$. One could attribute the difference obtained from "central−peripheral" to the ridge if one assumes that the jet correlations are the same in central and peripheral collisions and are therefore subtracted.

5.4.2 The Near-side Jetlike $\Delta\eta$ Correlations

This section quantifies the near-side jetlike correlation in central and peripheral d+Au collisions. The term "jetlike" is used instead of "jet" because other correlations are also present, such as resonance decays. The parts of the dihadron correlations used for the jet study are therefore referred to as "jetlike" correlations.

To compare the jetlike correlations in central and peripheral collisions, the near-side $\Delta\eta$ distribution is studied, because the jetlike contribution is located within a small $\Delta\eta$ angle. Figure 5.12 shows the near-side $\Delta\eta$ projection as the red symbols.

The away-side yields are the blue symbols. The near side is defined as $|\Delta\phi| < \pi/3$. The away side is defined as $|\Delta\phi - \pi| < \pi/3$. The error bars are statistical errors of the data points, including those from the ZYAM values since they are independent of the $\Delta\eta$ bins. The boxes are the systematic errors from the tracking efficiency and ZYAM systematic errors. Both the near-side yield magnitudes and shapes are different in the central d+Au collisions from those in the peripheral collisions. A Gaussian+pedestal (a single constant number) function is used to fit the near-side correlation formula: the fit results of the near side for central and peripheral data are listed in the plots. There are three parameters in the fitting. The Gaussian area N represents the near-side jetlike correlated yield $Y_{jetlike}$ per radian in $\Delta\phi$. The Gaussian width σ represents the near-side jetlike peak width. The pedestal is C. The fit χ^2/ndf for both the central and peripheral collisions are less than 1. The near-side jetlike peak is larger and wider in central d+Au collisions than in peripheral collisions. A similar broadening of the jetlike peak was previously observed in d+Au collisions compared to that in p+p collisions [94]. The away side shapes in Fig. 5.12 are weakly dependent on $\Delta\eta$, as expected from the away-side jet or the ridge.

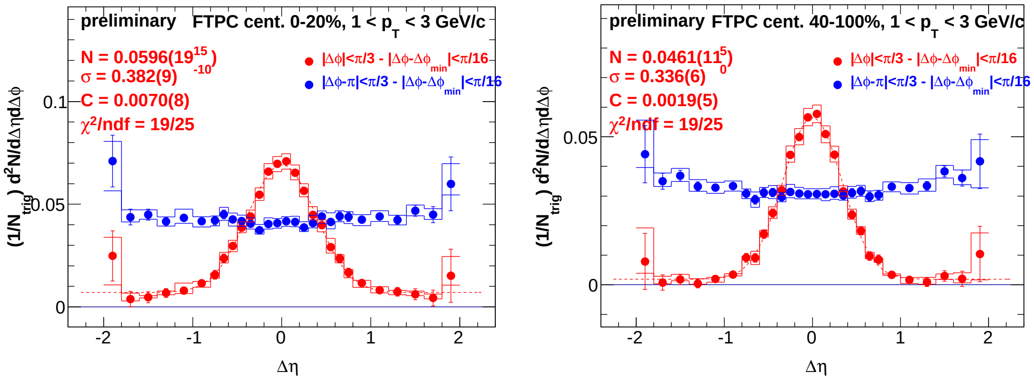

Figure 5.12. The near-side and away-side $\Delta\eta$ projection for the FTPC-Au multiplicity selected central (left panel) and peripheral (right panel) collisions. $|\Delta\phi| < \pi/3$ is near side. $|\Delta\phi - \pi| < \pi/3$ is away side. The "$|\Delta\phi - \Delta\phi_{min}| < \pi/16$" represents the ZYAM value at minimal $\Delta\phi_{min}$ average with bin width $\pi/16$.

The "central−peripheral" $\Delta\eta$ distribution is shown in the left panel of Fig. 5.13. The near side, the red dots, has a Gaussian shape, while the away side, the blue points, is more or less constant over $\Delta\eta$. The red and blue solid curves are the Gaussian fits to the near side and the away side, respectively. The red and blue dashed curves are the constant fits to the near side and the away side. For the near side, the constant fit gives a $\chi^2/ndf = 49.5/9$ and the Gaussian fit gives a $\chi^2/ndf = 1.9/7$. For the away side, the Gaussian fit χ^2/ndf is 5.8/7 and the constant fit χ^2/ndf is 6.4/9. The Gaussian fit gives a very large σ, effectively consistent with a constant fit. The difference obtained from the "central−peripheral" is therefore consistent with a Gaussian peak on the near side and a uniform distribution on the away side. These shapes resemble jetlike features. The non-zero difference, therefore, likely arise from jetlike origins.

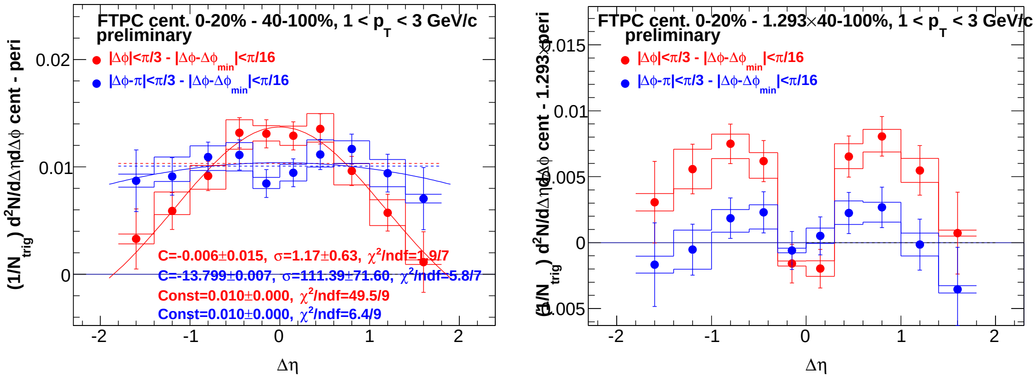

Figure 5.13. Near-side and away-side $\Delta\eta$ projection for "central−peripheral" (left panel) and "central−scaled peripheral" by Eq. (5.2) (right panel).

One way to account for the peripheral and central jet yields discrepancy is to scale the peripheral correlation up so that the peripheral near-side jetlike yield (technically, the Gaussian area on the near side) is the same as the central jetlike yield. Namely,

$$C^{central} - \alpha C^{peripheral}_{jetlike}, \tag{5.2}$$

where

$$\alpha = \frac{N_{jetlike}^{central}}{N_{jetlike}^{peripheral}}. \tag{5.3}$$

Here $C^{central}$ and $C^{peripheral}$ are the two-particle correlations (the associated particle yields, not the fit parameter C written in the plots) in the central and peripheral collisions, respectively. $N_{jetlike}^{central}$ and $N_{jetlike}^{peripheral}$ are the fit parameters N for the central and peripheral collisions, which are the Gaussian areas representing the near-side jetlike yields. The scaling method certainly does not make the peripheral jetlike contribution look exactly the same as in the central d+Au collisions. This is because their shape difference has not been taken into account. Nevertheless, the scaling method provides a first order approximation. The scaling method with the near-side jetlike yield ratio assumes that the away-side correlated yield scales with the near-side yield from peripheral to central d+Au collisions, which is reasonable based on dijet momentum conservation.

The α parameter, the ratio of the central to peripheral jetlike correlated yields, indicates how strong the event-selection effect is on the jetlike correlated yield. The fit results give $\alpha = 1.29 \pm 0.05$ (stat.) ± 0.2 (sys.) for FTPC centrality 0-20% to 40-100%. Meanwhile, the ratio of the away-side correlated yields are 1.32 ± 0.02 (stat.) ± 0.01 (sys.). The α parameter for the near-side jetlike yield is consistent with the away-side yield ratio of central to peripheral collisions. This suggests that the away-side difference between central and peripheral collisions is also mainly due to jets.

The result of Eq. (5.2) is shown in the right panel of Fig. 5.13. The red dots represent the near side. The blue dots represent the away side. After the subtraction of the scaled peripheral yield to take the jet difference into account, the away-side difference between the central and peripheral collisions is consistent with zero. As aforementioned, the zero away-side yield difference suggests that the difference of the away side between central and peripheral events may primarily be due to a difference in jetlike correlations for different event selection. The near-side difference is reduced.

The shape of the near-side difference is the result of the subtraction of a narrow Gaussian from a wide Gaussian of equal area and an offset by a pedestal.

5.5 Event-Selection Effect on Jetlike Correlated Yield

5.5.1 Centrality Selection Methods

Besides the FTPC-Au multiplicity selection effect on the jetlike near-side correlated yield as discussed in Section 5.4.2, there are two other centrality selection methods: the TPC multiplicity and the ZDC-Au neutral energy. The near side and away side correlated yield distributions in central and peripheral collisions selected by the TPC multiplicity are shown in the left and middle panels of Fig. 5.14, while those selected by the ZDC energy ones are shown in left and middle panels Fig. 5.15. The TPC multiplicity centrality selection is expected to have a larger centrality selection effect on the jetlike correlation than the FTPC centrality one, as the right panel of Fig. 5.14 shows. When using the TPC multiplicity for the centrality, the near-side jetlike peak is of greater magnitude than the one using the FTPC multiplicity. The strong TPC centrality selection effect is due to auto-correlation (the same tracks being used for both the centrality selection and the dihadron correlation study). On the other hand, the ZDC-Au neutral energy as centrality selection has a weaker effect, as the right panel of Fig. 5.15 shows. The weaker ZDC centrality effect is expected from the large pseudo-rapidity (near the beam pipe), and the fact that the ZDC measures the neutral spectators which are not directly related to the charged particles in the mid-rapidity used for the dihadron correlation study. The Gaussian and the constant fitting results are listed in the plots for the TPC and the ZDC-Au centrality selections, similar to Fig. 5.12.

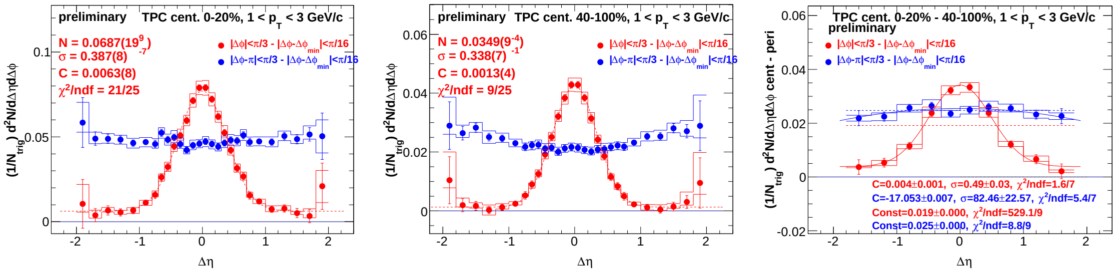

Figure 5.14. The near-side and the away-side $\Delta\eta$ projection for the TPC multiplicity selected central (left panel) and peripheral (middle panel) collisions. The "central−peripheral" difference (right panel) shows a strong jetlike correlation feature.

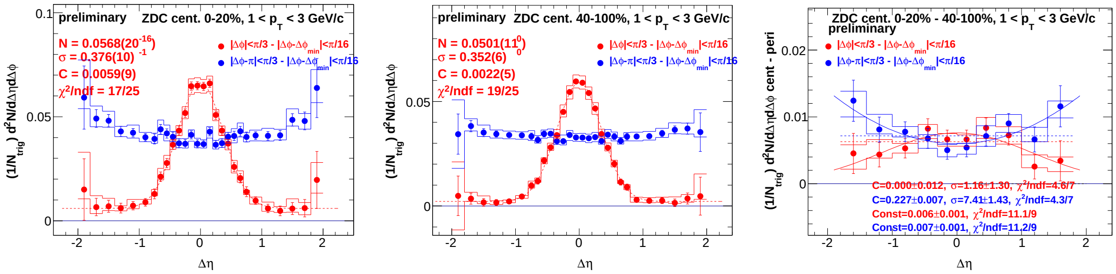

Figure 5.15. The near-side and the away-side $\Delta\eta$ projection for the ZDC-Au energy selected central (left panel) and peripheral (middle panel) collisions. The "central−peripheral" (right panel) method shows weak jetlike feature.

5.5.2 Multiplicity Dependence

To further investigate the influence of event selection on jetlike correlations, Fig. 5.16 shows Y_{jetlike} as a function of the event activity (centrality), represented by the mid-rapidity raw (efficiency uncorrected) charged hadron $dN/d\eta$, in events selected according to the FTPC-Au multiplicity (solid squares) and the ZDC-Au neutral energy (open squares), respectively. The systematic uncertainties are obtained by Gaussian fits to the $\Delta\eta$ correlations varied by the ZYAM systematic uncertainties. The MB events are divided into five centrality classes as listed in Table 5.3. Figure 5.16

shows that the near-side jetlike correlated yield continues to increase with increasing event multiplicity. ALICE also reports a jetlike correlation increase with multiplicity in p+Pb collisions at $\sqrt{s_{\rm NN}} = 5.02$ TeV [116]. The comparison with the HIJING model [117] is illustrated by the curve in Fig. 5.16. HIJING is a Monte Carlo program to study jet and associated particle production in high energy collisions based on QCD inspired model for multiple jets production [117]. HIJING shows no increase of jetlike yield with the multiplicity increase. The HIJING calculations are scaled down for all centrality bins by the same factor such that the lowest multiplicity bin matches real data.

Table 5.3
The centrality class cuts for the FTPC multiplicity and the ZDC attenduated ADC signal.

Centrality	0-10%	10-20%	20-40%	40-60%	60-100%
FTPC-Au multiplicity	[22,500]	[17,21]	[10,16]	[6,9]	[0,5]
ZDC-Au ADC	[133,500]	[129,132]	[117,128]	[100,116]	[0,99]

5.5.3 p_T Dependence

The jetlike ratio α parameter can quantify the effect of event selection on jetlike correlations. Figure 5.17 shows the p_T dependence of the α parameter. The systematic uncertainties are given by ZYAM uncertainties as in Fig. 5.16. Two sets of data points are shown. One shows the α parameter as a function of the associated particle $p_T^{(a)}$ with the trigger p_T fixed in $0.5 < p_T^{(t)} < 1$ GeV/c . This trigger p_T range is similar to the $0.5 < p_T^{(t)} < 0.75$ GeV/c used by PHENIX [104]. The α parameter is larger than unity and relatively insensitive to $p_T^{(a)}$ for this particular $p_T^{(t)}$ choice. The other set of points show α as a function of $p_T^{(t)}$ with $0.5 < p_T^{(a)} < 1$ GeV/c fixed. The α parameter seems to decrease with $p_T^{(t)}$.

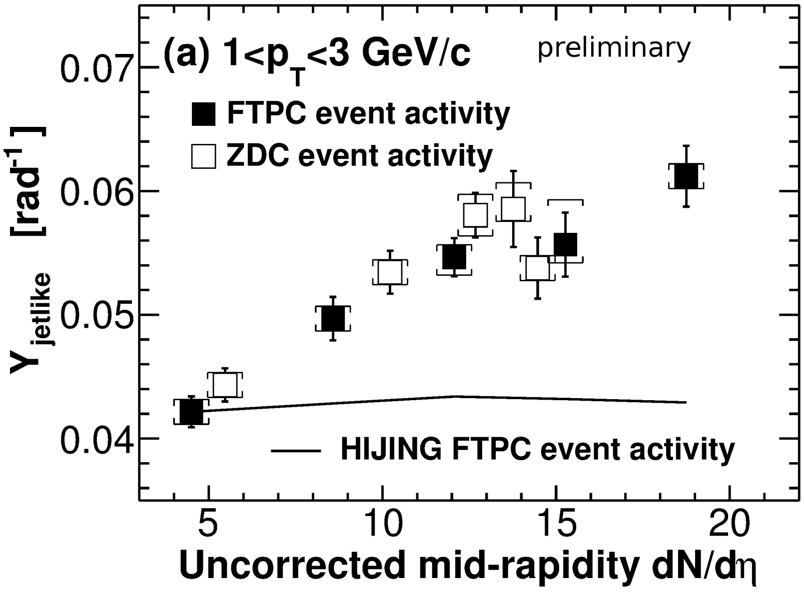

Figure 5.16. The near-side jetlike correlated yield, obtained from a Gaussian+pedestal fit to $\Delta\eta$ distribution, as a function of the uncorrected mid-rapidity $dN/d\eta$ measured in the TPC. Two event selections are used: the FTPC-Au multiplicity (filled squares) and the ZDC-Au energy (open squares). The curve is the result of a HIJING calculation. Error bars are statistical and caps show the systematic uncertainties.

5.5.4 Discussion

There could be multiple reasons for the event-selection effect on jetlike correlations. One is a simple selection bias due to self-correlation for the centrality definition using TPC multiplicity. Such a bias may also be present for the centrality definition using FTPC-Au multiplicity: because the away-side jet can contribute to the FTPC-Au multiplicity. A high FTPC-Au multiplicity could preferentially select larger multiplicity jets (either of larger energy or happening to fragment into more particles). However, such a bias is not observed in the HIJING model implementation. Possibly because dijet production in HIJING resulting in hadrons in studied p_T range of $1 < p_T < 3$ GeV/c may be negligible at the FTPC pseudo-rapidity region.

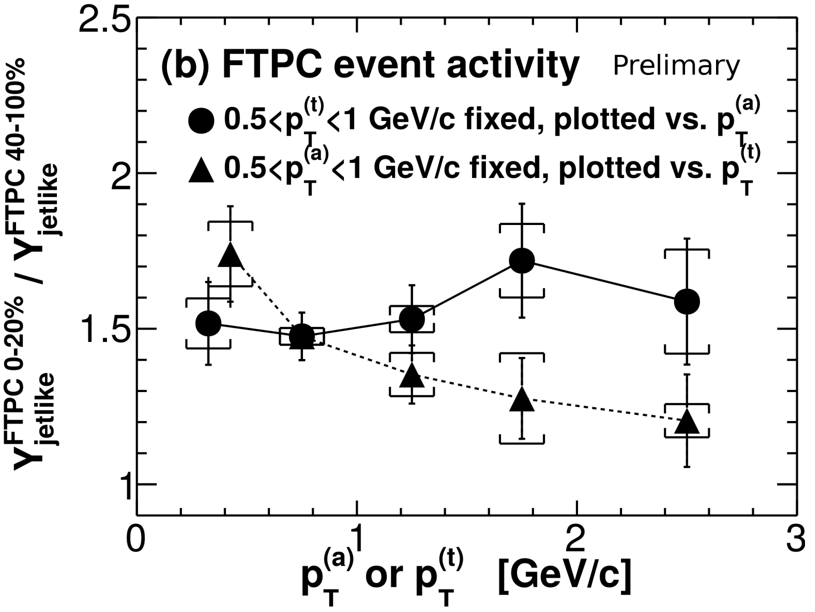

Figure 5.17. The ratio of the correlated yields in high to low FTPC-Au multiplicity events as a function of $p_T^{(a)}$ ($p_T^{(t)}$) where $p_T^{(t)}$ ($p_T^{(a)}$) is fixed. Error bars are statistical and the caps show the systematic uncertainties.

Centrality selection bias is unlikely present in events selected by the ZDC energy. Event centrality dependent sampling of jet energies could also be caused by physics rather than selection biases; for example, there could be positive correlations between jet production and the underlying event. There could also be a genuine dependence of jetlike correlations on event activity, such as initial-state k_T effects due to initial state multiple scattering or even final-state jet modifications by possible medium formation [98, 99] in the small d+Au collision system.

5.5.5 Low-Multiplicity Data Subtraction

The open circles in Fig. 5.18 represent the difference between central and peripheral events, with the latter first multiplied by the α parameter from the fit. The scaling is essentially a first order correction to the multiplicity selection effect on jetlike correlations. Indeed, the away-side yields are approximately zero for all $|\Delta\eta|$ ranges shown in Fig. 5.18. The vanishing away-side difference suggests that the difference in the away-side long-range correlations between central and peripheral events is mostly from jetlike correlations.

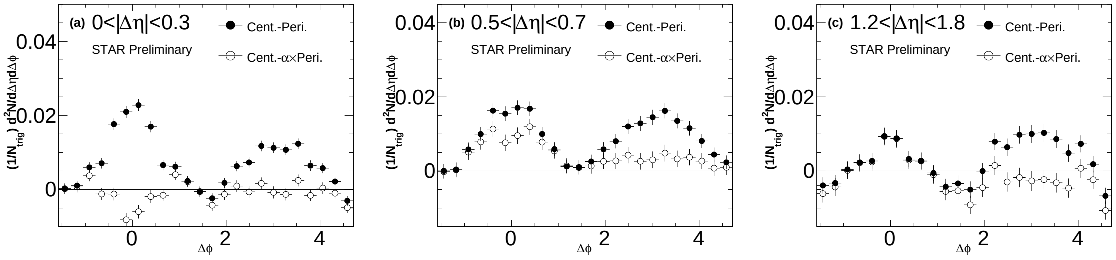

Figure 5.18. Dihadron $\Delta\phi$ correlation difference between high- and low-multiplicity collisions in (a) $0 < |\Delta\eta| < 0.3$, (b) $0.5 < |\Delta\eta| < 0.7$ and (c) $1.2 < |\Delta\eta| < 1.8$ in d+Au collisions at $\sqrt{s_{\mathrm{NN}}} = 200$ GeV for charged particles of $1 < p_T < 3$ GeV/c. Both the trigger and associated particles are from the TPC. FTPC-Au multiplicity is used for event selection. The solid dots represent "central−peripheral.". The open circles represent "central−$\alpha\times$peripheral.", where α is near-side Gaussian area ratio in central to peripheral collisions. The error bars are statistical errors.

The solid dots in Fig. 5.18 show the simple difference between central and peripheral data, is similar to the measurement by PHENIX [104]. The peak magnitudes on the near-side and away-side turn out to be similar, resembling a double ridge. As the large acceptance STAR data show, the resulting double-ridge structure may well be due to residual jetlike correlations which remain after the simple subtraction of the peripheral data from the central data.

5.6 Two-Particle $\Delta\phi$ Correlation at Forward Rapidities

The FTPCs cover $2.8 < |\eta| < 3.8$ acceptance on each side. Studying the two-particle correlations with the trigger particle in the TPC and the associated particle in the FTPC will allow access to the large $|\Delta\eta|$ region, where the near-side jet contribution should be minimal. Figure 5.19 shows such correlations.

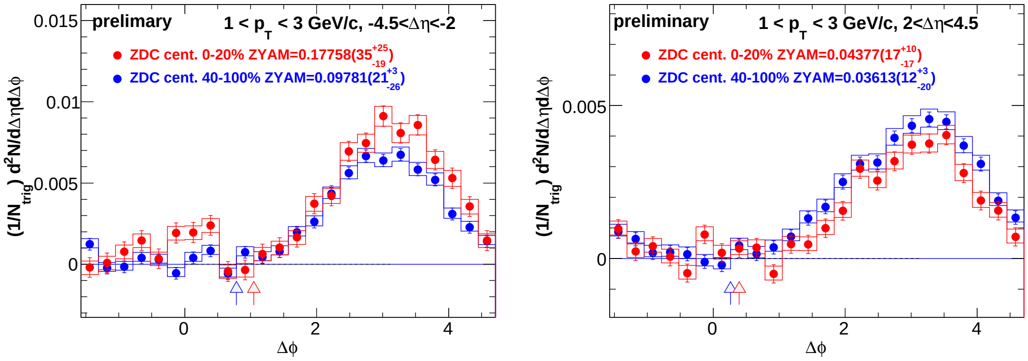

Figure 5.19. Two-particle TPC-FTPC correlated yield $\Delta\phi$ distributions at $-4.5 < \Delta\eta < -2$ (left panel) and $2 < \Delta\eta < 4.5$ (right panel).

As Fig. 5.19 shows, on the away side, for the Au-going side, the central data (red points) are larger than the peripheral data (blue points); for the d-going side, it is the opposite behavior. The difference in behaviors of the Au-going and the d-going sides may be related to the difference in underlying parton distribution because different x ranges are probed by the Au-going or the d-going side correlations. On the near side, for the Au-going side, the central yield has an excess over the peripheral yield (the later is consistent with zero); for the d-going side, the central and peripheral yields are both consistent with zero.

5.7 Near-Side Long-Range Ridge $\Delta\eta$ Dependence

To further understand the near-side ridge, the near-side and away-side correlated yields in central d+Au collisions are plotted as a function of $\Delta\eta$ with both the TPC-TPC and the TPC-FTPC correlations on the same graph in Fig. 5.20. To avoid self-correlations, the ZDC-Au centrality selection is used for both correlations. For comparison, the ZYAM magnitude is also plotted. The points at $\Delta\eta < -2$ and the

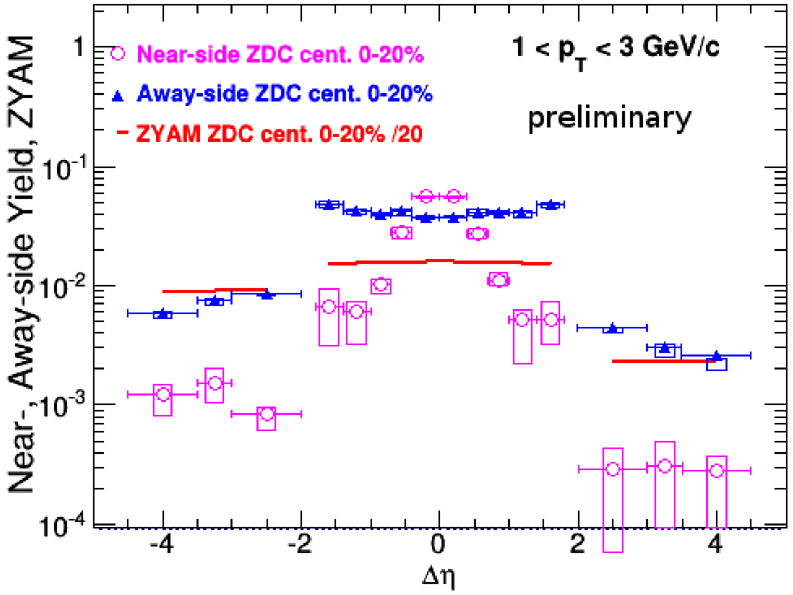

Figure 5.20. The $\Delta\eta$ dependence of the near-side and away-side correlated yields and the estimated ZYAM background (scaled by 1/20).

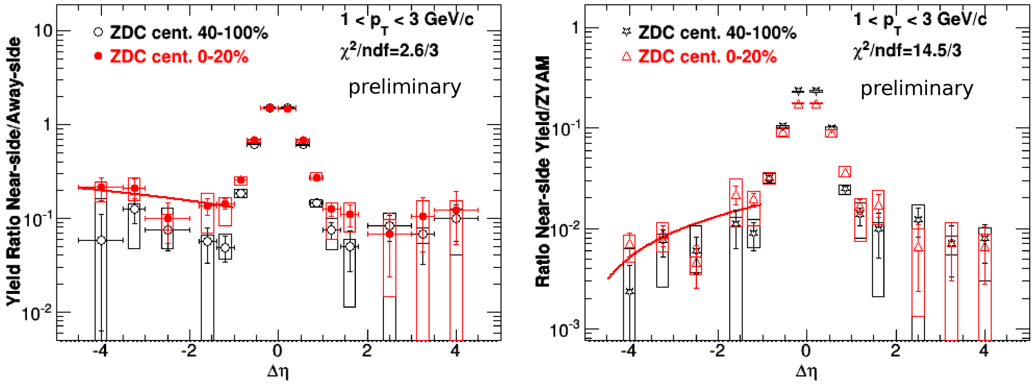

Figure 5.21. Left panel: the $\Delta\eta$ dependence the ratio of the near-side to away-side correlated yields. The solid line is a linear fit to the ratio in central d+Au collisions, yielding a slope of $(-2.2 \pm 1.8) \times 10^{-2}$. Right panel: the $\Delta\eta$ dependences the ratio of the near-side correlated yield to the ZYAM values. The solid line is a linear fit to the ratio in central d+Au collisions, yielding a slope of $(4 \pm 1) \times 10^{-3}$.

points at $\Delta\eta > 2$ are from the TPC-FTPC correlations. The others are from the TPC-TPC correlations. The near-side yields are the pink circles. The away-side yields are the blue triangles. The ZYAM values are represented by the red lines. There is a step at $|\Delta\eta| = 2$ between the two sets of correlation data. This step is due to the fact that the particle pairs with $\Delta\eta$ to the left of the step and those which $\Delta\eta$ to the right come from different kinematic regions (TPC particles have $-1 < \eta < 1$ and FTPC particles have $-3.8 < \eta < -2.8$ or $2.8 < \eta < 3.8$) even though their $\Delta\eta$ gaps are similar at the step.

To possibly elucidate the formation mechanism of the ridge, the ratio of the near-side to the away-side correlated yields is studied in left panel of Fig. 5.21. The solid dots are the central data. The open circles are the peripheral data. While the large peak at $\Delta\eta \approx 0$ is due to the near-side jet, the ratio is rather uniform in $\Delta\eta$ at $|\Delta\eta| > 1$. A linear fit to the $\Delta\eta < -1$ region gives a slope of $(-2.2 \pm 1.8) \times 10^{-2}$. The linear fit indicates that the ratio is consistent with a constant within one standard deviation. Since the away-side correlated yields are dominated by jets, the $\Delta\eta$-independent ratio may suggest a connection between the near-side ridge and dijet production, even though any possible jet contribution to the ridge at $|\Delta\eta| > 1$ should be minimal.

On the other hand, the near-side ridge does not seem to scale with the ZYAM magnitude. A linear fit to the ratio of the near-side correlated yield over ZYAM indicates a slope of $(4 \pm 1) \times 10^{-3}$ in $\Delta\eta$ which differs from zero by four standard deviations, as the right panel of Fig. 5.21 shows.

5.8 Fourier Coefficients

The above correlated yields are subject to ZYAM background subtraction. Another way to study the correlations is to use Fourier series, which can characterize all azimuthal functions. The Fourier coefficients are calculated by

$$V_n(\Delta\eta) = \langle \cos(n\Delta\phi) \rangle = \frac{\int_0^{2\pi} C(\Delta\eta, \Delta\phi) \cos(n\Delta\phi) d\Delta\phi}{\int_0^{2\pi} C(\Delta\eta, \Delta\phi) d\Delta\phi}. \tag{5.4}$$

$C(\Delta\eta, \Delta\phi)$ is the correlation function, see Eq. (1.6) in Section 5.3. V_n is the average of the $\cos(n\Delta\eta)$ over the trigger-associated pairs in the selected $\Delta\eta$ window for all events.

5.8.1 Systematic Uncertainty

Systematic uncertainties in the Fourier coefficients in Fig. 5.25 are estimated to be 5% for V_1 and 10% for V_2, while V_3 is consistent with zero within 2σ. It is estimated by varying the *dca* from the default 3 cm to 2 cm, and varying number of hit points from the default 25 points to 20 points (see Figures 5.22 through 5.24).

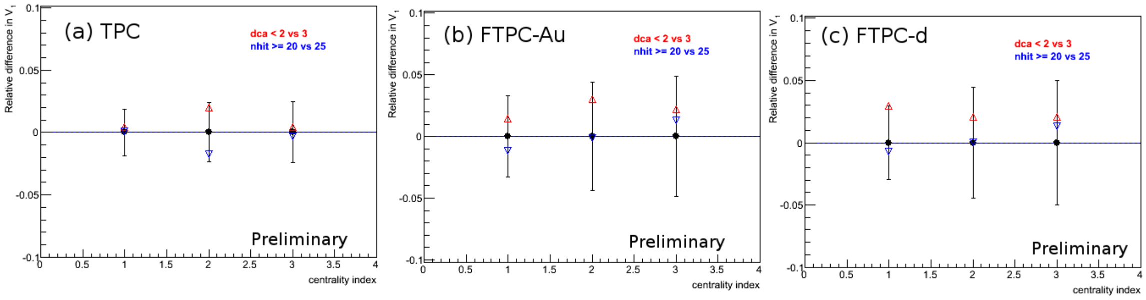

Figure 5.22. Systematic error estimation (relative error $\frac{V_1 - V_1^{default}}{V_1^{default}}$) for Fourier coefficient V_1 by changing track cuts for TPC-TPC ($1.2 < |\Delta\eta| < 1.8$), TPC-FTPC Au-side ($-4.5 < \Delta\eta < -2$), and TPC-FTPC d-side ($2 < \Delta\eta < 4.5$) correlations with FTPC Au-side multiplicity event selection.

5.8.2 Results

The left panel of Figure 5.25 shows the Fourier coefficient V_1, the middle panel shows the V_2 and the right panel shows the V_3. V_3 is mostly consistent with zero. Three $\Delta\eta$ ranges for the correlations are shown: the TPC-FTPC Au-side, the TPC-TPC, and the TPC-FTPC d-side correlations. Results from all three centrality defi-

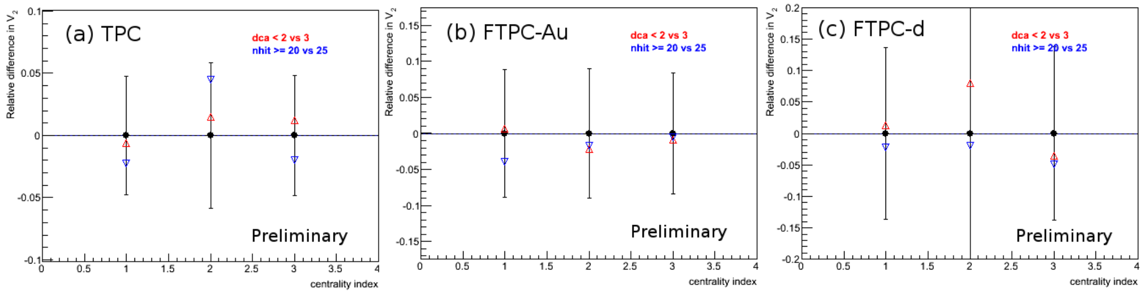

Figure 5.23. Systematic error estimation (relative error $\frac{V_2 - V_2^{default}}{V_2^{default}}$) for Fourier coefficient V_2 by changing track cuts for TPC-TPC ($1.2 < |\Delta\eta| < 1.8$), TPC-FTPC Au-side ($-4.5 < \Delta\eta < -2$), and TPC-FTPC d-side ($2 < \Delta\eta < 4.5$) correlations with FTPC Au-side multiplicity event selection.

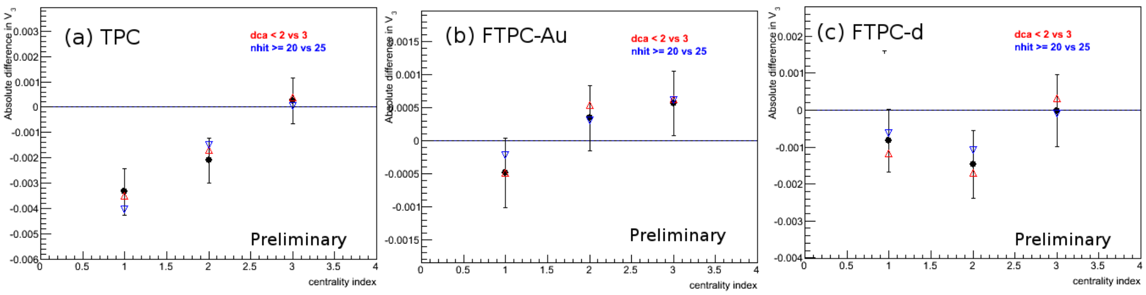

Figure 5.24. Systematic error estimation (absolute error $V_3 - V_3^{default}$) for Fourier coefficient V_3 by changing track cuts for TPC-TPC $1.2 < |\Delta\eta| < 1.8$, TPC-FTPC Au-side $-4.5 < \Delta\eta < -2$, and TPC-FTPC d-side $2 < \Delta\eta < 4.5$ with FTPC Au-side multiplicity event selection.

nitions are shown, plotted at the corresponding measured mid-rapidity charged particle $dN/d\eta$. V_2 is finite at all measured $\Delta\eta$, and is larger at mid-rapidity than at forward/backward rapidities; V_2 from the TPC-FTPC d-side correlation may be even larger than that from the TPC-FTPC Au-side correlation. As shown in the left panel of Fig. 5.25, V_1 varies approximately as $(dN/d\eta)^{-1}$, and from the middle panel of Fig. 5.25, V_2 is approximately independent of $dN/d\eta$. As a result, the "central−peripheral" correlated yield (essentially products of multiplicity and V_n) could be dominated by a V_2 component, with a magnitude similar to those for the individual peripheral and central data. There appears to be a symmetric back-to-back double ridge at large $\Delta\eta$ in "central−peripheral" correlations. After accounting for multiplicity biases, the "central−scaled-peripheral" correlated yield is essentially eliminated on the away side, as shown by the open symbols in Fig. 5.18.

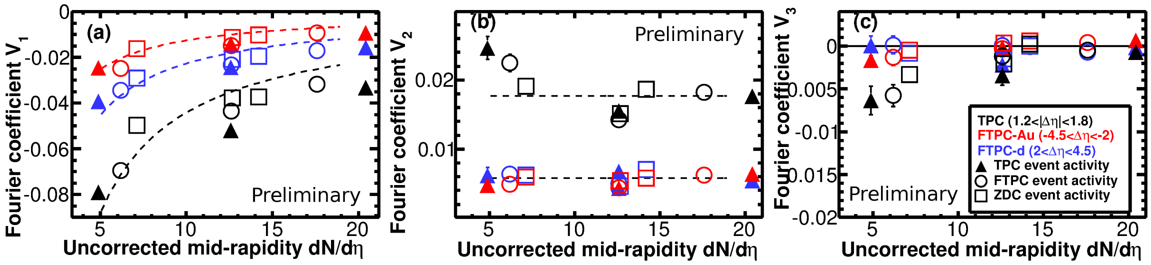

Figure 5.25. Fourier coefficients V_1 (left panel), V_2 (middle panel) and V_3 (right panel) versus the measured mid-rapidity charged particle density $dN/d\eta$.

Figure 5.26 shows the second harmonic Fourier coefficient V_n as a function of $\Delta\eta$ for both central and peripheral collisions. The near-side jet peak at $\Delta\eta = 0$ is clearly seen in all V_n. V_2 continues to decrease with increasing $|\Delta\eta|$ from the small $|\Delta\eta|$ jet region to the large $|\Delta\eta|$ ridge region. The V_2 values are similar between central and peripheral d+Au collisions. A V_2 from the jet correlation decreases as $|\Delta\eta|$ increases. However, if V_2 at large $\Delta\eta$ is of a hydrodynamic collective flow origin, the decreasing trend with $\Delta\eta$ is not unreasonable. However, the similar magnitudes in central and peripheral collisions seem surprising in the hydrodynamic collective flow picture.

5.9 Summary

Dihadron correlations are measured at mid-rapidity and forward/backward rapidities using the STAR TPC and FTPC as a function of centrality, i.e. event activity, in d+Au collisions at $\sqrt{s_{\rm NN}} = 200$ GeV. The centrality is classified by three measure-

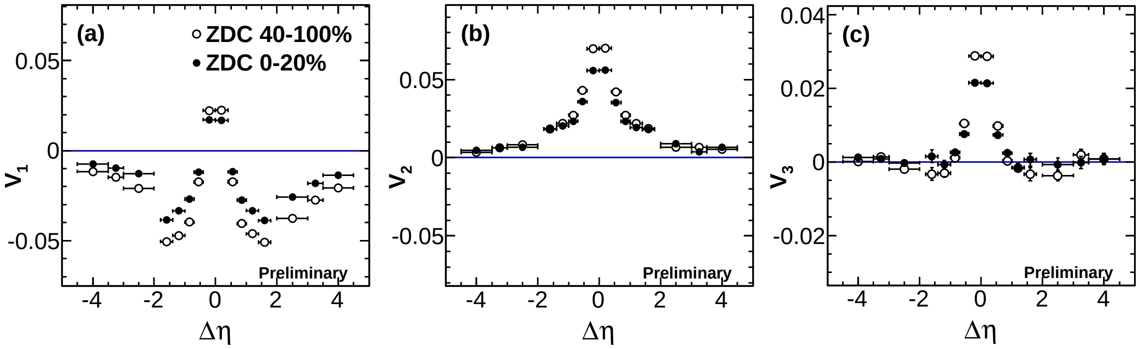

Figure 5.26. Fourier coefficient V_1 (left panel), V_2 (middle panel) and V_3 (right panel) versus $\Delta\eta$.

ments: the mid-rapidity TPC charged particle multiplicity, the FTPC-Au forward charged particle multiplicity, and the ZDC-Au zero-degree neutral energy.

The correlated yields are extracted by subtracting the estimated $\Delta\phi$-independent combinatorial background using the ZYAM method. It is found that the correlated yield is larger in central than peripheral collisions, and that the $\Delta\eta$-dependence of the observed yield difference resembles jetlike features, suggesting a jetlike origin. There could be multiple reasons for this difference, ranging from simple auto-correlation biases to physical differences between central and peripheral d+Au collisions. After scaling the peripheral data by the ratio of the near-side jetlike correlated yields, the away-side correlation difference is significantly diminished. This analysis demonstrates that the long-range dihadron correlation difference between central and peripheral events at RHIC may primarily be due to jets. Such event-selection effects on jetlike correlations must be addressed before investigating possible non-jet correlations, such as anisotropic flow, in d+Au collisions at RHIC.

Finite near-side correlated yields are present above the estimated ZYAM background in central d+Au collisions at large $\Delta\eta$ between particle pairs both from the TPC as well as from the TPC and the Au-beam direction FTPC. The near-side ridge at $|\Delta\eta| > 1$ appears to scale with the away-side correlated yield, which is believed that the away-side yield is dominated by jet contributions in d+Au collisions at $\sqrt{s_{\mathrm{NN}}} = 200$ GeV. The near-side ridge does not scale with the estimated ZYAM background.

Fourier coefficients of the raw dihadron correlations are also reported. All $\Delta\phi$ correlation functions appear to have a V_1 and a V_2 Fourier component. The V_1 is found to be approximately inversely proportional to event multiplicity. The V_2 is found to decrease with $\Delta\eta$, but remains finite at both forward and backward rapidities of $|\Delta\eta| \approx 3$ with similar magnitudes. The V_2 is found approximately independent of the event multiplicity. Extreme caution should be taken when interpreting the V_2 result in peripheral collisions as being from jets and in central d+Au collisions as primarily being from non-jet, elliptic flow physics.

6. Conclusion

Three distinct but intellectually connected measurements are reported in this thesis. The first regards triangular harmonic flow in heavy-ion collisions, which is considered to be the primary source for the novel near-side ridge and away-side double-peak measurements in two-particle correlations. The second regards isolation of flow and nonflow effects in two-particle correlations, which is critical in extracting QGP properties, such as the shear viscosity to entropy density ratio η/s. The third regards long-range ridge correlations in d+Au collisions, which have important implications to possible QGP formation in small systems.

The ridge is a small azimuthal opening-angle correlation but long-range in pseudorapidity. The double-peak correlation refers to two peaks in the jet recoil direction in azimuth. Both were observed in heavy ion collisions after the subtraction of elliptic flow background, and can be quantified by triangular flow v_3. The $\Delta\eta$-gap, centrality and p_T dependence of v_3 is measured in Au+Au collisions at $\sqrt{s_{\mathrm{NN}}} = 200$ GeV. The hydrodynamic calculation with a lumpy initial condition describes well the measured v_3 below $p_T < 2$ GeV/c. The measurement helps constrain the η/s parameter in hydrodynamic model calculations.

The isolation of flow (a global correlation) and nonflow (few-body correlations) exploits the measurements of two- and four-particle azimuthal cumulants in symmetric Au+Au collisions. A data-driven method is applied to separate the $\Delta\eta$-dependent and $\Delta\eta$-independent azimuthal correlations. The $\Delta\eta$-independent correlation is dominated by flow and flow fluctuations. It is found to be constant over η in the measured range $|\eta| < 1$. The relative flow fluctuation is found be to $34\% \pm 2\%(stat.) \pm 3\%(sys.)$ in 20-30% central Au+Au collisions at $\sqrt{s_{NN}} = 200$ GeV. The $\Delta\eta$-dependent correlation may be attributed to nonflow. It is found to be $5\% \pm 2\%$ relative to the square of the average flow for those same collisions with $|\Delta\eta| > 0.7$ and $0.15 < p_T < 2$ GeV/c.

While Au+Au collisions have large collective flow, angular correlations in d+Au collisions are dominated by jet production at modest p_T. It is found that the jetlike correlations depend on the collision activity, in contrast to initial expectations. To account for the dependence, a scaling factor is applied to the low-activity data to be subtracted from the high-activity data. The remaining nonjet correlation is minimal on the away side. On the near side, a finite correlated yield is observed to extend to large pseudo-rapidity distances in high-activity collisions. This so-called near-side ridge appears to scale with the away-side jet as a function of $\Delta\eta$. A Fourier analysis of the measured azimuthal correlations indicates a V_2, independent of collision activity, with similar magnitudes between Au- and d-going directions. These measurements help constrain theoretical models for the ridge in d+Au collisions.

APPENDIX

A. Kinematic Variables

When dealing with relativistic heavy-ion collisions, several kinematic variables are used such that they have simple forms under the Lorentz transformation. The natural units are used, $c = \hbar = 1$, where c is the speed of light and $\hbar$ is the Planck constant.

The contravariant vector of a particle with momentum $\vec{p}$ and energy E is

$$p^{\mu} = (E, \vec{p}) = (E, \vec{p_T}, p_z) = (E, p_x, p_y, p_z), \tag{A.1}$$

where z is the beam direction and x-y is the transverse plane. The transverse momentum magnitude is $p_T = |\vec{p_T}| = \sqrt{p_x^2 + p_y^2}$, and the azimuthal angle ϕ spans from the x-axis to the $\vec{p_T}$ vector.

The rapidity of a particle is defined as

$$y = \frac{1}{2}\ln\frac{E + p_z}{E - p_z}. \tag{A.2}$$

Rapidity is a dimensionless variable. The advantage of using rapidity is that its Lorentz transformation has an additive form. For example, a particle has rapidity y in one frame, and rapidity y' in another frame moving at a velocity β in the z-direction relative to the first. The Lorentz transformation of the particle rapidity is simply given by

$$y' = y - y_{\beta} \tag{A.3}$$

where

$$y_{\beta} = \frac{1}{2}\ln\frac{1 + \beta}{1 - \beta}. \tag{A.4}$$

Following relations relate rapidity y and other kinematic variables:

$$E = m_T \cosh y, \tag{A.5}$$

$$p_z = m_T \sinh y. \tag{A.6}$$

where transverse mass $m_T = \sqrt{m^2 + p_T^2}$.

Despite the convenience of rapidity, the particle mass (particle species) is not easy to measure in experiments. The pseudo-rapidity η is often used as a substitute for y. The η is given by the particle momentum polar angle θ relative to the beam axis:

$$\eta = -\ln \tan \frac{\theta}{2} = \frac{1}{2} \ln \frac{|\vec{p}| + p_z}{|\vec{p}| - p_z}. \tag{A.7}$$

For massless particles, $\eta = y$. For mid-rapidity particles, $\beta_z \ll 1$: $\eta \approx y$. Similarly the following relations are useful:

$$|\vec{p}| = p_T \cosh \eta, \tag{A.8}$$

$$p_z = p_T \sinh \eta. \tag{A.9}$$

LIST OF REFERENCES

LIST OF REFERENCES

[1] M. Gell-Mann. A schematic model of baryons and mesons. *Physics Letters*, 8(3):214 – 215, 1964.

[2] G. Zweig. An SU(3) model for strong interaction symmetry and its breaking. Version 1. 1964.

[3] G. Zweig. An SU(3) model for strong interaction symmetry and its breaking. Version 2. pages 22–101, 1964.

[4] Y. Nambu. *A systematics of hadrons in subnuclear physics*, pages 133–142. 1966.

[5] M. Y. Han and Y. Nambu. Three-Triplet Model with Double SU(3) Symmetry. *Physical Review*, 139:B1006–B1010, 1965.

[6] H. D Politzer. Reliable Perturbative Results for Strong Interactions? *Physical Review Letters*, 30:1346–1349, 1973.

[7] D. J. Gross and F. Wilczek. Ultraviolet Behavior of Non-Abelian Gauge Theories. *Physical Review Letters*, 30:1343–1346, 1973.

[8] E. V. Shuryak. Quark-Gluon Plasma and Hadronic Production of Leptons, Photons and Psions. *Physics Letters B*, 78:150, 1978.

[9] H. Bohr and H.B. Nielsen. Hadron production from a boiling quark soup: A thermodynamical quark model predicting particle ratios in hadronic collisions . *Nuclear Physics B*, 128(2):275 – 293, 1977.

[10] M. Plmer, S. Raha, and R. M. Weiner. How free is the quark-gluon-plasma? . *Nuclear Physics A*, 418(0):549 – 557, 1984.

[11] W. A. Zajc. The Fluid Nature of Quark-Gluon Plasma . *Nuclear Physics A*, 805(14):283c – 294c, 2008. INPC 2007 Proceedings of the 23rd International Nuclear Physics Conference.

[12] J. F. Gunion and R. S. Willey. Hadronic spectroscopy for a linear quark containment potential. *Physical Review D*, 12:174–186, 1975.

[13] A. Chodos, R. L. Jaffe, K. Johnson, C. B. Thorn, and V. F. Weisskopf. New extended model of hadrons. *Physical Review D*, 9:3471–3495, 1974.

[14] H. Satz. *Extreme States of Matter in Strong Interaction Physics*, volume 841 of *Lecture Notes in Physics*, chapter The Analysis of Dense Matter. Springer, 2012.

[15] J.D. Bjorken. Highly relativistic nucleus-nucleus collisions: The central rapidity region. *Physical Review D*, 27:140, 1983.

[16] J. Kuti, J. Polnyi, and K. Szlachnyi. Monte Carlo study of SU(2) gauge theory at finite temperature . *Physics Letters B*, 98(3):199 – 204, 1981.

[17] Larry D. M. and Benjamin S. A Monte Carlo study of SU(2) Yang-Mills theory at finite temperature . *Physics Letters B*, 98(3):195 – 198, 1981.

[18] E. Iancu. QCD in heavy ion collisions. arXiv:1205.0579, 2012.

[19] M. Kliemant et al. *The Physics of the Quark-Gluon Plasma*, chapter Global Properties of Nucleus-Nucleus Collisions. Springer, 2010.

[20] B. Muller and J. L. Nagle. Results from the relativistic heavy ion collider. *Annual Review of Nuclear and Particle Science*, 56:93–135, 2006.

[21] J. Sollfrank, P. Huovinen, M. Kataja, P. V. Ruuskanen, M. Prakash, and R. Venugopalan. Hydrodynamical description of 200A GeV/c S+Au collisions: Hadron and electromagnetic spectra. *Physical Review C*, 55:392–410, 1997.

[22] B.R. Schlei, U. Ornik, M. Plumer, D. Strottman, and R.M. Weiner. Hydrodynamical analysis of single inclusive spectra and Bose-Einstein correlations for Pb + Pb at 160 A GeV. *Physics Letters*, B376:212–219, 1996.

[23] C.M. Hung and Edward V. Shuryak. Equation of state, radial flow and freezeout in high-energy heavy ion collisions. *Physical Review C*, 57:1891–1906, 1998.

[24] J. Adams et al. Identified particle distributions in pp and Au+Au collisions at $\sqrt{s_{\rm NN}} = 200$ GeV. *Physical Review Letters*, 92:112301, 2004.

[25] H. A. Gustafsson, H. H. Gutbrod, B. Kolb, H. Löhner, B. Ludewigt, A. M. Poskanzer, T. Renner, H. Riedesel, H. G. Ritter, A. Warwick, F. Weik, and H. Wieman. Collective Flow Observed in Relativistic Nuclear Collisions. *Physical Review Letters*, 52:1590–1593, 1984.

[26] J. Adams et al. Azimuthal anisotropy at RHIC: The First and fourth harmonics. *Physical Review Letters*, 92:062301, 2004.

[27] J. Adams et al. Directed flow in Au+Au collisions at $\sqrt{s_{\rm NN}} = 62$ GeV. *Physical Review C*, 73:034903, 2006.

[28] B.I. Abelev et al. System-size independence of directed flow at the Relativistic Heavy-Ion Collider. *Physical Review Letters*, 101:252301, 2008.

[29] L. Adamczyk et al. Directed Flow of Identified Particles in Au + Au Collisions at $\sqrt{s_{\rm NN}} = 200$ GeV at RHIC. *Physical Review Letters*, 108:202301, 2012.

[30] L. Adamczyk et al. Beam-Energy Dependence of Directed Flow of Protons, Antiprotons and Pions in Au+Au Collisions. *Physical Review Letters*, 112:162301, 2014.

[31] B. Abelev et al. Directed Flow of Charged Particles at Midrapidity Relative to the Spectator Plane in Pb-Pb Collisions at $\sqrt{s_{\rm NN}}$=2.76 TeV. *Physical Review Letters*, 111(23):232302, 2013.

[32] R. S. Bhalerao and J.-Y. Ollitrault. Eccentricity fluctuations and elliptic flow at RHIC. *Physics Letters B*, 641(34):260 – 264, 2006.

[33] D. Teaney and L. Yan. Nonlinearities in the harmonic spectrum of heavy ion collisions with ideal and viscous hydrodynamics. *Physical Review C*, 86:044908, 2012.

[34] H. Niemi, G. Denicol, H. Holopainen, and P. Huovinen. Event-by-event distributions of azimuthal asymmetries in ultrarelativistic heavy-ion collisions. *Physical Review C*, 87:054901, 2013.

[35] F Gardim, F. Grassi, M. Luzum, and J.-Y. Ollitrault. Mapping the hydrodynamic response to the initial geometry in heavy-ion collisions. *Physical Review C*, 85:024908, 2012.

[36] B. Alver and G. Roland. Collision-geometry fluctuations and triangular flow in heavy-ion collisions. *Physical Review C.*, 81:054905, 2010.

[37] B. Alver et al. System size, energy, pseudorapidity, and centrality dependence of elliptic flow. *Physical Review Letters*, 98:242302, 2007.

[38] A. Bilandzic, R. Snellings, and S. Voloshin. Flow analysis with cumulants: Direct calculations. *Physical Review C*, 83:044913, 2011.

[39] D. d'Enterria and B. Betz. *The Physics of the Quark-Gluon Plasma*, chapter High-p_T Hadron Suppression and Jet Quenching. Springer, 2010.

[40] A. H. Mueller. *Advanced Series on Directions in High Energy Physics*, volume 5. World Scientific, 1989.

[41] J.W. Cronin et al. Production of hadrons at large transverse momentum at 200, 300, and 400 GeV. *Physical Review D*, 11:3105, 1975.

[42] K. Adcox et al. Suppression of Hadrons with Large Transverse Momentum in Central $Au + Au$ Collisions at $\sqrt{s_{\mathrm{NN}}} = 130\mathrm{GeV}$. *Physical Review Letters*, 88:022301, 2002.

[43] C. Adler et al. Centrality Dependence of High-p_T Hadron Suppression in $\mathrm{Au} + \mathrm{Au}$ Collisions at $\sqrt{s_{\mathrm{NN}}} = 130\ \ \mathrm{GeV}$. *Physical Review Letters*, 89:202301, 2002.

[44] U. A. Wiedemann. *Relativistic Heavy Ion Physics*, volume 23 of *Landolt-Börnstein: Numerical Data and Functional Relationships in Science and Technology - New Series*, chapter Jet Quenching in Heavy Ion Collisions. Springer, 2009.

[45] S. Chatrchyan et al. Observation and studies of jet quenching in PbPb collisions at nucleon-nucleon center-of-mass energy $\sqrt{s_{\mathrm{NN}}}$= 2.76 TeV. *Physical Review C*, 84:024906, 2011.

[46] N. N. Ajitanand, J. M. Alexander, P. Chung, W. G. Holzmann, M. Issah, Roy A. Lacey, A. Shevel, A. Taranenko, and P. Danielewicz. Decomposition of harmonic and jet contributions to particle-pair correlations at ultrarelativistic energies. *Physical Review C*, 72:011902, 2005.

[47] C. Adler et al. Disappearance of back-to-back high p_T hadron correlations in central Au+Au collisions at $\sqrt{s_{\mathrm{NN}}} = 200$ GeV. *Physical Review Letters*, 90:082302, 2003.

[48] J. Adams et al. Direct observation of dijets in central Au+Au collisions at $\sqrt{s_{\mathrm{NN}}} = 200$ GeV. *Physical Review Letters*, 97:162301, 2006.

[49] J. Adams et al. Distributions of Charged Hadrons Associated with High Transverse Momentum Particles in *pp* and Au + Au Collisions at $\sqrt{s_{\mathrm{NN}}} = 200$ GeV. *Physical Review Letters*, 95:152301, 2005.

[50] B. I. Abelev et al. Long range rapidity correlations and jet production in high energy nuclear collisions. *Physical Review C*, 80:064912, 2009.

[51] B. Alver et al. High Transverse Momentum Triggered Correlations over a Large Pseudorapidity Acceptance in Au+Au Collisions at $\sqrt{s_{\mathrm{NN}}} = 200$ GeV. *Physical Review Letters*, 104:062301, 2010.

[52] J. Adams et al. $\Delta\phi - \Delta\eta$ correlations in central Au+Au collisions at $\sqrt{s_{\mathrm{NN}}} = 200$ GeV. *Physical Review C*, 75:034901, 2007.

[53] B. I. Abelev et al. Long range rapidity correlations and jet production in high energy nuclear collisions. *Physical Review C*, 80:064912, 2009.

[54] A. Dumitru, F. Gelis, L. McLerran, and R. Venugopalan. Glasma flux tubes and the near side ridge phenomenon at RHIC . *Nuclear Physics A*, 810(14):91 – 108, 2008.

[55] S. Gavin, L. McLerran, and G. Moschelli. Long range correlations and the soft ridge in relativistic nuclear collisions. *Physical Review C*, 79:051902, 2009.

[56] L. McLerran and R. Venugopalan. Computing quark and gluon distribution functions for very large nuclei. *Physical Review D*, 49:2233–2241, 1994.

[57] T. Lappi and L. McLerran. Some features of the glasma. *Nuclear Physics A*, 772(34):200 – 212, 2006.

[58] A. Adare et al. Dihadron azimuthal correlations in Au+Au collisions at $\sqrt{s_{\mathrm{NN}}} = 200$ GeV. *Physical Review C*, 78:014901, 2008.

[59] E. C. Aschenauer et al. The RHIC Spin Program: Achievements and Future Opportunities. 2013.

[60] W. Haeberli. Sources of Polarized Ions. *Annual Review of Nuclear and Particle Science*, 17:373–426, 1967.

[61] M. A. Stephanov. Sign of Kurtosis near the QCD Critical Point. *Physical Review Letters*, 107:052301, 2011.

[62] L. Adamczyk et al. Elliptic flow of identified hadrons in Au+Au collisions at $\sqrt{s_{\mathrm{NN}}} = 7.7$-$62.4$ GeV. *Physical Review C*, 88:014902, 2013.

[63] L. Adamczyk et al. Beam Energy Dependence of Moments of the Net-Charge Multiplicity Distributions in Au + Au Collisions at RHIC. *Physical Review Letters*, 113:092301, 2014.

[64] L. Adamczyk et al. Energy Dependence of Moments of Net-Proton Multiplicity Distributions at RHIC. *Physical Review Letters*, 112:032302, 2014.

[65] A. Deshpande et al. Study of the Fundamental Structure of Matter with an Electron Ion Collider. *Annual Review of Nuclear and Particle Science*, 55:165–228, 2005.

[66] E. C. Aschenauer and other. eRHIC Design Study: An Electron-Ion Collider at BNL. arXiv:1409.1633, 2014.

[67] K.H. Ackermann et al. STAR detector overview. *Nuclear Instruments and Methods*, A499(23):624 – 632, 2003.

[68] J Anderson, A. Berkovitz, W. Betts, et al. The STAR time projection chamber: a unique tool for studying high multiplicity events at RHIC. *Nuclear Instruments and Methods*, A499:659–678, 2003.

[69] K.H. Ackermann, F. Bieser, F.P. Brady, et al. The forward time projection chamber in STAR . *Nuclear Instruments and Methods*, A499(23):713 – 719, 2003.

[70] C. Adler, A. Denisov, E. Garcia, M. Murray, H. Stroebele, and S. White. The RHIC zero degree calorimeters . *Nuclear Instruments and Methods*, A470(3):488 – 499, 2001.

[71] M. L. Miller, K. Reygers, S. J. Sanders, and P. Steinberg. Glauber Modeling in High-Energy Nuclear Collisions. *Annual Review of Nuclear and Particle Science*, 57:205–243, 2007.

[72] L. Adamczky et al. Third harmonic flow of charged particles in Au+Au collisions at $\sqrt{s_{\mathrm{NN}}} = 200$ GeV. *Physical Review C*, 88:014904, 2013.

[73] N. Borghini, P. M. Dinh, and J. Y. Ollitrault. Is the analysis of flow at the CERN Super Proton Synchrotron reliable? *Physical Review C*, 62:034902, 2000.

[74] N. Borghini, P. M. Dinh, and J. Y. Ollitrault. New method for measuring azimuthal distributions in nucleus-nucleus collisions. *Physical Review C*, 63:054906, 2001.

[75] N. Borghini, P. M. Dinh, and J. Y. Ollitrault. Flow analysis from multiparticle azimuthal correlations. *Physical Review C*, 64:054901, 2001.

[76] H. Agakishiev et al. Event-plane-dependent dihadron correlations with harmonic v_n subtraction in Au + Au collisions at $\sqrt{s_{\mathrm{NN}}} = 200$ GeV. *Physical Review C*, 89:041901, 2014.

[77] M. Procura and W. J. Waalewijn. Fragmentation in jets: Cone and threshold effects. *Physical Review D*, 85:114041, 2012.

[78] G. Agakishiev et al. Energy and system-size dependence of two- and four-particle v_2 measurements in heavy-ion collisions at $\sqrt{s_{\mathrm{NN}}} = 62.4$ and 200 GeV and their implications on flow fluctuations and nonflow. *Physical Review C*, 86:014904, 2012.

[79] G. Aad et al. Measurement of event-plane correlations in $\sqrt{s_{\mathrm{NN}}} = 2.76$ TeV lead-lead collisions with the ATLAS detector. *Physical Review C*, 90:024905, 2014.

[80] B. Schenke, S. Jeon, and C. Cale. Elliptic and Triangular Flow in Event-by-Event D $= 3 + 1$ Viscous Hydrodynamics. *Physical Review Letters*, 106:042301, 2011.

[81] N.M. Abdelwahab et al. Isolation of Flow and Nonflow Correlations by Two- and Four-Particle Cumulant Measurements of Azimuthal Harmonics in $\sqrt{s_{\rm NN}} =$ 200 GeV Au+Au Collisions. arXiv:1409.2043,2014.

[82] P. K. Kovtun, D. T. Son, and A. O. Starinets. Viscosity in Strongly Interacting Quantum Field Theories from Black Hole Physics. *Physical Review Letters*, 94:111601, 2005.

[83] S. Wang, Y. Z. Jiang, Y. M. Liu, D. Keane, D. Beavis, S. Y. Chu, S. Y. Fung, M. Vient, C. Hartnack, and H. Stöcker. Measurement of collective flow in heavy-ion collisions using particle-pair correlations. *Physical Review C*, 44:1091–1095, 1991.

[84] H. Song, S. A. Bass, U. Heinz, T. Hirano, and C. Shen. 200 A GeV Au+Au collisions serve a nearly perfect quark-gluon liquid. *Physical Review Letters*, 106:192301, 2011.

[85] A. M. Poskanzer and S. A. Voloshin. Methods for analyzing anisotropic flow in relativistic nuclear collisions. *Physical Review C*, 58:1671–1678, 1998.

[86] L. Xu, L. Yi, D. Kikola, J. Konzer, F. Wang, and W. Xie. Model-independent decomposition of flow and nonflow in relativistic heavy-ion collisions. *Physical Review C*, 86:024910, 2012.

[87] P. Bozek, W. Broniowski, and J. Moreira. Torqued fireballs in relativistic heavy-ion collisions. *Physical Review C*, 83:034911, 2011.

[88] H. Petersen, V. Bhattacharya, S. A. Bass, and C. Greiner. Longitudinal correlation of the triangular flow event plane in a hybrid approach with hadron and parton cascade initial conditions. *Physical Review C*, 84:054908, 2011.

[89] K. Xiao, F. Liu, and F. Wang. Event-plane decorrelation over pseudorapidity and its effect on azimuthal anisotropy measurements in relativistic heavy-ion collisions. *Physical Review C*, 87:011901, 2013.

[90] J. Y. Ollitrault, A. M. Poskanzer, and S. A. Voloshin. Effect of flow fluctuations and nonflow on elliptic flow methods. *Physical Review C*, 80:014904, 2009.

[91] B. I. Abelev et al. Centrality dependence of charged hadron and strange hadron elliptic flow from $\sqrt{s_{\rm NN}} = 200$ GeV Au + Au collisions. *Physical Review C*, 77:054901, 2008.

[92] J. Adams et al. Azimuthal anisotropy in Au+Au collisions at $\sqrt{s_{\rm NN}} = 200$ GeV. *Physical Review C*, 72:014904, 2005.

[93] K.H. Ackermann et al. The STAR time projection chamber. *Nuclear Physics A*, 661:681–685, 1999.

[94] B. I. Abelev et al. Systematic measurements of identified particle spectra in pp, $d+$ Au, and Au $+$ Au collisions at the STAR detector. *Physical Review C*, 79:034909, 2009.

[95] B. Alver et al. Non-flow correlations and elliptic flow fluctuations in gold-gold collisions at $\sqrt{s_{\mathrm{NN}}} = 200$ GeV. *Physical Review C*, 81:034915, 2010.

[96] I. Arsene et al. Quarkgluon plasma and color glass condensate at RHIC? The perspective from the BRAHMS experiment . *Nuclear Physics A*, 757(12):1 – 27, 2005.

[97] B.B. Back et al. The PHOBOS perspective on discoveries at RHIC . *Nuclear Physics A*, 757(12):28 – 101, 2005.

[98] J. Adams et al. Experimental and theoretical challenges in the search for the quarkgluon plasma: The STAR Collaboration's critical assessment of the evidence from RHIC collisions . *Nuclear Physics A*, 757(12):102 – 183, 2005. First Three Years of Operation of RHIC.

[99] K. Adcox et al. Formation of dense partonic matter in relativistic nucleusnucleus collisions at RHIC: Experimental evaluation by the PHENIX Collaboration . *Nuclear Physics A*, 757(12):184 – 283, 2005. First Three Years of Operation of RHIC.

[100] S. Chatrchyan et al. Observation of long-range, near-side angular correlations in pPb collisions at the LHC. *Physics Letters B*, 718(3):795 – 814, 2013.

[101] B. Abelev et al. Long-range angular correlations on the near and away side in pPb collisions at $\sqrt{s_{\mathrm{NN}}} = 5.02$ TeV. *Physics Letters B*, 719(13):29 – 41, 2013.

[102] G. Aad et al. Observation of Associated Near-Side and Away-Side Long-Range Correlations in $\sqrt{s_{\mathrm{NN}}}$=5.02 TeV Proton-Lead Collisions with the ATLAS Detector. *Physical Review Letters*, 110:182302, 2013.

[103] G. Aad et al. Measurement of long-range pseudorapidity correlations and azimuthal harmonics in $\sqrt{s_{\mathrm{NN}}} = 5.02$ TeV proton-lead collisions with the ATLAS detector. *Physical Review C*, 90:044906, 2014.

[104] A. Adare et al. Quadrupole Anisotropy in Dihadron Azimuthal Correlations in Central d+Au Collisions at $\sqrt{s_{\mathrm{NN}}}$=200 GeV. *Physical Review Letters*, 111:212301, 2013.

[105] B. B. Abelev et al. Multi-particle azimuthal correlations in p-Pb and Pb-Pb collisions at the LHC. arXiv:1406.2474,2014.

[106] Q. Wang. Azimuthal anisotropy of charged particles from multiparticle correlations in pPb and PbPb collisions with CMS. *Nuclear Physics A*, 931(0):997 – 1001, 2014.

[107] B. B. Abelev et al. Long-range angular correlations of π, K and p in p-Pb collisions at $\sqrt{s_{\mathrm{NN}}} = 5.02$ TeV. *Physics Letters B*, 726:164–177, 2013.

[108] A. Adare et al. Measurement of long-range angular correlation and quadrupole anisotropy of pions and (anti)protons in central d+Au collisions at $\sqrt{s_{\mathrm{NN}}}$=200 GeV. arXiv:1404.7461, 2014.

[109] A. Dumitru, K. Dusling, F. Gelis, J. Jalilian-Marian, T. Lappi, and R. Venugopalan. The ridge in protonproton collisions at the LHC. *Physics Letters B*, 697(1):21 – 25, 2011.

[110] A. Dumitru, J. Jalilian-Marian, and E. Petreska. Two-gluon correlations and initial conditions for small x evolution. *Physical Review D*, 84:014018, 2011.

[111] P. Tribedy and R. Venugopalan. QCD saturation at the LHC: Comparisons of models to p+p and A+A data and predictions for p+Pb collisions . *Physics Letters B*, 710(1):125 – 133, 2012.

[112] P. Tribedy and R. Venugopalan. Erratum to QCD saturation at the LHC: Comparisons of models to and data and predictions for collisions [Physics Letters B 710 (1) (2012) 125] . *Physics Letters B*, 718(3):1154 –, 2013.

[113] M. Gyulassy, P. Levai, I. Vitev, and T.S. Bir. Initial-state bremsstrahlung versus final-state hydrodynamic sources of azimuthal harmonics in at RHIC and LHC . *Nuclear Physics A*, 931(0):943 – 948, 2014.

[114] D. Molnar, F. Wang, and C. H. Greene. Momentum anisotropy in nuclear collisions from quantum mechanics. arXiv:1404.4119,2014.

[115] J. Adams et al. Evidence from d+Au Measurements for Final-State Suppression of High-p_T Hadrons in Au + Au Collisions at RHIC. *Physical Review Letters*, 91:072304, 2003.

[116] B. B. Abelev et al. Multiplicity dependence of jet-like two-particle correlations in p-Pb collisions at $\sqrt{s_{\mathrm{NN}}} = 5.02$ TeV. arXiv:1406.5463, 2014.

[117] M. Gyulassy and X. N. Wang. HIJING 1.0: A monte carlo program for parton and particle production in high energy hadronic and nuclear collisions. *Computer Physics Communications*, 83(23):307 – 331, 1994.

VITA

VITA

Li Yi graduated from University of Science and Technology of China in July 2010 with a Bachelor of Science Degree in Physics. She pursued her graduate study in Purdue University from 2010 to 2014. Li joined STAR experiment in the Relativistic Heavy-Ion Collider, Brookhaven National Lab, Upton, NY at year 2010. Li worked on the collective flow and jet correlation measurements by studying the particle correlations in d+Au and Au+Au collisions.